Analysis of short-period waves in the solar chromosphere

Dissertation
zur Erlangung des Doktorgrades
der Mathematisch-Naturwissenschaftlichen Fakultäten
der Georg-August-Universität zu Göttingen

vorgelegt von
Aleksandra Anđić
aus Banjaluka, Bosnia

Göttingen 2005

D7
Referent: Franz Kneer
Korreferent: Wolfgang Glatzel
Tag der mündlichen Prüfung:

Contents

Summary **5**

1 Introduction **7**
1.1 Heating of the solar atmosphere 8
1.2 Acoustic waves 10
1.2.1 Propagation 12
1.3 Magnetic field effects 13
1.4 Short-period waves 14

2 Observations **15**
2.1 Aim of the observations 15
2.1.1 Choice of the spectral line 15
2.2 Instrumentation 17
2.2.1 Telescope 17
2.2.2 Post-focus setting 18
2.3 Data 20
2.3.1 Observations 22

3 Data reduction and analysis methods **23**
3.1 Data reduction 23
3.1.1 Speckle reconstruction 24
3.1.2 Reconstruction of the narrowband images 26
3.2 Determination of the heights 27
3.2.1 Bisectors 27
3.2.2 Response functions 27
3.2.3 Velocity maps 32
3.3 The data cubes 33
3.3.1 Correlation 33
3.3.2 Destretching 34
3.4 Wavelet analysis 35
3.4.1 The mother wavelet 35
3.4.2 The code 36
3.4.3 Additional data processing 37

4 Results **39**
4.1 Waves at different heights . . . 39
4.1.1 Spatial location . . . 41
4.2 Methods used for the analysis of the data . . . 42
4.2.1 Comparison of the spatial distribution of short-period waves with white-light structures . . . 43
4.2.2 Determining the time shift . . . 46
4.2.3 Different periods . . . 48
4.2.4 Terms used for description of granular events . . . 49
4.3 Location of short-period waves . . . 50
4.3.1 The quiet Sun . . . 50
4.3.2 Solar area with G-band structures . . . 53
4.3.3 Observations containing a pore . . . 54
4.4 Relation of short-period waves to certain structures on the Sun . . . 56
4.4.1 The quiet Sun . . . 56
4.4.2 Solar area with G-band structures . . . 57
4.4.3 Observations containing a pore . . . 58
4.5 Relation between waves of different periods . . . 59
4.5.1 Variation of power location with periods . . . 60
4.5.2 Comparison of short-period waves with waves of the longer-period 63
4.6 Travelling of waves through the solar atmosphere . . . 66
4.6.1 Matching of similar power features . . . 67
4.7 Energy transport and the dissipation of energy . . . 74

5 Summary and conclusions **79**
5.1 Location of power . . . 79
5.2 Periods . . . 80
5.3 Travelling . . . 81
5.4 Energy . . . 81

6 Suggestions for future investigations **83**
6.1 Instrumental . . . 83
6.2 Information from the granular pattern . . . 83
6.3 Information from the line profiles . . . 83

A Appendix 1 **87**
A.1 Fabry- Perot interferometer . . . 87

B Appendix 2 **89**
B.1 2003 . . . 89
B.2 2004 . . . 89
B.2.1 22.6.2004 . . . 89
B.2.2 26.6.2004 . . . 90

Acknowledgements **95**

Curriculum Vitae **97**

Summary

The temperature of the solar atmosphere decreases to low values of 4200K at approximately 500km height above $\tau_{cont} = 1$ and then increases to approximately 10000K around 2300km height. This phenomenon can only be explained by mechanical heating of the chromosphere. Short-period acoustic waves were suggested as the source of the mechanical heating; waves with periods between 10s and 150s are assumed to be the main carriers of the required energy. Those waves originate in the sub-photosphere. Propagating through the solar atmosphere, they form shocks and thus dissipate energy.

Observations for this work were done with the telescope Vacuum tower Telescope (VTT) at the Observatorio del Teide, Tenerife. The data reduction is done with speckle interferometry. The velocity response functions are calculated using the LTE atmospheric model (Holweger & Müller 1974) for an estimate of the heights. The results are obtained with wavelet analysis.

Short-period waves exist at different heights and are located mostly above down flows. They closely follow the temporal evolution of the white-light structures. The short-period waves of different periods seem to be associated with different spatial scales.

The velocity interval of short-period wave propagation starts with $3.7 \pm 0.4 \frac{km}{s}$ but the upper limit can not be determined with the temporal resolution achieved in this work. The magnetic field has an influence on the propagation of short-period waves.

The energy flux at the height of 200km is:

$$F_{200} = 6.5 \pm 0.6 \, \frac{kW}{m^2}.$$

The energy flux at the height of 600km is:

$$F_{600} = 1.1 \pm 0.3 \, \frac{kW}{m^2}.$$

And the difference between those two energy fluxes is:

$$F_{200} - F_{600} = 5.4 \pm 0.5 \, \frac{kW}{m^2}.$$

This difference could represent the energy flux which is used for heating of chromosphere or the energy flux which simply returned to the photosphere. The interpretation depends on the adopted location of the chromospheric base.

1 Introduction

The Sun is an average star of spectral type G2. The mean distance between the Sun and the Earth is $A = 149597870 \pm 2$km (Stix 2002). This proximity makes it possible to study the Sun in great detail, as a representative star for a large quantity of main sequence stars. The atmosphere of the Sun marks those layers where most of the emitted photons can freely escape. The so called surface of the Sun is the layer where the continuum optical depth changes from $\tau_c \gg 1$ to $\tau_c \ll 1$. Due to the height variation of the physical parameters, the solar atmosphere is divided into several parts: the layer near the 'surface' forms the photosphere; the layer above is the chromosphere, followed by the corona which extends several solar radii around the Sun.

The photosphere is the visible part of the Sun; it is very thin and relatively dense, as compared to the solar atmosphere as a whole; it is the source of a large percentage of the solar radiation. Above it lays the chromosphere which is less dense and more transparent. It can be seen near the end and the beginning of total solar eclipses as a coloured flash, due to the intensive red colour of the $H\alpha$ spectral line. Higher still is the corona which extends from the top of the rather narrow transition layer to the heliopause.

The temperature structure of the chromosphere is interesting. As we leave the photosphere the temperature first falls to low values of 4200K at the height of approximately 500km, moving higher, the temperature increases to approximately 10000K (around a height of 2300km). This phenomenon can only be explained by mechanical heating of the chromosphere. During the last century, short-period acoustic waves were suggested as the source of the mechanical heating. Their origin was believed to be in the sub-photosphere. Propagating upwards through the solar atmosphere, they form shocks and dissipate energy in the chromosphere. Short-period waves with periods from 10s to 150s are assumed to be the main carrier of the required energy. The peak energy transport should occur for waves of periods below 50s. The chromosphere is considered to represent the onset of transport of mass, momentum and energy to upper layers of the atmosphere (Kneer 2002).

The observation of short-period waves encounters technical difficulties, since it requires good spatial and temporal resolution. These waves were thus first detected in the last few decades. Some of the observational works are: (von Uexküll et al. 1985) where detection of the waves with the period of 60s was done for the chromospheric layer, than (Wunnenberg et al. 2003), where the lowest detected period was 50s for the chromospheric layer and (Hansteen et al. 2000) with the lowest detected period of 100s for the transition layer.

1.1 Heating of the solar atmosphere

As mentioned above, we can observe in the chromosphere an increase of the temperature with the height above the temperature minimum. The chromosphere radiates more light than it absorbs from below. The radiative loss for the chromosphere is $(2.5-6)\cdot 10^3$ W/m^2, the uncertainty being caused by the differences of energy losses in quiet and active regions [1] (Kneer & Uexküll 1999). The heating required to balance the radiative loss is approximately $4\cdot 10^3\, W/m^2$ [2] (Kalkofen 2001). According to (Kalkofen 2001) the chromospheric temperature averaged over the time does not increase with height, and one can say that the problem of chromosphere heating is a question of energy supply for the radiative emission.

As source for the heating of the solar atmosphere one has to consider the convection zone. All late type stars with surface convection zones are believed to have hot chromospheric layers where the temperature increases outwards from low photospheric values to about $10^4 K$. It is believed that unresolved motions, or non-thermal micro-turbulence may be responsible for the energy transport to the chromosphere.

An amount of heat dQ entering into a volume element across its boundaries raises the entropy S by $dS = dQ/T$, where T is the temperature. For a gas element moving with sound velocity v through the chromosphere, we have an entropy conservation equation written in the Lagrange frame (Ulmschneider & Kalkofen 2003):

$$dS/dt = \partial S/\partial t + v\partial S/\partial z = dS/dt|_R + dS/dt|_J + dS/dt|_C + dS/dt|_V + dS/dt|_M, \quad (1.1)$$

here t is the time and z the height. The five terms are called radiative, Joule, thermal-conductive, viscous, and mechanical heating, respectively. The four terms on the right hand side are defined as (Ulmschneider & Kalkofen 2003):

$$dS/dt|_R = \frac{4\pi\overline{\kappa}}{\rho T}(J-B) \quad (1.2)$$

$$dS/dt|_J = \frac{j^2}{\lambda_{el}} \quad (1.3)$$

$$dS/dt|_C = \frac{d}{dz}\kappa_{th}\frac{dT}{dz} \quad (1.4)$$

$$dS/dt|_V = \eta_{vis}(\frac{dv}{dz})^2 \quad (1.5)$$

where $\overline{\kappa}$ is the Rosseland opacity [3], j is the current density, λ_{el} is the electrical conductivity, κ_{th} the thermal conductivity, T the temperature, J the frequency integrated mean intensity, B the frequency intergrated Planck function, η_{vis} the viscosity, v the velocity and ρ the density.

Calculations of heating rates done by Ulmschneider et al. (2003) show that Joule and thermal-conductive heating are too small to balance the chromospheric cooling rate in the

[1] or $(2.5-6)\cdot 10^6 \frac{erg}{cm^2 s}$

[2] or $4\cdot 10^6 \frac{erg}{cm^2 s}$

[3] mainly due to H^-

quiet regions, they can thus be ignored. Since the chromosphere does exist, there should be a mean steady state, and the left hand side of Eq. 1.1 should be zero. So we can write:

$$\frac{4\pi\overline{\kappa}}{\rho T}(J-B)+\frac{dS}{dt}|_M=0, \tag{1.6}$$

where $\frac{dS}{dt}|_R=\frac{4\pi\overline{\kappa}}{\rho T}(J-B)$ is the radiative heating. Hence, in stellar chromospheres, the main energy balance is between radiative and mechanical heating.

Since observations show that the temperature rises from the temperature minimum to the upper heights of the chromosphere, the term for mechanical heating has to be much larger than zero. Still higher the losses caused by the solar wind can not be balanced by thermal conduction alone. This leads to the conclusion that the existence of chromospheres, coronae and wind depends on a constant energy supply provided by mechanical heating (Ulmschneider & Kalkofen 2003).

The theory of weak shocks shows that in a uniform medium the crest of an acoustic wave has higher temperature, thus higher acoustic speed, thus propagates faster and will overtake the preceding, cooler wave valley, and a shock will form. In a stratified medium, the wave amplitude must increase with height (to keep the flux constant), and this allows us to estimate the distance for a shock formation:

$$\Delta Z=2Hln(1+\frac{\pi\gamma g}{\omega u_o(\gamma+1)}), \tag{1.7}$$

where u_o is the initial velocity amplitude, ω the frequency of the wave, γ the ratio of specific heats and $H=\frac{p_o}{\rho_o g}$ the scale height in the atmosphere. High frequency acoustic waves will form shocks within a few scale heights; low frequency waves need larger scales to shock. The variation of the dissipation and of the mechanical energy flux with height is shown in Fig. 1.1 for vertically propagating short (50s) and long (300s) period waves, both having a velocity amplitude of 0.3 km/s at $z=0$ (Stein & Leibacher 1974).

It seems reasonable to suppose that the upper chromosphere and corona are heated by five-minute oscillations which retain their sinusoidal profiles up to 1.2 Mm and shock above 1.5Mm height, while the low chromosphere is heated by turbulent convective motions via the 'Lighthill mechanism' (Stein & Leibacher 1974).

Kalkofen (2001) concludes that the energy flux generated in the convection zone by the Lighthill mechanism is large enough to cover the radiative losses of the chromosphere. Kalkofen (1990) also argues that different parts of the chromosphere are heated by waves of different wavelengths (see Sect. 1.2).

Radiation from the compressed region behind a shock front also removes energy from the wave. This radiative dissipation of the waves causes an excess of emission but does not increase the gas temperature. Heating by dissipation of acoustic shocks is time dependent. Short intervals of very high temperature are caused by acoustic shocks (Carlsson & Stein 1995). The maximum of the wave power is expected at a period of $P\approx 50s$. Of course, the spatial-temporal structure of the quiet chromosphere is still under debate, therefore the final conclusions are not yet made. Short-period waves do occur in the Sun's atmosphere but with strongly varying amplitude (Wunnenberg et al. 2003).

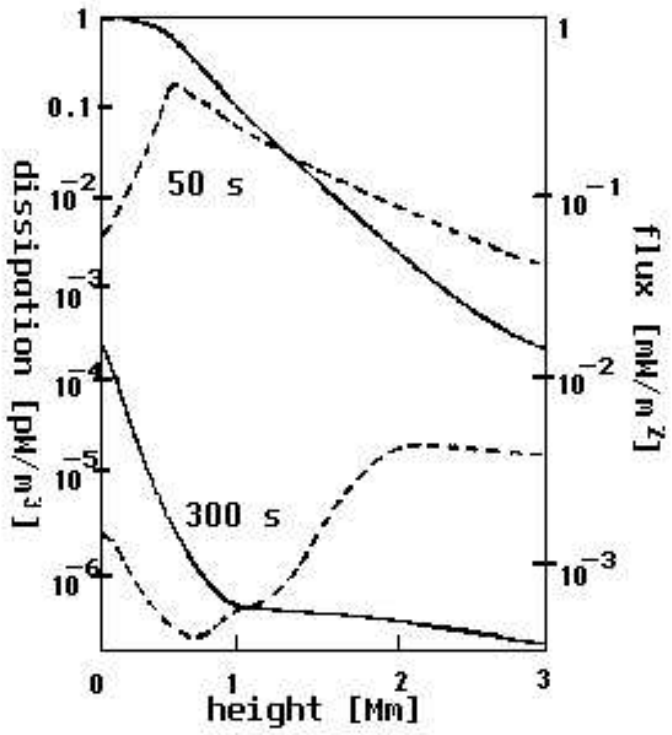

Figure 1.1: Behaviour of waves with height with thermal conduction neglected. Solid lines represent flux, dotted lines dissipation, (Stein & Leibacher 1974).

1.2 Acoustic waves

Below the photosphere, a convective layer exists from which overshooting plasma is visible as the 'solar granulation' (see Fig. 1.2). There are several possibilities how the convection zone may generate the wave modes in the atmosphere: a) convective motions penetrate into atmospheric layers and directly deposit their energy; b) pressure fluctuations, generated by convective motions, propagate as acoustic waves; c) thermal over-stabilities, which occur in the upper layers of the convection zone, generate waves.

The second possibility is widely accepted as the method of generation of acoustic waves. The generation of acoustic waves can be described by the 'Lighthill mechanism' (Lighthill 1951). The most energetic oscillations should be generated in those regions where the convective velocities are largest. The more detailed explanation one can find also in (Proudman 1952) and (Stein 1967). Some authors argue that short-period bursts are either generated by rising granules, or propagate more or less uniformly from deeper layers into the convection zone (Deubner & Laufer 1983). Although there is a general consensus that the source of acoustic waves is convective motion, some authors argue that one can not decide whether their origin is convective or magnetic. The observational and the theoretical results do not reveal a clear picture of the source of the solar oscillations (Moretti et al. 2001).

The frequencies of the acoustic waves depend on various parameters of the fluid flow:

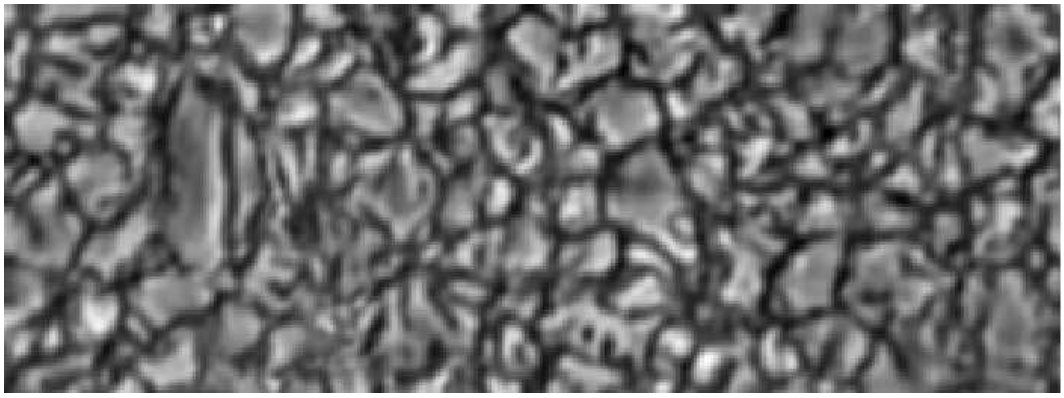

Figure 1.2: One of the broadband images taken with the Vacuum Tower Telescope (VTT) at the Observatorio del Teide (OT), Tenerife, after speckle reconstruction. One can see the granulation pattern of surface convection. The field of view is $30.5'' \times 11''$.

If v is the typical flow velocity, l the typical linear dimension, and ν the typical frequency, then the non-dimensional product $\nu l/v$ (the Strouhal number) varies less with changing conditions of the flow than ν itself. But taking frequencies proportional to v/l can give a preliminary and rough idea of how the acoustic wave production varies with the constants of the flow (Lighthill 1951).

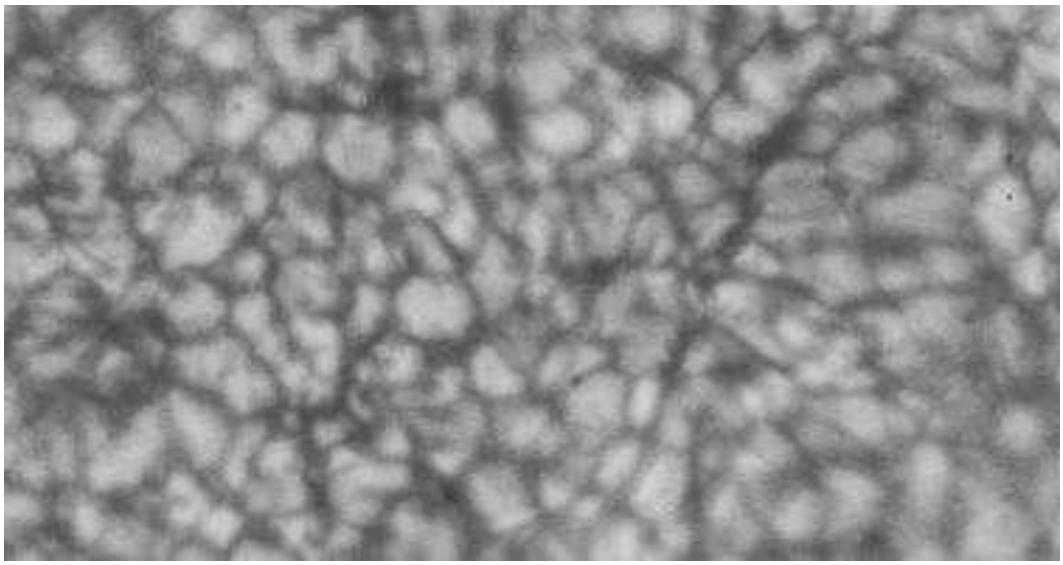

Figure 1.3: One of the broadband images taken with the German VTT at OT, Tenerife, without speckle reconstruction. Image degradation (e.g. at the lower right side) is caused by atmospheric turbulence, 'seeing'. The field of view is approximately $38'' \times 20''$.

The surface of the Sun is covered by adjacent granules of apparent sizes between 1" (1500km) to 3"(2250km), as can be seen in Fig. 1.3 and 1.2. Observations (Espagnet et al. 1996) show that the acoustic events occur preferentially in the dark intergranular lanes, i.e. correspond to down flows of plasma. This leads to the conclusion that the excitation

of solar waves is associated with a rapid cooling occurring in the upper convection layer. Indeed, events which last a few minutes and extend over an area of a few arcsec have been detected to follow a darkening and a collapse of the plasma which is localized in the intergranular lanes (Espagnet et al. 1996). The most energetic waves are associated with those down-flows in dark areas which are well separated from each other in time and space (Espagnet et al. 1996). Some observers noticed strong waves following expansions of intergranular spaces. There is observational evidence that acoustic waves tend to be converted into magneto-acoustic waves at locations where a magnetic field is expected, e.g. at granular boundaries or in bright points (Espagnet et al. 1996). There are also suggestions about a transition from acoustic waves in the centres of supergranulation cells to fast magneto-acoustic waves at the boundaries of supergranulation or chromopshere network. (Kalkofen 1990)

Kalkofen (1990) suggests that the location of acoustic waves should depend on their frequency. In areas of strong magnetic fields at the cell boundary, Kalkofen calculates that heating is done by waves of $6 - 12$min periods. The bright points are heated by waves with periods around $3min$; locations free of magnetic field will be heated by waves of still shorter period.

1.2.1 Propagation

In the solar atmosphere the acoustic transit time is approximately 5 minutes (for a height of 2000km and a sound speed of 7kms^{-1}), which match with the period of the 5min oscilations. For a propagation of acoustic waves in the solar atmosphere over several scale heights, their frequency has to be above the cut-off frequency:

$$\omega_{ac} = \frac{\gamma g}{2c_s}, \tag{1.8}$$

where g is the gravitational acceleration, $\gamma = c_p/c_v$ is the adiabatic coefficient and $c_s = \sqrt{H\gamma g}$ is the sound speed, with H as density scale height:

$$H \equiv \frac{-\rho_0}{\frac{d\rho_0}{dr}}, \tag{1.9}$$

(see: Stix (2002), chapter 5.2.4). The cut-off frequency varies with the height in the atmosphere since g and c_s are not constant. Thus, at a certain height in the atmosphere a reflection layer exists where the values of g and c_s yield the appropriate cut-off frequency. For a given frequency, a wave can be propagating at one height and be evanescent at other. This means that for waves of different frequency, the atmospheric conditions - temperature and density stratification form reflection layers at different heights. Waves can freely propagate below the reflection layer where their frequency reaches the local cut-off frequency. At the corresponding reflection layer they are reflected downwards. This situation can cause standing waves for almost the whole range of acoustic waves. Fleck et al. (1989) explain that there is a possibility for standing waves, originating from the total reflection of upward propagating waves at the chromosphere - corona transition region. This discovery of standing patterns was confirmed by Espagnet et al. (1996).

Waves with a frequency above the atmospheric cut-off frequency ω_{ac} (Eq. 1.8) propagate across the temperature minimum towards the chromosphere and corona. As long as

the wave amplitude is small, the energy flux associated with propagating waves F_w is

$$F_w = c_s \rho v^2, \tag{1.10}$$

where c_s is the speed of sound, ρ the mass density, and v the velocity fluctuation of the gas. Since $F_w = const.$ and c_s depends only weakly on the temperature we have $v^2 \propto \rho^{-1/2}$ meaning that the velocity fluctuations increase through the chromospheric layers. We can assume that c_s is constant above 1Mm. For small amplitudes, we have $v \ll c_s$.

During propagation through the solar atmosphere the velocity amplitude increases with decreasing density. The wave crests start to travel with different velocities as compared to wave valleys. This yields a deformation of the wave affecting a saw tooth shape and the creation of a shock front where the energy is dissipated; an illustration of this process can be seen in Fig. 1.4.

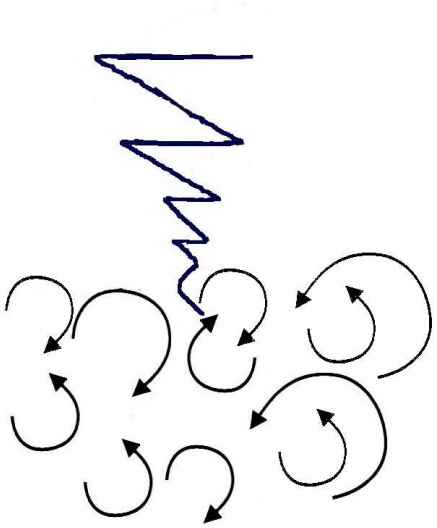

Figure 1.4: Sketch of acoustic-wave propagation through the solar atmosphere.

The propagation of waves through the atmosphere will cause a height-dependent variation of its frequency. These changes are caused by the resonance property, the merging of shocks, and from shocks 'cannibalizing' each other. As a consequence of this behaviour, the spectrum develops at 2000 km height into almost pure 3 minute spectrum. Above 5000 km, the chromosphere reaches a dynamical steady state where the mean temperature is time-independent (Ulmschneider 2003). The acoustic wave then travels on top of this mean temperature, while its shock dissipation continuously provides the energy for the chromospheric radiation losses.

1.3 Magnetic field effects

One usually defines as quiet Sun those areas where the solar magnetograms do not show locations where polarisation signals exist. But recent research (Domìnguez 2004) has

shown that the quiet Sun is not at all magnetically quiet. Indeed, besides the visible magnetic structures, there are also the magnetic knots. Their life time is approximately one hour and they typically appear in dark intergranular lanes; and therefore can be associated with the down-flow motions. Magnetic knots are flux concentrations and can be seen in the spectrum as the line gaps.[4] Therefore, in those areas one can expect strong mixture of the acoustic waves and Alfvén waves.

It was general consensus that the magnetic field in the quiet Sun around $B \sim 10^{-4}$T and for active regions it is assumed that magnetic field has values from $B \sim 0.1$T till $B \sim 0.3$T in Sunspots (Stix 2002). In a recent analysis of the quiet Sun magnetic fields, Domìnguez (2004) observes elements in the quiet Sun with magnetic field strengths of the order of 0.1T, and that 45% of the areas having the magnetic field around $B \sim 10^{-3}$T.

In magnetic locations, the waves may travel with Alfvén speed. The velocity for Alfvén waves can be calculated with the expression:

$$v_A = \sqrt{\frac{B^2}{4\pi\rho}}, \tag{1.11}$$

where B is the magnetic field and ρ the density of the atmosphere. It is clear that the velocity of Alfvén waves will follow variations in the magnetic field.

The correlations of chromospheric losses with concentrations of the magnetic fields suggest that the field should play a role in the heating. In a flux tube, the analogue to the ordinary acoustic wave is the longitudinal tube wave. Longitudinal tube waves are produced by fluctuating compressions of the magnetic tubes. They are very similar to acoustic waves and develop into shocks, which heat the tubes by dissipating the wave energy. The main influence of the magnetic field comes from its geometric shape which channels the propagating wave. The narrower the channelling, the stronger the upwards increase of the amplitude, and therefore the deeper the level where shock formation and heating occurs.

1.4 Short-period waves

In the previous few years, short-period waves were detected. But it was not clear whether they are propagating through the atmosphere and carry enough energy flux to cover the needs of the chromosphere. Hence, an analysis of short-period waves was necessary.

Ulmschneider (1971b) predicted the maximum of the transported energy for the waves of periods from 20 to 40s. Therefore, the increase of the energy amount is expected when approaching to these periods. To detect waves of such short period in such specific locations high spatial and temporal ground based observations were done since only that kind of observation can give required details. As most interesting quantity, the amount of energy they carry, needed to be established. Additional quantities of short-period waves could give a more complete image of the mechanism for the heating of the chromosphere.

This work is based on the work of (Wunnenberg et al. 2003) who opened the possibilities to investigate this matter in future.

[4] For more details see: Stix (2002) section 8.2

2 Observations

2.1 Aim of the observations

Short-period waves are thought to carry the energy needed for the heating of the chromosphere. Their detection and analysis is a vital step in solving this puzzle about heating.

Short-period waves are spatially small events and their temporal changes are quite rapid. In order to observe such short-period waves one needs high spatial and temporal resolution. The high temporal resolution requires a fast repetition rate; a high spatial resolution is achieved from best observations combined with special techniques for data reduction.

2.1.1 Choice of the spectral line

Since acoustic waves are supposed to heat the chromosphere, the first request was to obtain information which is not influenced by the magnetic field. To prevent strong thermal broadening, spectral lines of elements with large atomic mass should be chosen. Taking all these items into account an optimal choice for the spectral line is Fe I 543.45nm. Calculated response functions (see Sect. 3.2.2) show that its line-core is formed near the temperature minimum at height of 600km above $\tau_{cont} = 1$ where the wavelenght of the continuum optical depth τ_{cont} is 500nm.

Table 2.1: Data for the spectral line Fe I 543.45nm

The strong iron line	
Wavelength	543.4534 nm
Multiplet	15
Transition	${}^5F_1 \rightarrow {}^5D_0$
g_{eff}	0
χ_{low}	1.01 eV
$W_\lambda^\odot$	18.4 pm

In the chronological order, the first set of data used in this work, DS1, containing the non-magnetic spectral line Fe I 543.45nm (Table 2.1) was taken by J.K. Hirzberger and M. Wunnenberg during August 2000. These observations were done near the solar disc centre in a region without any G-band structures, i.e. far from any activity centre.

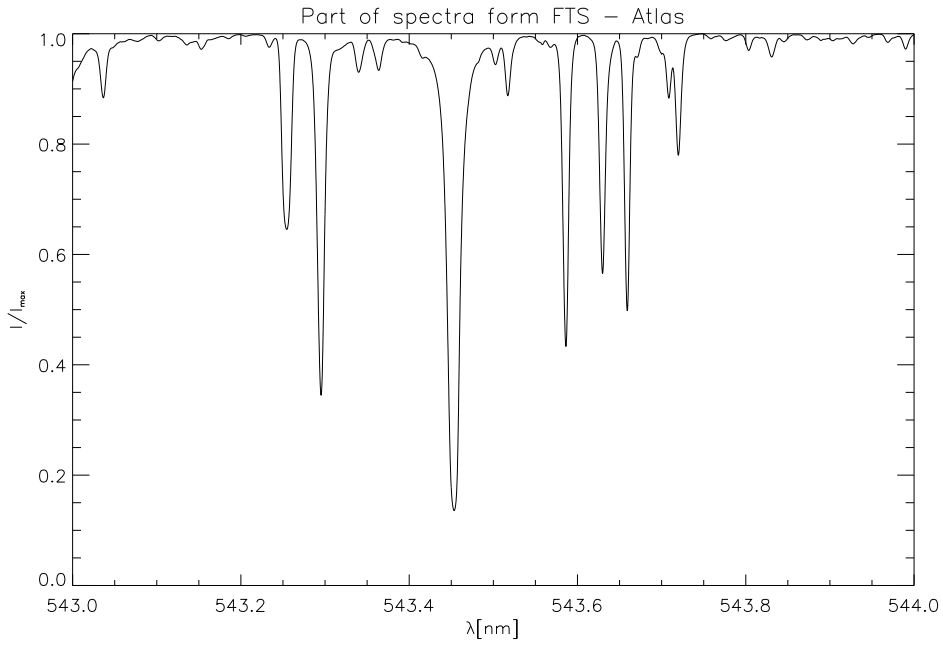

Figure 2.1: Observed lines Fe I 543.45nm and Fe I 543.29nm and their neighbourhood extracted from FTS Atlas.

Table 2.2: Data for the spectral line Fe I 542.29nm

The fainter iron line	
Wavelength	543.2955 nm
Multiplet	1143
Transition	${}^5G_2 \rightarrow {}^5F_2$
g_{eff}	0.667
χ_{low}	4.44 eV
$W_\lambda^\odot$	7.2 pm

For the next campaigns, two lines were used, Fe I 543.45nm (Table 2.1) and the slightly Zeeman-sensitive Fe I 543.29nm (Table 2.2) which has a Landé factor of 0.667. During the last campaign we planned to obtain also magnetic information, but bad weather conditions did not allow these observations. Fig. 2.1 shows the used lines and their spectral neighbourhood extracted from the Fourier Transform Spectrometer Atlas of the Sun (Neckel 1999).

Restriction from the line choice

Usually, strong lines form at great height and weak lines near the solar surface [1]. The main contribution to lines stems from a height interval of about $\Delta z = 300$ km. If the

[1] Definition of the term surface can be found at the beginning of Sect. 1

length of the acoustic waves is smaller than Δz the line shows no wavelength fluctuations but only a line broadening. This fact limits observations to waves with periods greater than $\approx$ 40s, taking 7 km/s as sound speed (Ulmschneider 2003), and largely influenced our choice of spectral lines used to obtain relevant data: a strong one from high and a fainter one from deeper layers.

Direct information about the magnetic field was not available, since the lines were just selected for their insensitivity to the Zeeman effect. However, indirect information may be deduced from the residual intensity effect (see Sect. 6.3).

2.2 Instrumentation

For the present study I needed data which combine high temporal and spatial resolution and, at the same time, give information about the spectral behaviour of the line.

An instrument which can provide all those requirements is the German Vacuum Tower telescope (VTT) on the Canary Islands, with an appropriate post-focus equipment.

Figure 2.2: Observational site on island Tenerife, Spain (USW web page)

2.2.1 Telescope

The VTT was installed in 1987 at the 'Observatorio del Teide' on Tenerife, see Fig. 2.2, at a height of 2400m above sea level. Since time sequences are necessary for this work, the good weather conditions are a primary condition mostly fulfilled by this telescope. One of the major reasons for the choice of a telescope location is the astronomical quality of the atmosphere above the site. Certain conditions in the Earth's atmosphere cause an image flickering; this phenomenon is called "seeing", it depends on a large number of factors, as for any gaseous atmosphere [2]. Some factors can be influenced to a certain extent by the choice of the site. Telescopes are usually built on mountains, where the atmosphere above

[2]The Earth atmosphere itself is a chaotic system.

the telescope is less extended than at sea level. At the Canaries, telescopes are additionally located above the mean height of the cloud layers. Another factor is the wind which may remove atmospheric turbulences. Long distance influences of the Earth's atmosphere are further improved by the location on an isolated island far from larger land masses. For solar telescopes it is additionally useful to have surroundings which are not much heated during the day. Heating of the immediate telescope surrounding is minimized by reflective material and white colour of the building.

The VTT (see Fig. 2.3) was built on such an appropriate site. It is located at $16^o30'35"$ geographical longitude and $28^o18'00"$ latitude, thus often exposed to trade winds. Several hundred meters below the telescope, a stable cloud layer usually forms a helpful temperature inversion layer.

Figure 2.3: Open dome of VTT (Vacuum Tower Telescope)

The VTT is equipped with a coelostat system, having two mirrors of 80cm size. The main imaging mirror has 70cm diameter and a focal length of 46m. The main optical path is protected by a vacuum tube preventing air convection due to the vertical temperature stratification in the most sensitive parallel beam.

2.2.2 Post-focus setting

As mentioned above, this work requires data which will contain spectral information. Two-dimensional spatial maps at several spectral positions in the line profile appeared to be optimal for the present work. Besides a fast repetition rate between scans through the line are required. A post-focus instrument which meets all the requirements is the Göttingen Fabry-Perot spectrometer (Bendlin et al. 1992). With this instrument, and an appropriate set of reconstruction methods, the high temporal and spatial resolution necessary for my work could be achieved.

The Göttingen Fabry-Perot is located in the optic laboratory No. 2 of the VTT. The light from the main path of the telescope is deflected into that 'OL2' by means of a 45^o mirror. The complete scheme of the post-focus setting is shown in Fig. 2.4.

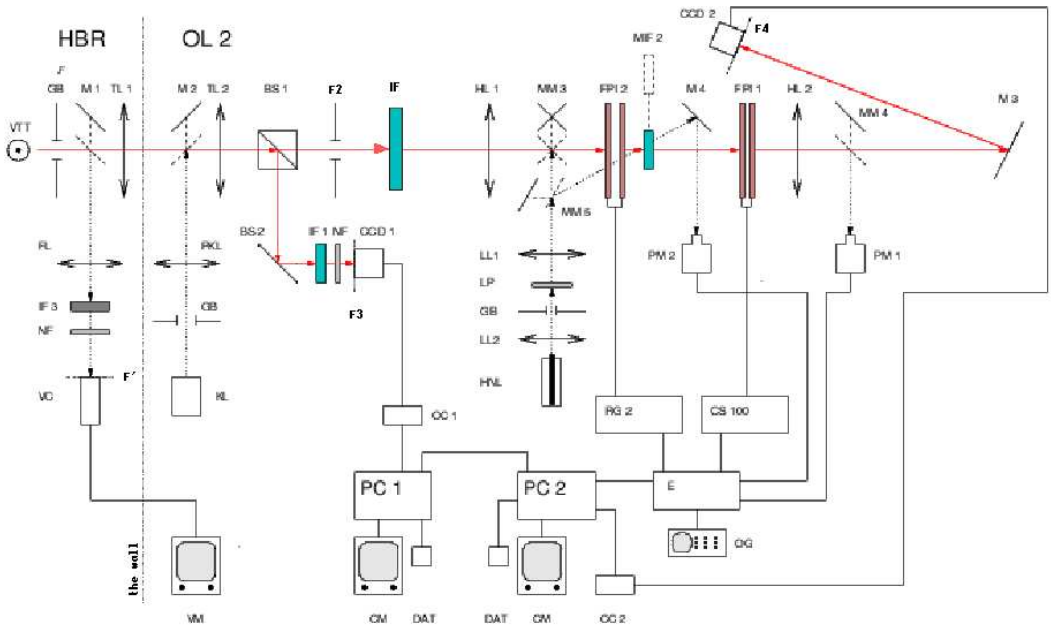

Figure 2.4: Schematic view of post-focus settings used to obtain the data for this work.

The scheme of Fig.2.4 shows the instrumentation in two rooms, the main observing room and the optic laboratory No.2, both are separated by the dashed line marked as 'the wall'. Those parts of the instrumentation located in the main observing room, marked as HBR, consist of a mirror M1 which deflects the light to a camera, an imaging lens and two filters, the one marked IF3 being a 'G-band filter' (i.e., set at the CH absorption near 430nm). This part of the equipment is used to initialise the equipment and to choose a location on the Sun.

The part of the instrumentation located in the OL2, contains the main instruments to obtain data. The incoming light is directed from the VTT focus F, through two lenses, TL1 and TL2, to a beamsplitter BS1 which transmits 95% of the light to a narrowband filter and deflects 5% to a broadband filter. The latter part passes an interference filter marked as IF1 and then a neutral filter, NF. The image of this part is recorded by a CCD detector, marked CCD1. The larger part of incoming light feeds the narrowband beam, first producing a secondary image F2, where one of the diaphragms is located. Behind that focus, another interference filter, IF, is located, followed by a lens, HL1, and two Fabry-Perot interferometers, marked as FPI1 and FPI2. Finally, lens HL2 and mirror M3 image the filtered light onto CCD2.

Part of the left side of the schematic view, starting with the mirror M2 is used to take images with an artificial light source, required for the data reduction. During the actual

observations, mirror M2 is outside the beam. Mirrors MM3 and MM4 with adjoining equipment are used for fine tuning of the FPIs.

Both cameras are slow scan ones and have Thompson TH 7863 FT chips with 384×286 pixels. FPI1 is a Queensgate etalon 'ET 100' with an aperture of 50mm, 125μm spacing and a finesse of $\mathcal{F} \approx 40$. FTP2 has an aperture of 35mm, its spacing can vary from 100μm to several mm. It has a finesse of $\mathcal{F} \approx 30$ and is manufactured by Burleigh Instruments Ltd (Koschinsky et al. 2001). Reflections between two FPIs can cause reflexes on CCD2; to avoid this, FPI1 is slightly inclined against the optical axis. Some additional information about the FPI can be found in Appendix A.

2.3 Data

In this work data sets from several observation campaigns were used. The direction of the FPIs scanning was done for all lines from the red to the blue. The data set, DS1, was taken by J.K. Hirzberger and M. Wunnenberg during August 2000 (Wunnenberg 2003). The rest of the data sets were taken during observational campaigns in the years 2003 and 2004, see Table 2.3. The main objective was to achieve the fastest repetition rate possible, allowing to study waves with shortest periods. Since the time evolution of short-period waves was of main interest, reasonably long time sequences were taken.

Table 2.3: Dates, used lines and object of observation for obtained data sets.

Data Sets			
mark	date	line used	object of observation
DS2	08.10.2003	543.45 nm and 543.29 nm	quiet Sun, disk centre
DS3	22.06.2004	543.45 nm and 543.29 nm	quiet Sun, disk centre
DS4	24.06.2004	543.45 nm and 543.29 nm	quiet Sun and G-band structures disk centre
DS5	25.06.2004	543.45 nm and 543.29 nm	pore, disk centre
DS6a	26.06.2004	543.45 nm	quiet Sun, disk centre
DS6b	26.06.2004	543.45 nm	pore, disk centre
DS7	28.06.2004	543.45 nm	quiet Sun and G-band structures disk centre

During the October 2003 campaign it was decided to observe with two lines. The main reason was the expectation that noise will less influence the final results if two lines formed at different heights are used. The spectral lines Fe 543.45 nm and Fe 543.29 nm which originate from different heights and are not essentially affected by Zeeman splitting were finally chosen. Although Fe 543.29nm has a Landé factor $g = 0.667$, it does not allow to deduce quantitative information's about the magnetic field. The data were obtained with the help of K.G. Puschmann. Because of unfavourable weather conditions we got only one set of data in that campaign. The observations were done at the solar disc centre far away from active regions which would be visible as G-band structures. Detailed information about that data set can be found in appendix B.1.

In the campaign of June 2004, the adaptive optics (Berkefeld & Soltau 2001, Soltau et al. 2002) could be used; these data sets were obtained with the help of J.K. Hirzberger, S. Stangl and K.G. Puschmann. During this campaign some data sets were taken with one and some with two lines (see Table 2.3). Additional details about each data set obtained with two lines can be seen in Table 2.4. During this observation campaign various solar regions were observed. To determine the correct area the equipment from HBR is used. The areas which showed neither G-band structures nor other magnetic activity were chosen as the Quiet Sun. For the active areas the field of view with the pores and with large number of G-band bright points were chosen. The coordinates represent the position of the field of view, in arcsec, where the reference point is the centre of the Sun. During the take of data the FPIs move through the selected spectral line with previously determined steps. The number of steps and the position in the line where the FPI will pause for taking images is pre-determined. Those numbers of places in the line are in Table 2.4 and 2.5 marked as line positions. One complete FPI pass through the spectral line is called scan. The FPIs have a limited range of scanning. In the case that more than one spectral line will be scanned, it is sometimes necessary to skip the area between the lines. To achieve that, the FPIs are set to perform a jump. At the given line position the FPIs jump over the predetermined distance. The cadence indicates the repetition time of the FPI scans through the total spectral range.

Table 2.4: Details for obtained data sets for two lines.

Data Sets						
mark	coordinates [arcsec]	images per scan	line positions	exposure time [ms]	jump at	cadence [s]
DS2	$[0, 0]$	108	18	30	10	27.4
DS3	$[0, 0]$	108	18	30	10	28.2
DS4	$[0, 0]$	108	18	30	10	28.4
DS5	$[0, 0]$	108	18	30	10	28.3

Since the repetition rate of data sets with two lines was rather low, I took additional data sets with only one line to achieve a faster repetition rate, see Table 2.5.

Table 2.5: Details for obtained data sets for one line.

Data Sets					
mark	coordinates [arcsec]	images per scan	line positions	exposition [ms]	cadence [s]
DS6a	$[96.7, 90.7]$	91	13	20	22.7
DS6a	$[19.8, -45]$	91	13	20	22.7
DS7	$[6, 0]$	91	12	20	29.9

The last data set, DS7, was taken to check whether the number of images per scan has

a large influence on the data quality. Information about some of data sets from campaign of 2004 can be found in Appendix B.2.

2.3.1 Observations

The equipment and the data acquisition system are designed to satisfy requirements of the speckle reconstruction. With the help of the speckle reconstruction the spatial resolution can be improved.

Each data set contains one time sequence and consists of the broadband and the narrowband images. Narrowband images contain the required information about spectral lines, while broadband images are taken for reconstruction purposes. For the latter, the both sets of images, the broadband and the narrowband are taken simultaneously.

A precondition for successful reconstruction of data is the consideration of the dark and flat field matrices as well as the total transmission. Only after acquiring all the necessary matrices and the data set, a speckle reconstruction can be done.

Dark frames

CCD dark frames are images taken with the shutter closed with the same exposure time as that for the object frames. These are used to correct the data for e.g. 'hot' or bad pixels, and allow to estimate the thermal noise of the CCD, as well as the rate of cosmic ray strikes at the observational site. Multiple dark frames are averaged to produce a final dark calibration frame. We usually take one or two scans, with 20 images per scan.

Flat fields

Flat field images are taken by moving the telescope pointing in a 'random walk' mode to average any solar structure. For a reconstruction of the narrowband images, flat fields were also taken with defocused telescope. Flat fielding must be done for each wavelength region and particular instrumental setup in which object frames are taken (Howell 2000). For our observations we usually take 20 scans for the ordinary flat field, each with the same number of images per scan as for main data sequences and one or two scans with defocused telescope. Flat field exposures are used to correct for pixel by pixel variations in the CCD response as well as for a non-uniform illumination of the detector.

Transmission curve

For each observational campaign and in case of any additional experimental or altered line setting, we took narrowband images with a halogen lamp as a continuum light source. This is done to correct the narrowband images for the transmission curve of the pre-filters.

3 Data reduction and analysis methods

The final analysis of the data is done by means of velocity maps. In order to obtain highest spatial resolution in two-dimensional images, the influence of seeing has to be removed. An example of the ”raw” data is shown in Fig. 3.1; it can be seen that the contrast and brightness of the image are not constant over the field of view. Patches of unsharpenes are caused by atmospheric seeing. This problem is most effectively removed by speckle reconstruction.

From the reconstructed images at different position in the spectral line velocity maps are calculated. Since it is important to resolve the flows also in vertical direction we combine the data such that the height range which contributes to the velocity map is as narrow as possible.

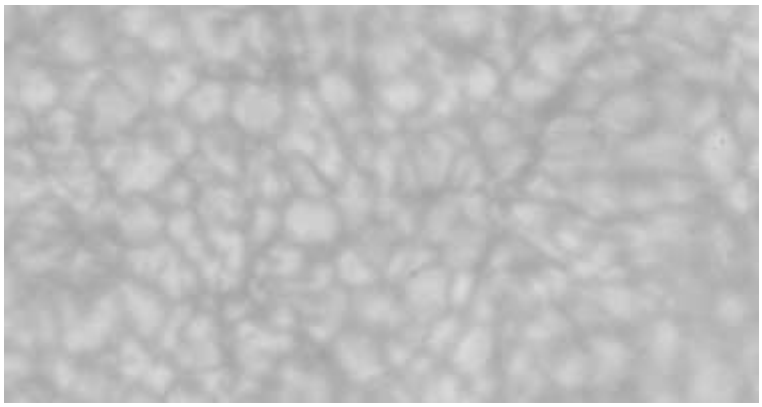

Figure 3.1: One of the ”raw” broadband images from data set obtained at August 2000.

3.1 Data reduction

The data reduction is done in two major steps, each performed by separate sets of programs written in IDL. The data for the broadband images are taken from CCD1. The same number of images is taken with the two FPIs on CCD2, simultaneously with the CCD1 images, and has therefore the same atmospheric distortion. The CCD1 images are taken in the integrated light of a spectral region covered by the interference filter IF1. The program used for this step was developed by de Boer (de Boer et al. 1992, de Boer & Kneer 1994).

The CCD2 provides spectral resolution by scanning through the spectral line in a previously determined number of steps (see Sect. 2.3), with an appropriate number of the images per wavelength position of the FPI. The number of images per line profile position depends on the quality of seeing during the observations. The better the seeing, the fewer images per position are necessary; and vice versa. One of the main guide lines for the total image number is the speckle reconstruction, which requires approximately one hundred images per data scan. The program set used for this reconstruction was developed by Janssen (Janssen 2003).

3.1.1 Speckle reconstruction

Speckle interferometry can improve the angular resolution, down to the diffraction limit of the telescope. The term speckle describes the grainy structure observed when a laser beam is reflected from a diffusing surface. This structure is a result of interference effects in a coherent beam with random spatial phase fluctuations. The grains can be identified with the coherence domains of the Bose-Einstein statistics. The speckle-affected image contains more information about smaller features than a long exposure image or an average image with blurred speckles (Labeyrie 1970).

The speckle interferometry is based on the analysis of a sequence of short-exposure images observed with a telescope. The exposure time should be shorter than the time scales of atmospheric changes, i.e. typically of the order of $10 - 50$ms. The images differ since the state of the atmosphere changes continuously; but every image contains a part of the information of the small angular structure of the observed object. Averaging of the images loses this kind of information, but it can be recovered using speckle imaging methods (von der Lühe 1993).

The astrophysical image can be represented by the equation :

$$i(\boldsymbol{x}) = o(\boldsymbol{x}) * s(\boldsymbol{x}), \tag{3.1}$$

where $o(\boldsymbol{x})$ is the true image and $s(\boldsymbol{x})$ is the point spread function, PSF. The PSF contains the effects of the telescope and of the atmosphere. Transforming Eq. 3.1 into the Fourier space, we can write :

$$\frac{1}{N}\sum_{j=1}^{N} I_j(\boldsymbol{u}) = O(\boldsymbol{u}) \cdot \frac{1}{N}\sum_{j=1}^{N} S_j(\boldsymbol{u}), \tag{3.2}$$

where $\frac{1}{N}\sum_{j=1}^{N} I_j(\boldsymbol{u})$ is the long exposure image with degradation, O is the Fourier transform of the true image and $S_j(\boldsymbol{u})$ is the instantaneous Optical Transfer Function, OTF.

The atmospheric turbulences introduce varying phases in the OTF, therefore averagind the OTFs results in the cancelling of some of the amplitudes and causes a loss of information at higher frequencies.

The method for recovering that information, proposed by (Labeyrie 1970), replaces the individual terms in Eq. 3.2 with their square modulus :

$$\frac{1}{N}\sum_{j=1}^{N} |I_j(\boldsymbol{u})|^2 = |O(\boldsymbol{u})|^2 \cdot \frac{1}{N}\sum_{j=1}^{N} |S_j(\boldsymbol{u})|^2. \tag{3.3}$$

The average of $|S_j(\boldsymbol{u})|^2$ is called Speckle Transfer Function, STF. In solar observations, the STF depends only on the seeing conditions and is gained from a model of turbulence in the Earth's atmosphere. The STFs are evaluated with the Fried parameter r_0 (Korff 1973) which is obtained with the spectral ratio method (von der Lühe 1984). This kind of calculation requires at least 100 speckle images.

The STF and equation 3.3 give the amplitude of the image in the Fourier space. The speckle masking method gives the information about the phases at each frequency, (Weigelt 1977), (Weigelt & Wirnitzer 1983). The bispectrum is defined as :

$$BS(i,j,k,l) = \langle I(i,j) \cdot I(k,l) \cdot I(-i-k,-j-l) \rangle, \tag{3.4}$$

where $i,j,k,l = -N/2,\ldots,N/2$. When averaged over a sufficient number of OTFs, Eq. 3.4 gives a real non-zero function, therefore containing only the object phases. The result is a four-dimensional array containing multiplications with different displacements of the images in Fourier space. With the starting conditions :

$$\phi(0,0) = 0, \tag{3.5}$$
$$\phi(0,1) = f_1, \tag{3.6}$$
$$\phi(1,0) = f_2, \tag{3.7}$$

(where f_1 and f_2 are phases obtained from the original data using the fact that phases at low frequencies are well known) and the equation :

$$e^{\mathbf{i}\phi(i+k,j+l)} = e^{\mathbf{i}\phi(i,j)} e^{\mathbf{i}\phi(k,l)} e^{-\mathbf{i}\Phi(i,k,j,l)}, \tag{3.8}$$

(where $\Phi(i,k,j,l)$ are the phases of the bispectrum) one can recover the phases.

The speckle imaging process usually consists of two passes through the data. A first pass estimates the prevailing seeing conditions and constructs a noise filter. Also, the Fried parameter is calculated in this first pass. In the second pass the speckle imaging is performed. In order to prevent artefacts due to anisoplanatism the size of the reconstructed field is reduced. Each image is cut into overlapping segments. Those segments are treated independently and after complete reconstruction they are combined into one image of the full field of view.

Two major sources of noise contribute to the reconstructed image, one is the speckle process itself, and the other is the photon noise. The noise introduced by the speckle process itself can be reduced when increasing the number of averaged frames which are used for the reconstruction, in frame registration; (see von der Lühe 1993). The statistics of the normalized error of the complex Fourier transform of the reconstructed image can be approximated by a circularly complex random process with equal variance in the real and the imaginary parts. Besides the speckle process, many sources in the detection process contribute to the noise, but due to the luminosity of the Sun the photon noise is the largest component. This source is not connected with the OTF but it results in a bias which needs to be corrected. The photon noise contribution to the total error is comparable to the speckle noise contribution. So in total, a random photometric error is less than 1% if the rms contrast of the reconstruction is 10% (von der Lühe 1994). The reconstructions obtained from a continuous data run under not so good seeing conditions should be regarded with caution (von der Lühe 1994).

The code which uses the procedure was developed in USG solar group, by de Boer (thesis) and others.

3.1.2 Reconstruction of the narrowband images

The narrowband data contain a set of images per previously defined number of wavelength position in the line. This means that there are fewer images from which information can be extracted as compared to the broadband image series. Since the object of observation is seen though the same turbulent atmosphere, the narrowbandreconstruction use the instantaneous OTF known from the already reconstructed broadband data. This procedure is based on a method developed by Keller and von der Lühe (Keller & von der Lühe 1992).

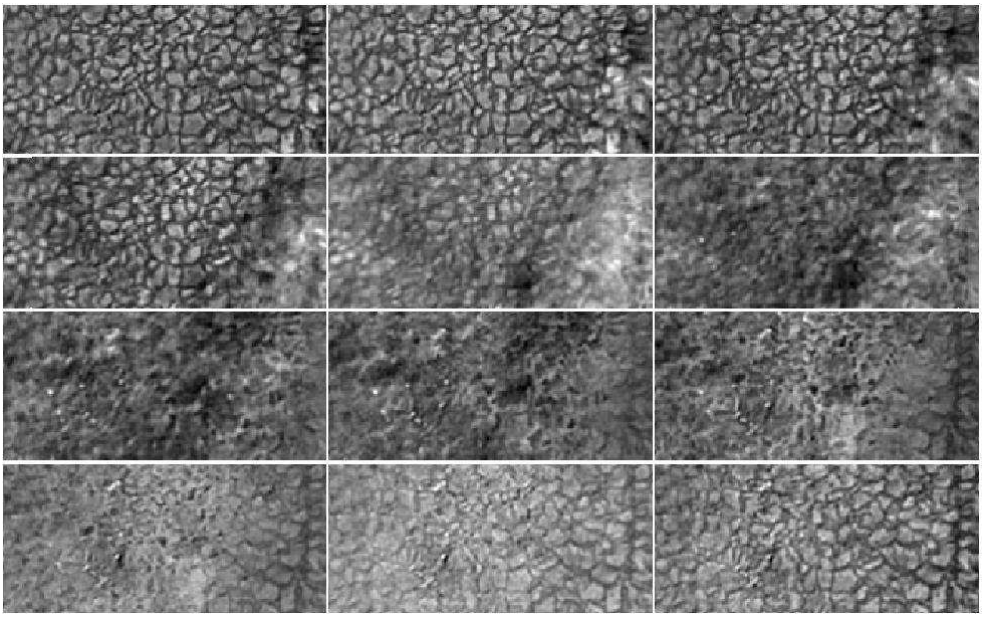

Figure 3.2: A reconstructed narrowband scan, for the spectral line 543.45 nm in 12 positions of the line profile. The blue shift of the maximum FPI transmission across the field of view is not yet removed.

If $\hat{O}_n$ is the estimate of the narrowband image and $\hat{O}_b$ is the already reconstructed estimate of the broadband image, the formula used for the reconstruction is:

$$\hat{O}_n = H \frac{\sum_j I_{nj} I^*_{bj}}{|I_{bj}|^2} \hat{O}_b, \tag{3.9}$$

where H is a noise filter, $I_{nj} = S_j \cdot \hat{O}_n$ the image in the Fourier space at the individual wavelength position $j = 1, \ldots M$, and M the number of images per position, S is the OTF, and $I_{bj} = S_j \cdot \hat{O}_b$ the respective broadband image. The noise filter can be calculated as an optimum filter, considering the noise level in the flat field frames and the corresponding light levels (Krieg et al. 1998).

The speckle imaging of the narrowband images is severely degraded by noise in the individual frames (Keller & von der Lühe 1992). One of the ways to reduce this degrada-

tion is to construct the best possible noise filter. Detailed work about the noise filtering was described by (de Boer 1996). In our case, additional improving of the filter is done by taking a large number of flat fields, around 20 scans during the process of the reconstruction. This procedure is done to obtain a flat field which does not contain any traces of the observed granular structures but only the disturbances introduced by the equipment.

In Fig. 3.2 one can see a reconstructed narrowband scan. The top left side corresponds to the red wing of the line, the 6^{th} image shows the line core, and the bottom right image the blue wing of the line.

3.2 Determination of the heights

In order to analyse the dynamics of the chromosphere, calculations of the velocities are required. This is done with the help of the Doppler formula:

$$v = \frac{\Delta\lambda}{\lambda_0} \cdot c, \tag{3.10}$$

where $\Delta\lambda$ is the shift of the wavelength, λ_0 is the laboratory wavelength and c the speed of light. The equation 3.10 is used for calculation of velocity maps for this work, and $\Delta\lambda$ is determined with the help of bisectors (see Sect. 3.2.1).

3.2.1 Bisectors

The bisector is a curve which divides the line profile into two parts. In the ideal case of a symmetric line profile the bisector would be a straight vertical line. Due to Doppler shifts and physical parameters of the solar atmosphere, the line profile is usually asymmetric, and the bisector thus curved.

3.2.2 Response functions

One of the aims of this analysis was to determine the behaviour of acoustic oscillations with increasing height. Therefore it was necessary to perform calculations which yield only oscillations produced in a certain height interval. The calculations necessary for this purpose are done with response functions (Eibe et al. 2001, Pérez Rodrìgues & Kneer 2002).

If we suppose that a certain physical quantity, in our case the radial velocity, v is disturbed by a small quantity $v(z,t)$ which depends on the height and the time, the fluctuations can be written as:

$$v_{ob,\lambda} = \int_{-\infty}^{\infty} RF_v(\lambda, z)v(z)dz, \tag{3.11}$$

where λ is the wavelength, $v_{ob,\lambda}$ is proportional to the Doppler shift at the same wavelength and $RF_v(\lambda, z)$ is the weighting function (Mein 1971), in our case the response function, associated to the physical quantity in question. This weighting function is computed by successively disturbing the model of the atmosphere in certain levels of increasing altitudes. This response function can be used to determine the formation height of the observed velocities.

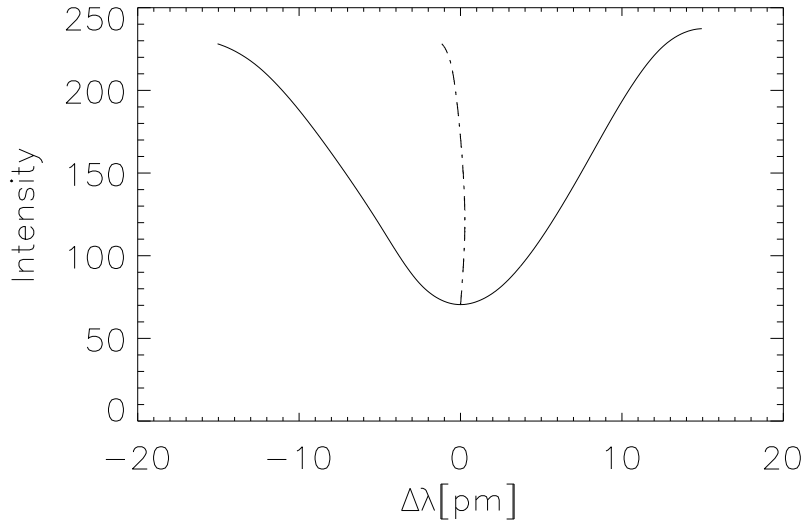

Figure 3.3: Example of the calculated bisector for a line profile. The line profile is represented by the solid line, and the bisector by the dash-dotted line.

The velocity response functions in this work are calculated with the software developed by F. Kneer. I will here describe the calculations done for the line Fe I 543.45nm. Using a model of the solar atmosphere by (Holweger & Müller 1974) calculations are done for 95 different heights, from -73km to 886km, where zero is the level with unity optical depth in the continuum at 500nm $\tau = 1$. It is assumed that fluctuations below this starting height do not influence the line profile. As disturbance for the above height interval I used: $v_d = 0.25\ km\,s^{-1}$. With this value the disturbed line profile is calculated for each of the 95 different heights. The bisectors for each profile were calculated and their wavelength shifts give observable velocities, via the Doppler formula:

$$\lambda = \lambda_0 \frac{v}{c}. \tag{3.12}$$

Hence, applying the constant velocity v at levels i with $i \geq j$ we obtain an observable velocity:

$$v_j = vRF_v(\lambda, z_j)\Delta z_j + v \sum_{i=j+1}^{95} RF_v(\lambda z_i)\Delta z_i \tag{3.13}$$

From Eq. 3.13 we can obtain the response function as:

$$RF_v(\lambda, z_j) \approx -\frac{1}{v_d} \frac{v_{j+1}(\lambda, z_{j+1}) - v_j(\lambda, z_j)}{z_{j+1} - z_j} \tag{3.14}$$

where v_d is $0.25\ km\,s^{-1}$. Thirty response functions are calculated for the intensity levels of bisector from $I_\lambda = 0.32$ to $I_\lambda = 0.9$, where the step width is 0.02. Fig. 3.4 gives these functions for the spectral line 543.45nm.

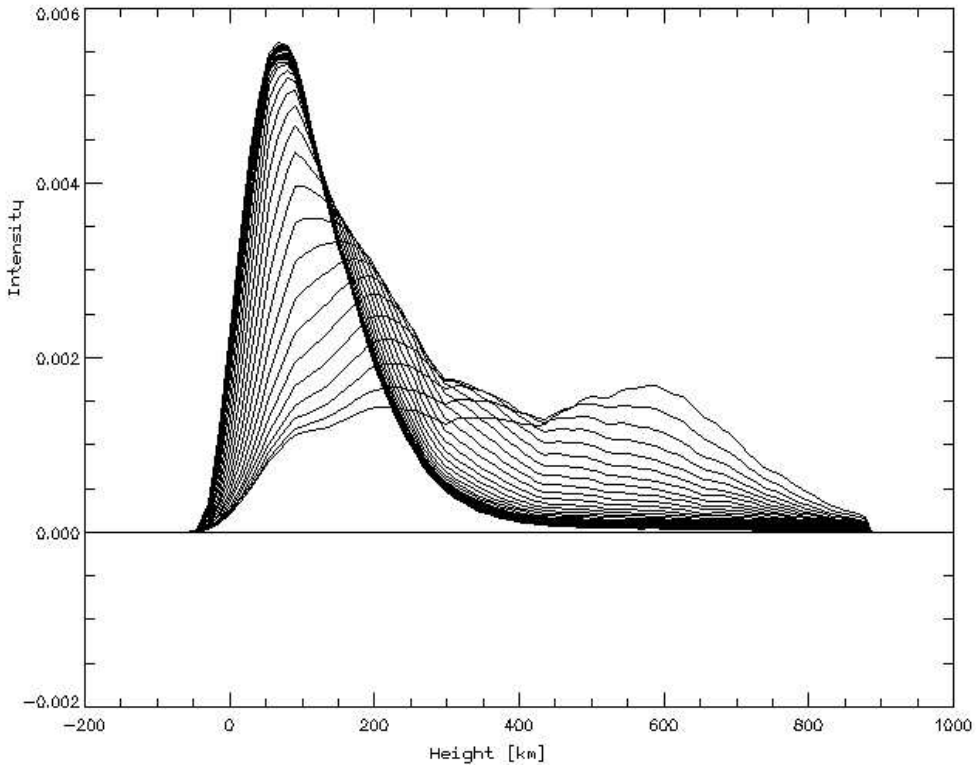

Figure 3.4: Velocity response functions for 30 intensity levels in the profile of the spectral line 543.45nm; that with the peak near 600km stems from the line core, that with the larger peak near 70km from the far line wings (i.e.≈ continuum).

Application

One can notice (in Fig. 3.4) that the velocity response functions cover a rather broad interval of heights. The largest contribution to the fluctuations comes from heights between 400km and 600km.

To achieve as narrow as possible contributions, linear combinations of the velocity response functions were calculated. Fig. 3.6 represents four of the narrowest linear combinations found; these combinations allow achieving satisfactory velocity maps. The linear combinations with maxima at heights below 100km often are too noisy, these had thus to be rejected. That linear combination with the maximum contribution near 500km height was obtained by combining three velocity response functions.

In Fig. 3.7 one can see that the results of the wavelet analysis for the velocity maps at heights between 100 and 200km have similar shapes, while the result for the height 500km shows some power which does not exist at other levels. Since the linear combination for this height was deduced from three velocity response function, there was a suspicion that the extra power obtained at this height might be caused by noise. Therefore, this linear combination was rejected.

In order to check whether the formation height of the spectral line (see Sect. 2.1) has any influence on the final results, data sets with two lines were taken. Since the linear combination for the contribution of the core of the weaker line gives 200km, this height

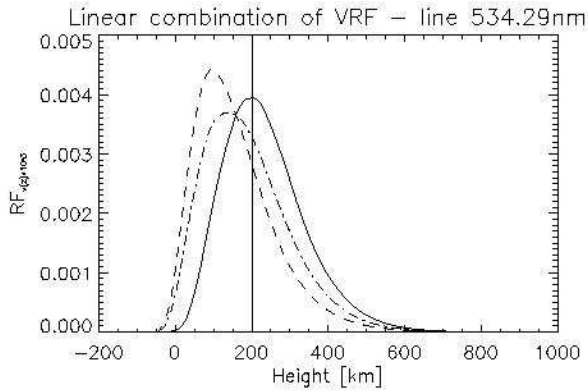

Figure 3.5: The linear combination of velocity response functions for the spectral line 543.29nm at 200km. The dashed and dash-dotted lines represent two velocity response functions for the different intensity levels in the line profile, and the solid line their linear combination.

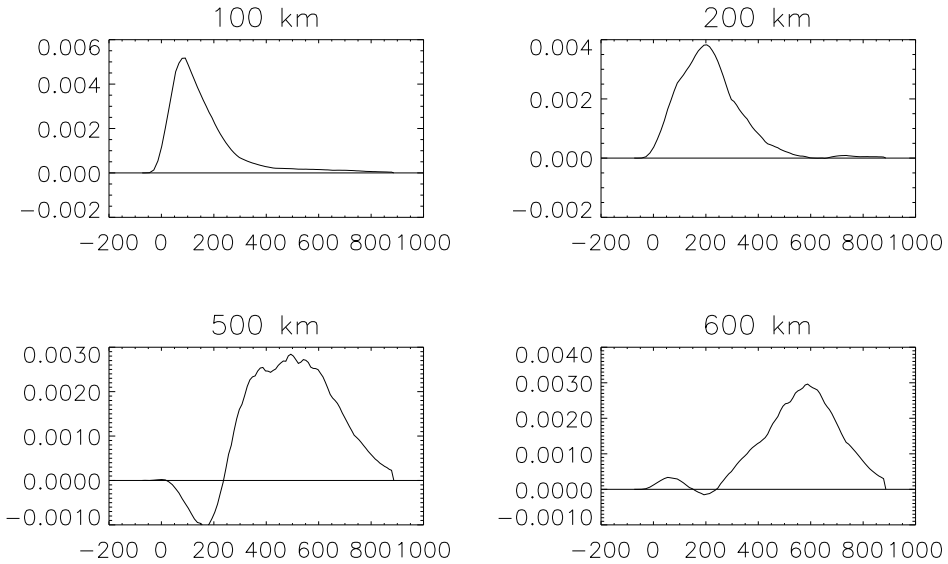

Figure 3.6: Linear combinations of velocity response functions yielding maxima at four different heights.

was taken as suitable for the analysis. Two heights finally chosen for this work are shown in Fig. 3.8.

For data sets with two lines linear combinations were made for each line separately using corresponding response functions. In case of data sets with two spectral lines, the linear combinations are calculated with the expressions:

$$RF_{v(z_{600})} = \frac{RF_0 - 0.6\,RF_4}{0.4} \tag{3.15}$$

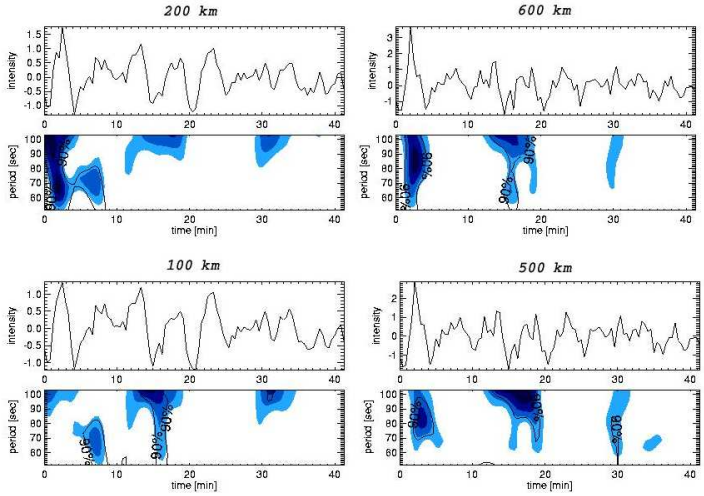

Figure 3.7: Example of results of a wavelet analysis for one pixel in the field of view for linear combinations of velocity response functions yielding maxima at four different heights.

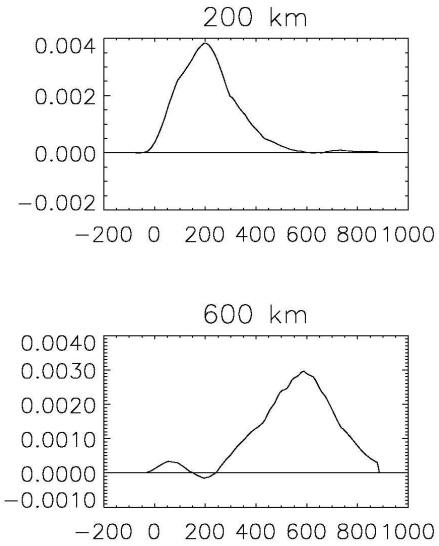

Figure 3.8: Linear combinations of velocity response functions for the spectral line 543.45nm. The top row shows the combination yielding a maximum at 200km and the bottom at 600km.

$$RF_{v(z_{200})} = \frac{RF_1 - 0.6\,RF_5}{0.4} \tag{3.16}$$

where RF_i represents the velocity response function for the level i. For the height of 600km the velocity response functions for the line 543.45nm were used, and for the height of 200km the velocity response functions of the line 543.29nm. In the data sets where only one line was scanned, the linear combinations:

$$RF_{v(z_{600})} = \frac{RF_0 - 0.6RF_4}{0.4} \tag{3.17}$$

$$RF_{v(z_{200})} = \frac{RF_4 - 0.7RF_2}{0.3} \tag{3.18}$$

were used. In Fig. 3.8 the resulting linear combinations of the response function are shown. The linear combination for the height of 200km calculated with velocity response functions for the spectral line 543.29nm, is shown on Fig. 3.5.

3.2.3 Velocity maps

During the scanning with the FPI, for mechanical reasons, the first wavelength position in the line often varies in each scanned line profile. To remove this effect, a calculation of the bisectors is required.

That calculation is done for each pixel in the reconstructed narrowband images. All images from one scan are correlated, so that we have a line profiles for each spatial position. This line profile is then interpolated by a cubic spline function (in the appropriate IDL program), then the bisector positions were calculated. This interpolation is necessary since the spectral line is scanned with a relatively small number of wavelength positions in order to achieve a fast cadence.

As reference for the calculation of the Doppler velocities in our data, we took a mean velocity from one data scan, and set it to zero. The shift of one bisector value with respect to this reference point corresponds to a Doppler shift, since the wavelength distance between two scanning positions is known.

After such calculations are done for each pixel, velocity maps have to be made. These are obtained from the same bisector level as the corresponding velocity response functions from which the linear combinations were calculated to give the narrowest height contribution.

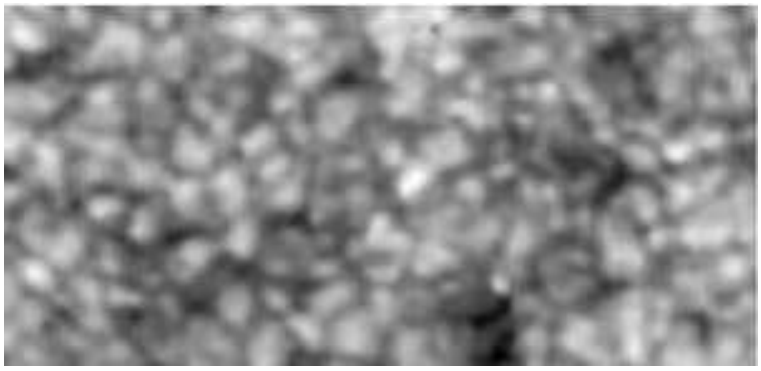

Figure 3.9: Example of a velocity map for the height of 200km; the granulation pattern is visible.

The combinations of different images increase the noise level in the resulting image. To minimize this effect, I calculated only two linear combinations of the velocity response

Figure 3.10: Example of a velocity map for the height of 600km; the granulation pattern is hardly visible.

functions, resulting in the two height levels 200 and 600 km, (see Fig.3.9 and 3.10). Linear combinations for the heights in between those two levels would require the use of three velocity response functions (i.e. three images); while linear combinations for heights below 200km and above 600km would require many individual wavelength images and would be extremely noisy.

3.3 The data cubes

In order to study the time evolution, it is necessary to look at time sequences. This is done by composing the velocity maps into data cubes where the third axis is the time. All these maps have different sizes as a consequence of the reconstruction procedure in the narrowband images. It is therefore necessary to do an additional correlation and destretching. This procedure, outlined below in detail, can be done properly only for images where clear structures are visible. Therefore it is done from the reconstructed broadband images which were already cut to the same dimensions as the narrowband images during the narrowband reconstruction. The parameters obtained in this way were used for correlating and destretching the velocity measurements.

3.3.1 Correlation

In a first step the cross correlation is done with the broadband images using the following equation:

$$Cr(a, b) = A \cdot B^*, \tag{3.19}$$

where a and b are two different functions to be correlated and A and B their Fourier transforms, B^* is complex conjugate. The maximum position of the Cr function is the appropriate shift. To perform a correlation of the images, a central sub-image, is cut and transformed into the Fourier space. The coordinates obtained with this process are saved, and the procedure is then done for the complete time sequence. After obtaining the shift for each image in the time sequence, the images are accordingly displaced and cut to the

same dimensions. This shift is also applied to the velocity maps from which the data cube has to be created.

3.3.2 Destretching

Correlation alone does not finish the procedure. Due to atmospheric influences it can happen that the shapes of certain structures are deformed, even after the reconstruction. This deformation can cause that a pixel in one image of the time sequence does not correspond to the pixel in the next image. Thus, a destretching is required.

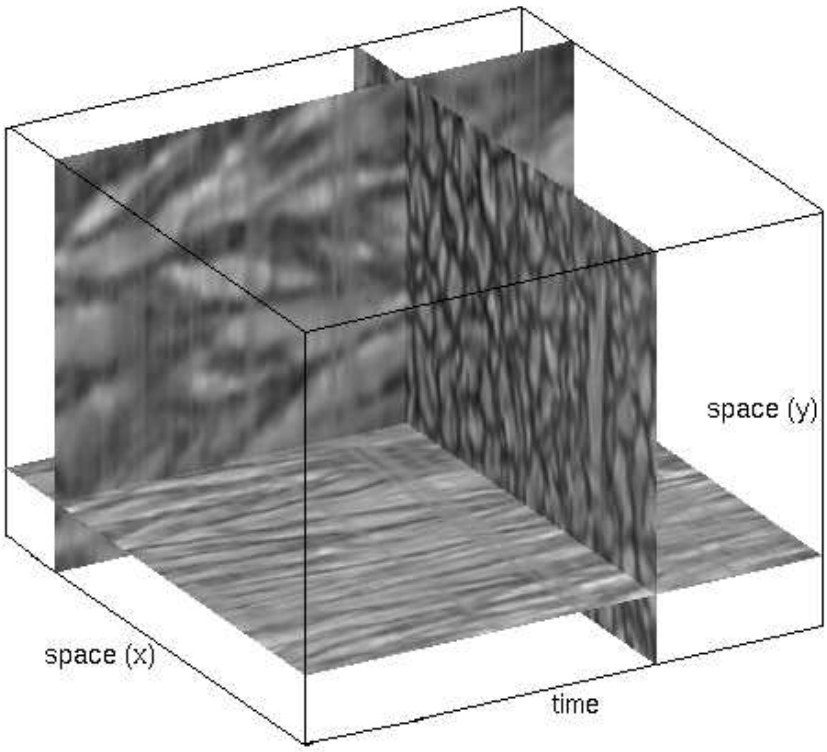

Figure 3.11: Example of a data cube made of granulation images. Three surfaces exhibit cuts through the cube. This cube is used as base in this procedure since it's images have traceable strctures.

To perform this procedure the mean image of the sequence of several images is taken as a reference. This can be done because the granulation changes in a time scale of minutes, while our scans have a time scale of seconds. That reference image is then used for destretching of those images of the chosen sequence. For this procedure the code developed by (Yi & Molowny Horas 1992) is used; it returns the matrix which contains the coordinates and the shift of each pixel. This matrix is then taken to destretch each image of the time sequence, following the method of (November 1986). The matrix calculated with broadband data, is then applied to the corresponding velocity map. These two procedures give the final time sequence.

3.4 Wavelet analysis

For a study of the dynamics of acoustic waves, the information about time and periods is crucial. [1] With wavelets it is possible to obtain simultaneous information about time and frequency. Wavelets may be considered as a compromise between digital data at the sampled times and data through a Fourier analysis in frequency space. In the first case one maximizes the information about the time location, and in the second case one maximises the information about the frequency location.

The essence of a wavelet analysis is the search of structures which are locally similar to one of the wavelets from the set. With the wavelet transform, time series can be analysed, which contain nonstationary power at many different frequencies. The typical wavelet analysis use the continuous wavelet transform:

$$W(s,\tau) = \int f(t)\psi^*_{s,\tau}(t)dt, \tag{3.20}$$

where $f(t)$ is the signal we analyse, $\psi^*_{s,\tau}(t)$ is a set of functions called wavelets, and the variables s and τ are scale and translation factors, respectively. The wavelets are generated from the single basic wavelet, the mother wavelet:

$$\psi_{s,\tau}(t) = \frac{1}{\sqrt{s}}\psi(\frac{t-\tau}{s}), \tag{3.21}$$

where $\frac{1}{\sqrt{s}}$ is the normalisation factor across the different scales.

As is visible from the equations 3.20 and 3.21 the wavelet basis function is not specified. If the function oscillates and is localized in the sense that it decreases rapidly to zero as $|t|$ tends to infinity, it can be taken as mother wavelet. The sets of wavelets created with Eq. 3.21 from the chosen mother wavelet can be orthogonal, bi-orthogonal or non-orthogonal.

The wavelet analysis is a common tool for data analysis. (Vigouroux & Delache 1993, Graps 1995 and Starck et al. 1997) For practical applications so-called discrete waveleta are used.

3.4.1 The mother wavelet

The main problem in the wavelet analysis is to find a set of functions that provides an optimal description of the problem at hand. Various functions which satisfy the conditions for the creation of a wavelet have been found. To choose the wavelet set appropriate for the problem, one needs to know what the main goal of the research is.

For my analysis I choose the Morlet wavelet:

$$\psi_0(t) = \pi^{-\frac{1}{4}} e^{i\omega_0 t} e^{-\frac{t^2}{2}}, \tag{3.22}$$

where ω_0 is the nondimensional frequency and t the nondimensional time parameter. This wavelet is non-orthogonal, based on the Gaussian function and therefore very close to the limit of the signal processing uncertainty, $\sqrt{\pi}$. An example is shown in Fig. 3.12.

[1] For the signal processing, Heisenberg's uncertainty principle states that it is impossible to know the exact frequency and the exact time of occurrence of this frequency in a signal, the limit is $\sqrt{\pi}$.

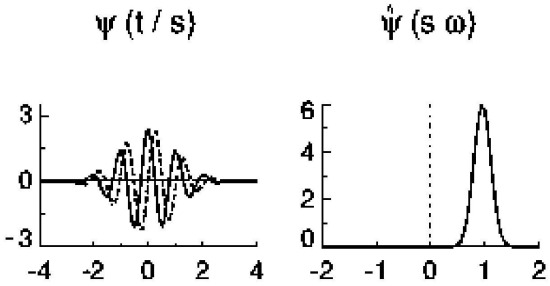

Figure 3.12: Morlet wavelet. The left panel is in the time domain, the solid line gives the real part, the dashed line the imaginary part; at the right panel the wavelet is given in the frequency domain. (Torrence & Compo 1998)

3.4.2 The code

The code for the present wavelet analysis is based on the one developed by Torrence and Compo (Torrence & Compo 1998). This code uses one-dimensional time series for the processing. As result it gives a diffuse two-dimensional time-frequency image.

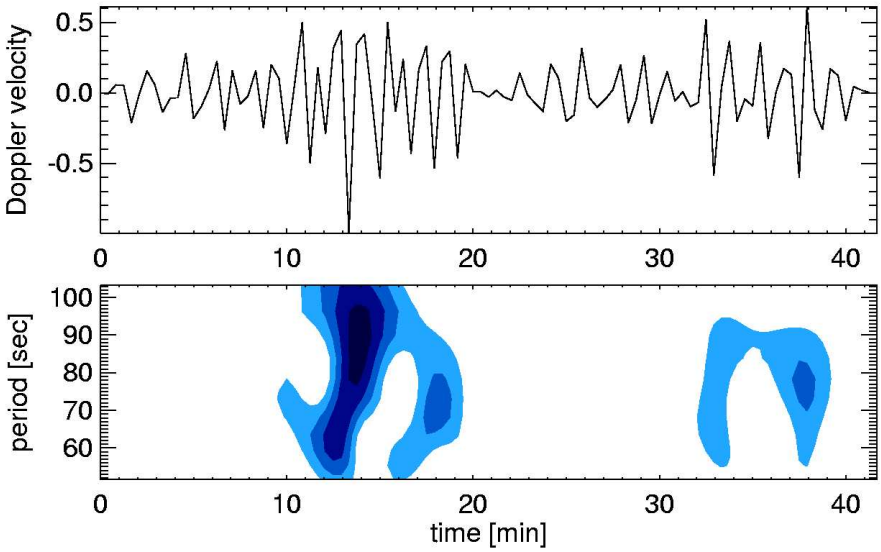

Figure 3.13: Example of a result obtained with the used code. In the top row velocity fluctuations are shown which are subject to the analysis. The bottom row shows the resulting two-dimensional time-frequency image.

Since the wavelet function is complex the wavelet transform is also complex. Therefore the result can be divided into a real part -amplitude- $|W_n(s)|$ and an imaginary part -phase- $\tan^{-1}[\frac{\mathcal{I}(W_n(s))}{\mathcal{R}(Wn(s))}]$. The wavelet power spectrum can be defined as:

$$|W_n(s)|^2. \tag{3.23}$$

For the scales s the following set was used:

$$s_j = s_0 2^{j\Delta j}, \quad j = 0, 1, \ldots, J \tag{3.24}$$

$$J = \Delta j^{-1} \log_2(\frac{N\Delta t}{s_0}) \tag{3.25}$$

where s_0 is the smallest resolvable scale, and J the largest scale. The best choice for s_0 is the value whose equivalent Fourier period is approximately Δt. The choice of Δj depends on the width of the wavelet function in the spectral space. Smaller values give higher resolution.

The code by (Torrence & Compo 1998) is made for noncyclic data in the Fourier space. To avoid errors at the edges of the data set, apodisation of the data was done before they are submitted to the wavelet analysis. Since all time series are subject to noise, only peaks in the wavelet power spectrum which are significantly above the noise level can be assumed to be a true feature with sufficient confidence. Therefore the total amount of presented wavelet power depends on the noise level; if that is low, more realistic wavelet power will occur, and vice versa.

For this work only a wavelet power spectra were used. The final result from the applied code is a four-dimensional data cube, where the additional fourth dimension is the wavelet power variation with the period. The wavelet transform can be considered as a bandpass filter of uniform shape and varying location and width (Torrence & Compo 1998, Wunnenberg et al. 2003). During the data reconstruction a certain amount of the noise remains in data. Wavelet analysis tends to filter out those remains, since it is registering only the selected frequencies in time which are significantly above the noise level. Therefore, noise then has no large effect on the processed data. This is readily seen during the choice of the appropriate linear combinations for a description of the height contribution.

3.4.3 Additional data processing

The resulting four-dimensional data cube spanning the whole period range was divided into period intervals named octaves. For the period range of 50s to 100s the data cube resulting from the used code, had eleven octaves, see Fig. 3.14.

For an overall analysis integration over all octaves is done. This gives the power integrated over the complete period range, see Fig. 3.15. In addition, integration is also done taking only two or three neighbouring octaves. This gives the integrated power over five sub ranges of the total period range.

Comparison of the two-dimensional power features requires constructing a particular spatial filter which removes all power features below a level which is given by the noise.

For the calculations of the energy carried by waves, additional high pass filtering of the velocity maps on the fluctuation range of 50 to 120s is done.

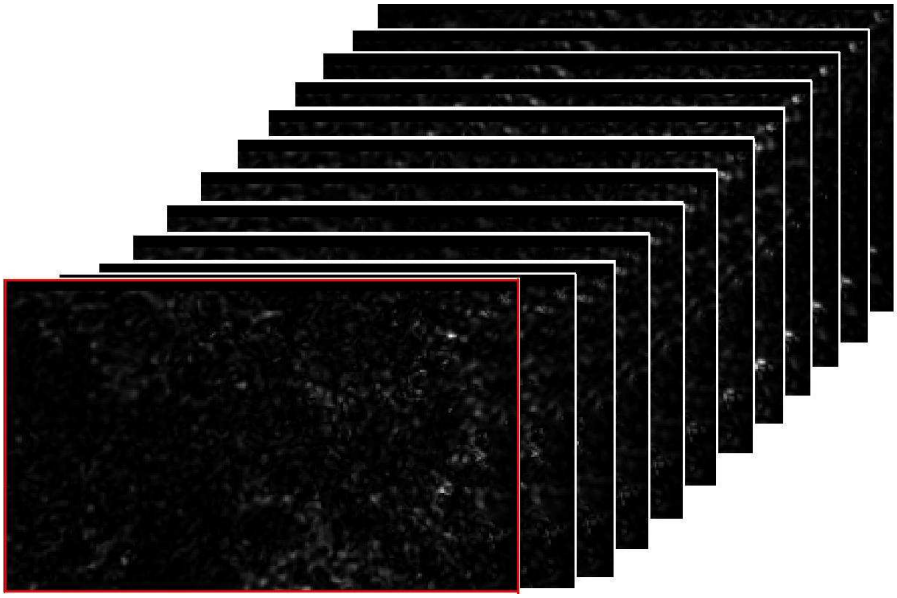

Figure 3.14: Example of a set of octaves of the data cube; each surface displays the two-dimensional distribution of power in one octave.

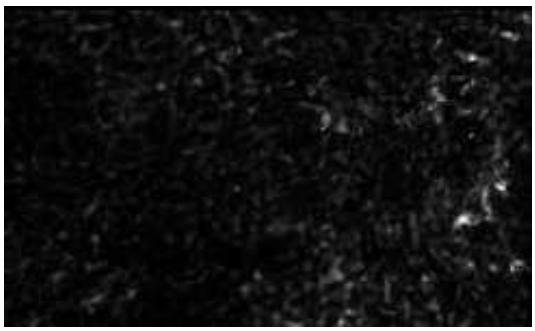

Figure 3.15: Example of integration over all sets of octaves of the data cube.

4 Results

It is believed that spatially unresolved motions, or non-thermal micro-turbulence, have as physical processe short-period waves,which may be responsible for the energy transport to the chromosphere (Ulmschneider & Kalkofen 2003). The existence of chromospheres and coronae depends on a constant energy supply provided by mechanical heating (Ulmschneider & Kalkofen 2003). The heating required to balance the radiative loss is approximately $4 \cdot 10^3 \frac{W}{m^2}$. The behaviour of short-period waves and the amount of energy they carry are the subject of this work.

4.1 Waves at different heights

Short-period waves with periods from 10s to 150s are assumed to be the main carrier of the energy required for the heating. The peak energy should be transported by waves of periods below 50s. An observation of these waves encounters technical difficulties, since it requires good spatial and temporal resolution; they were thus first investigated in the last few years (Hansteen et al. 2000, Wunnenberg et al. 2003). A first step in this work was to determine whether velocity fluctuations observed by (Wunnenberg et al. 2003) exist at different heights. Fig. 4.1 represents my result of the wavelet analysis of fluctuations at the same height (i.e.,600km) as the one used in (Wunnenberg et al. 2003).

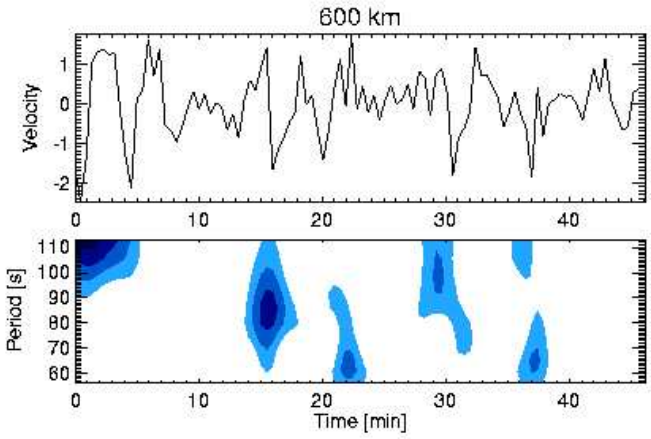

Figure 4.1: Wavelet power section from data set DS2, calculated for the pixel $x = 60, y = 75$ in the image plane. The maximum of the heights which contribute to the observed fluctuations is at $\approx$ 600km.

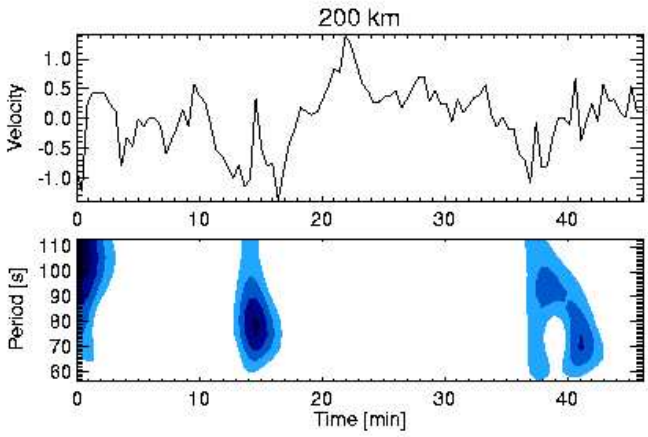

Figure 4.2: Same as Fig 4.1 but for $\approx$ 200km height.

At the top row of the figures the velocity fluctuations are shown, and at the bottom row the power of the short-period waves, both as function of time. Darker colour means that large power is registered, light colour means that less power is registered. There are 6 areas in the bottom row of Fig. 4.1 which represent the finally obtained power.

Fig. 4.2 shows the result of the wavelet analysis at the height of $\approx$ 200km. Here, only three areas show power.

Table 4.1: Overview of the power occurrence at the height 200km.

Occurrence of power in time			
time[min]	periods[s]	time for maximum power[min]	periods for max. [s]
0-5	65-110	0-1.5	100-110
13-17	60-110	14-15.5	69-89
37-43	56-110	41	68-73

In Table 4.1 one can see an overview of the power appearing in Fig. 4.2; Table 4.2 gives an overview of the power from Fig. 4.1. It is noticeable that although both images represent the same pixel in the data set, the results of the power are not the same. At the higher level one can notice more power features distributed in time and apparently without connection to the lower level. On the other hand power at the lower level, 200km, might be related to some of the features at the higher level, although the distribution of power is slightly different in time and period.

Short-period waves are not often visible in the signal presented in the top row of the figures, since longer-periods are overwhelming. In figures 4.3 and 4.4 however, a signal is present.

The different data sets show that power of short-period oscillations (in the range of 46s to 120s) appear at different heights in the solar chromosphere. It is evident that the power varies in time and appears with varying amplitudes. In addition, at 200km the power peaks appear to be less frequent than at 600km.

Table 4.2: Overview of the power occurrence at the height 600km.

Occurrence of power in time			
time[min]	periods[s]	time for maximum power [min]	periods for max. [s]
0-5	90-110	0-2	100-110
14-18	60-110	15-16	77-90
20.5-23.5	56-91	21.5-22.5	54-69
28-32	69-110	29-30	90-107
35-37	100-110	-	-
36-38	56-85	36.5-37.5	60-68

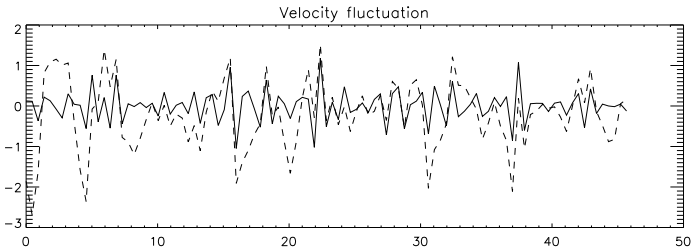

Figure 4.3: The Doppler velocity fluctuations from data set DS2, at the pixel $x = 60, y = 75$ in the image for the height of 600km. The solid line represents filtered velocity fluctuations in the period range $55 - 120$s, the dashed line represents non-filtered signals from the top row of Fig. 4.1.

4.1.1 Spatial location

In Fig. 4.5 the power of short-period waves is shown as two-dimensional maps. It is evident that power at the height 200km appears seldom in space as compared to power at the height 600km, in agreement with the findings in figures 4.1 and 4.2. In the enlarged rectangles one notices features which at 200km have low power and occur in three different patches; at 600 km these features are stronger in power and of different shape. The power features at the height 200km which appear at the same location as the power features at the height 600km tend to span less space. The shape of the power features tends to vary with height. A possible explanation for this spatial variation is a characteristic of short-period oscillations: they tend to expand in space while travelling upward. The contribution to the spatial variation comes from the dissipation of waves of different periods at different heights. The merging of waves from different sources additionally complicates this picture.

An example of merging is shown in Fig. 4.6. In the top row it is seen that the power features of the waves emitted from two neighbouring intergranular lanes merge into one feature at 600km. This feature is marked with a green arrow at the beginning of its evolution. The process is easier to see for waves with longer-periods since they change more slowly in time (see section 4.5.1).

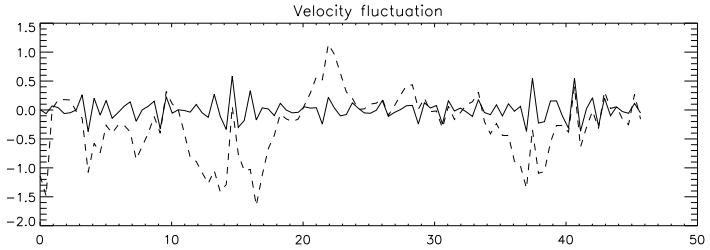

Figure 4.4: The Doppler velocity fluctuations from data set DS2, at the pixel $x = 60, y = 75$ in the image plane for the height of 200km. The solid line represents filtered velocity fluctuations in the period range $55 - 120$s. The dashed line represents non-filtered signals from the top row of Fig. 4.2.

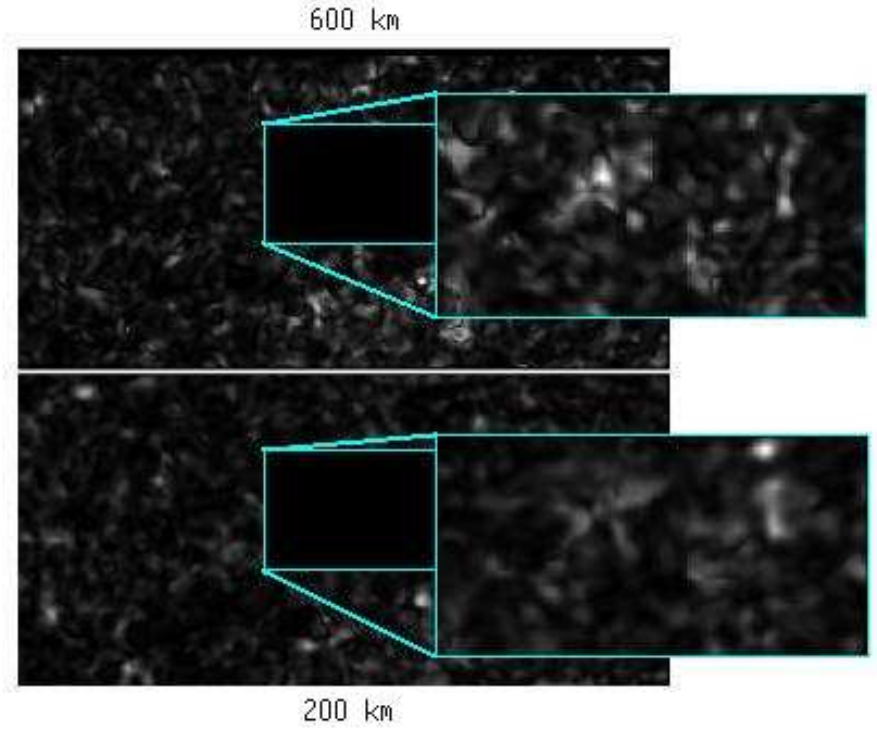

Figure 4.5: Two-dimensional map of the short-period wave power form the data set DS1, integrated over period ranges 50s to 100s. The images are time-shifted by 50s which corresponds to the time necessary for short-period waves to travel with sound speed from the 200km to the 600km height level.

4.2 Methods used for the analysis of the data

To obtain the final results it was necessary to perform an additional analysis. In this section the respective methods are described.

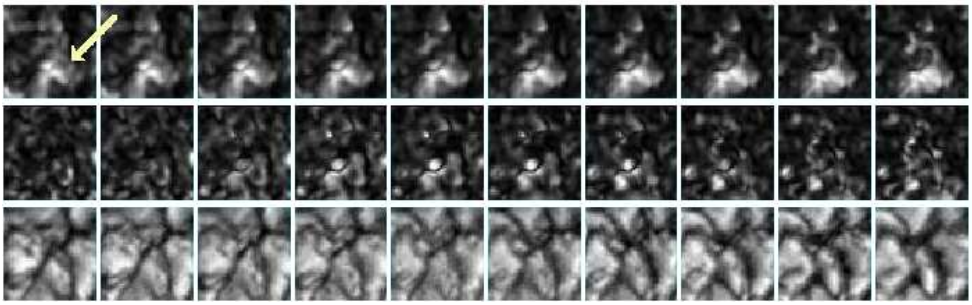

Figure 4.6: Time sequence of 250s from the data set DS1, with repetition rate of 25s. The bottom rows represent the granulation, the middle row the integrated power of short-period waves with periods of 50s to 100s at the height 600km, and the top row the integrated power of short-period waves with periods of 50s to 220s at the height 600km. The arrow points to a merging power feature.

4.2.1 Comparison of the spatial distribution of short-period waves with white-light structures

The starting assumption is that the observed short-period waves are acoustic in nature and thus travel through the solar atmosphere with $v_{sound} \approx 7\frac{km}{s}$. Therefore, as a first attempt, a time-shift required for connection between waves and granular events is applied to the data as expected from this velocity. In many cases where this shift proved to be inappropriate other time shifts are applied.

Pixel by pixel comparison

This comparison is made by simple comparison of the intensity of the corresponding white-light image with the short-period waves power map. In Fig. 4.7 a scatter plot for one moment in the time sequence is shown.

To obtain the percentage of power which is located above dark structures, the power was normalised, and only that power which exceeds 0.3 of the maximum value is considered. For comparison with the corresponding white-light image, it was assumed that the short-period waves travel with the speed of light and the appropriate time shift was calculated accordingly. This procedure is done through the whole time sequence yielding the variation of the percentage with time. During the time sequence the percentage of power appearing above intergranular lanes varies, as is visible in Fig. 4.8.

Comparison of power maps with the white-light images

Since the pixel by pixel comparison is insufficient for an accurate determination of the location of short-period waves, additional methods needed to be used.

In the first and third rows of Fig. 4.9 one can notice various structures formed by power of the short-period waves. I will refer later to such patches as 'power features'. In the second and fourth rows the granular evolution is shown; over-plotted are coloured contours which present areas with observed power of short-period waves.

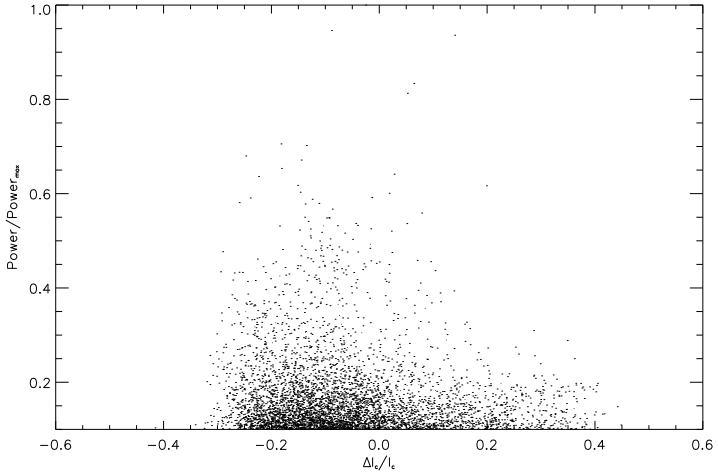

Figure 4.7: Scatter plot from the data set DS1. The short-period waves power above 30% of the maximum level is presented vs. the corresponding pixel intensity in the granulation image considering a time shift expected for the acoustic wave propagation of 25s between the continuum level and the height of the 200km.

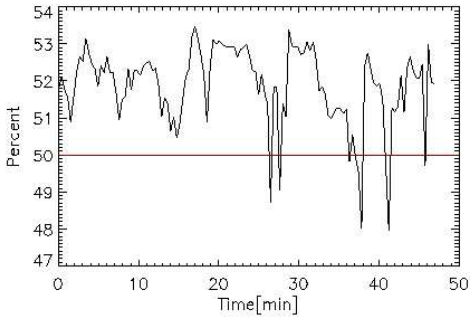

Figure 4.8: Time variation of the percentage of short-period waves power appearing above intergranular lanes for the data set DS6a.

This spatial comparison makes it possible to visually determine the exact location of a power feature in the white-light image. A similar method of analysis was presented in the work of (Espagnet et al. 1996).

For such a spatial comparison the full area of the reconstructed white-light images were cut into squares of 50×50 pixels. Since the reconstructed white-light images have the same field of view as the power maps it was easy to obtain for both equally sized squares.

The squares obtained in this way could cover shorter time spans which are more comfortable for a visual inspection. Here, it is important to make a presentation of the data easy to handle. The white-light images represent the continuum level; therefore I put them on the bottom row of the respective figures, the middle row presents power of short-period waves at the 200km level and the top row the level of 600km. The amounts of power are

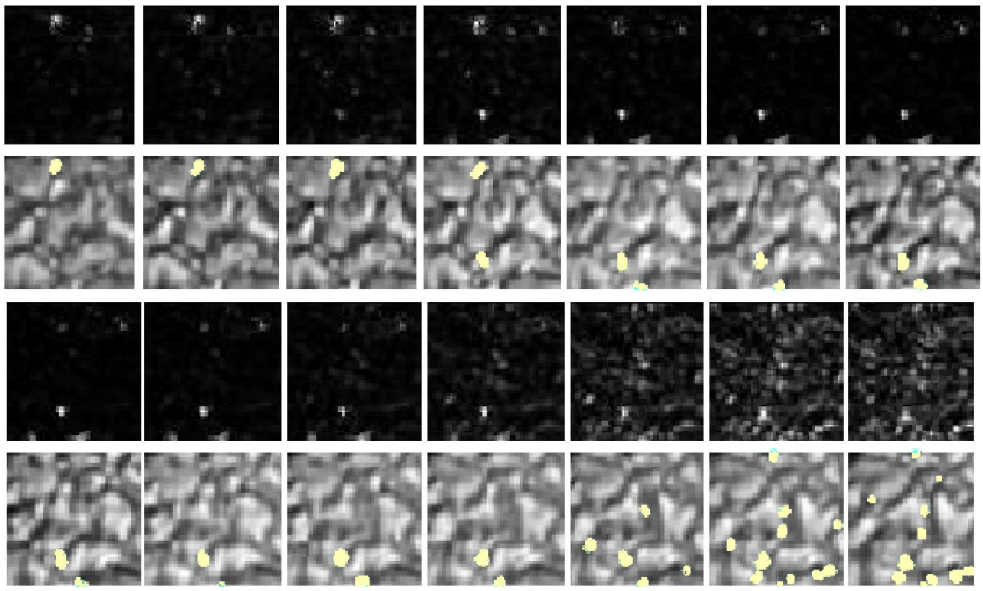

Figure 4.9: Time sequence of 311.3s from the data set DS5, with a repetition time of 28.3s. The second and fourth rows show granulation changes with the yellow areas marking positions of the most intense power, and the first and third row exhibit power of short-period waves integrated over the same period range at the height 600km.

different at both height levels, therefore the power is normalised before presented in the maps. All maps are 'tv-scaled' [1]; the normalised maximum corresponds to white and the minimum, in this case 0, to black. An example is given in Fig. 4.10. The arrows mark features whose behaviour is explained in Sect. 4.4.1.

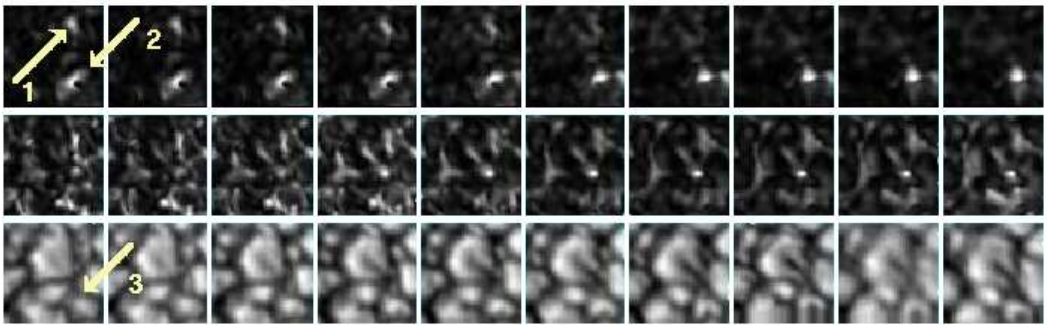

Figure 4.10: Time sequence of 274s from the data set DS2, with a repetition time of 27.4s. The top row shows power of short-period waves integrated over the same period range at the height 600km. The bottom rows represent granulation changes, the middle row power of short-period waves integrated over periods 55s to 110s at the height 200km

The other two power maps were placed above the white-light images, first the ones from 200km and then the ones for 600km. The procedure was repeated for 10 sub-images

[1] A routine from the IDL which presents matrices scaled in the most appropriate way.

of the time sequence. The sub-images of the power maps were also time-shifted following the method described in Sect. 4.2.2. This order was chosen because it is similar to natural positions.

This procedure was followed for the whole time sequence of each data set. To obtain the percentage of specific events or locations, simple visual sorting and counting of the events or locations was done. The percentage was then calculated with respect to the total number of all recorded events.

4.2.2 Determining the time shift

As a first step in this analysis a pixel by pixel correlation was attempted. This analysis is done under the assumption that short-period waves should travel with the speed of sound through the solar atmosphere; hence the higher level was shifted back in time by an appropriate interval. The power was normalised. Since features vary in intensity, a binary mask was formed covering the areas where the short-period wave's power exceeded a given minimum. This procedure gives the exact positions of features with power above 30% of the maximum power. These binary masks were then compared pixel by pixel for both height levels.

Time shifting by visual comparison

The time shift in this work is done in two ways. First a comparison of the power features with the granular evolution is done. In Fig. 4.11 an example of time shift using the power feature is shown. In this method I selected a power feature with a similar shape at both levels. The power features chosen in that way I first related with the white-light images, determining the granulation event which might be responsible for the emission of the short-period waves.

After that the time shift is done in such a way that the time evolution of the corresponding granulation change follows the time evolution of the power feature. This method to determine the time shift opened the possibility to pay attention to waves which travel down. [2]

In many cases a power feature could not be found in those power maps obtained by integrating the power over the whole range of short-period waves, from 46s to 120s. In this case the time shift was determined from power features of one of the period intervals shown in Table 4.3. Some of the events gave different time shifts for different period ranges. In these cases, the events in each period range were treated and counted as separate events.

Time shifting by maximum power

Since the whole procedure described above is done visually, an additional test of the results was necessary. This time shift is done by comparison of the power variation of similar power features in both height levels. First, the visual method is used to locate the power feature at one level, and then the field of view is reduced such that it contains only the power feature with its closest neighbourhood. Then, using the same coordinates, the

[2] Only two such events are found, which make the relative occurrence less than 1%.

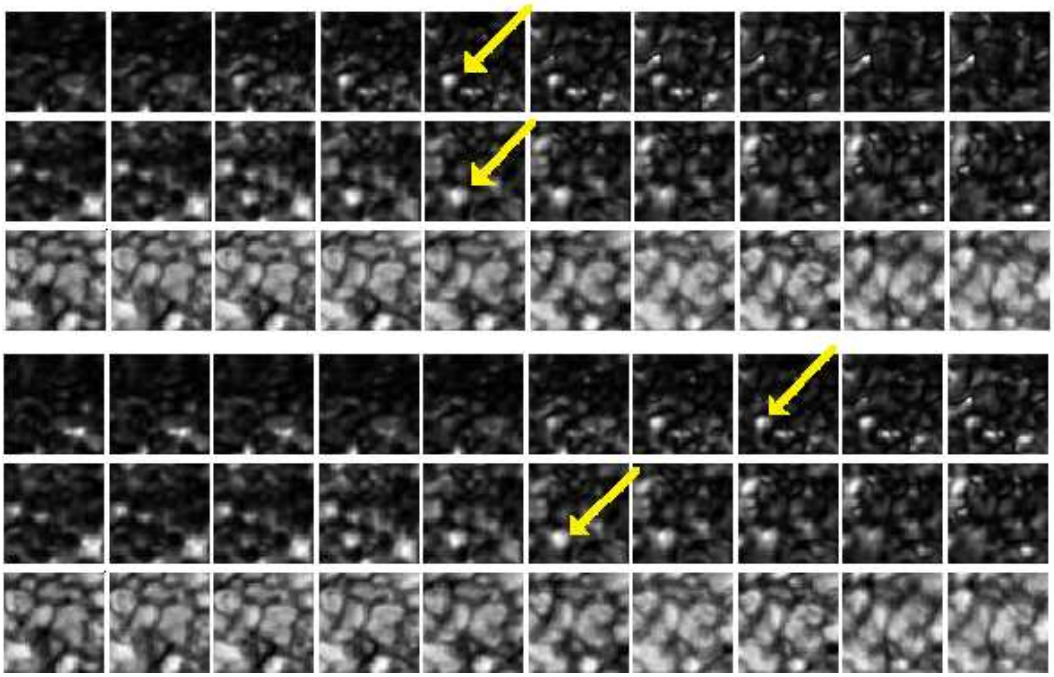

Figure 4.11: Example of a time shift. In the bottom row the time evolution without time shift is shown, and in the top row with a time shift appropriate to mach the maxima at 200km (middle) and 600km (upper rows). The yellow arrows point at the power feature which was used for the time shift.

field of view is reduced for the other level. Finally, the evolution of power integrated over a particular feature in the power maps is plotted versus time for both height levels. This yield the desired shift from an optimum match of both.

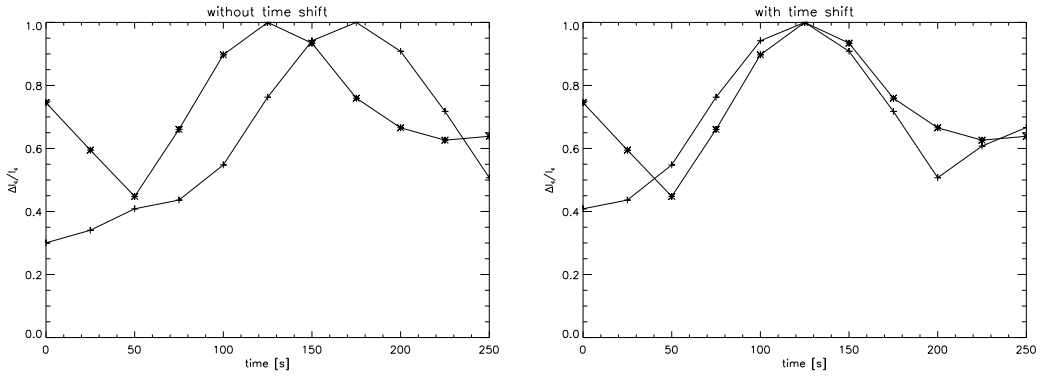

Figure 4.12: Temporal variation of the power spatially integrated over one power feature in the data set DS1. The line with crosses presents the feature at 600km, the line with stars the feature at 200km height. The diagram is done for an example from the data set DS1. A time shift is not applied in the left panel, in the right panel a time shift corresponds to 50s.

4.2.3 Different periods

The analysis showed that the use of power integrated over the whole period range does not allow obtaining a clear picture of the short-period waves. Much interesting information can be lost with an integration of the power over the whole period range of a given data set. Therefore, an analysis of the different period intervals was performed. This is possible since the wavelet analysis gives so called octaves per total period range. An investigation of separate octaves, i.e. period intervals, gives the information required.

It is found that differences between neighbouring octaves are not too large, since the observed power behaviour varies slowly with the period. Hence, for better presentation of the results a summation of power over two adjacent octaves is done. This integration gives the period intervals presented in the Table 4.3. In this table also the abbreviations for the various period ranges are introduced.

Table 4.3: Period intervals obtained from integration over octaves.

Period intervals for all data sets		
Data set	abbreviation for interval	period ranges [s]
DS1	P11	50-60
DS1	P12	60-70
DS1	P13	70-80
DS1	P14	80-90
DS1	P15	90-100
DS2	P21	54-65
DS2	P22	65-76
DS2	P23	76-87
DS2	P24	87-98
DS2	P25	98-109
DS3, DS4, DS5	P31	56-68
DS3, DS4, DS5	P32	68-79
DS3, DS4, DS5	P33	79-90
DS3, DS4, DS5	P34	90-102
DS3, DS4, DS5	P35	102-113
DS6	P61	45-54
DS6	P62	54-63
DS6	P63	63-72
DS6	P64	72-81
DS6	P65	81-90
DS7	P71	59-71
DS7	P72	71-83
DS7	P73	83-95
DS7	P74	95-107
DS7	P75	107-119

The power maps obtained in this way were then exposed to the same visual detection which was performed to the maps of the integrated power over the whole period range for the respective data set.

Waves of longer-periods

With the wavelet analysis, an increase of the number of octaves increases the observed period range, for data set DS1, from 50 to 200s, and for the data set DS6a, from 48 to 300s. For the present analysis of the long period-waves the power was integrated over the whole period range of data set DS1 and over the interval 175s to 300s for DS6a. The analysis of the power maps obtained in this way was also done using the visual method.

Finally, the whole power was summed over the periods, for each data cube.

4.2.4 Terms used for description of granular events

In this section certain terms will be defined which describe events observed in the granulation; they are sorted alphabetically.

Appearance of a granule

If in a larger intergranular area a new granule starts to appear and to grow, the event will be called 'appearance of a granule'.

Bright point-like structure

A small structure which appears in intergranular lanes possesses usually shapes which are much smaller than the surrounding granules. Some of these structures have a high intensity, but some of them are less bright than the surrounding granules. The G-band bright points are very similar in shape and location as the structures observed here, therefore I call them 'bright point-like structures'.

Changes of abnormal granulation

If the typical granulation pattern is hardly visible since smaller structures fill the intergranular lanes, the event is called abnormal granulation. Changes in this kind of granulation in shape and position are much faster and easier to notice.

Disappearance of a low intensity structure within a granule

A darker structure in the centre of a granule can mean two things: that granule will explode or that simply a large granule has bright edges. In the second case, it can happen that during the change of a granule's shape the darker area in its centre disappears.

Disappearance of a part of a granule

Sometimes a granule starts to change the shape, and parts of the granule seem to fade to the background.

Fading of a small granule into the background

If a granule disappears by slowly shrinking and loosing intensity one can say it fades into the background.

Merging of two granules into one larger

One of the possibilities of the ending of granules, especially smaller ones, is that two or more of them merge into one larger.

Slow granulation changes

If changes in the granulation occur of the order of minutes, without any special events, I address this as 'slow granulation changes'.

Splitting of a granule or exploding granule

Often large granules can split into two or more smaller ones. If this happens quickly, the event is called 'exploding granule'.

4.3 Location of short-period waves

One of the interesting points of short-period wave analysis is to determine where exactly in the chromosphere they appear. The analysis with visual methods was described in Sect. 4.2.1. The results in this section were obtained by a comparison of the spatial distribution of the short-period waves with the white-light structures.

As stated in section 2.3 the data sets used in this work were taken from different regions of the solar surface. Therefore, the following results are grouped according to the different objects of observation.

4.3.1 The quiet Sun

The data sets DS1, DS2, DS3 and DS6a were observed in the quiet Sun. The first step in the analysis was the pixel by pixel comparison. This kind of analysis showed that for these data sets the most common location of short-period power are the dark intergranular areas. In figures 4.7 and 4.13 scatter plots for one moment in the time sequence is shown. It can be seen that the power at 200km is more concentrated in the intergranular lanes [3] than the power at 600km. Here, the power above intergranular lanes is about 70% of the total power at the height of 200km, and about 60% at the height of 600km.

The situation is a bit different for the other data sets, for DS6a the percentage of the power above the dark intergranular areas is 52% at the 200km. The scatter plot for this set of data is given in Fig. 4.14.

[3] Defined as $\Delta I_c < 0$, where ΔI_c is the local continuum intensity minus that of the mean undisturbed Sun.

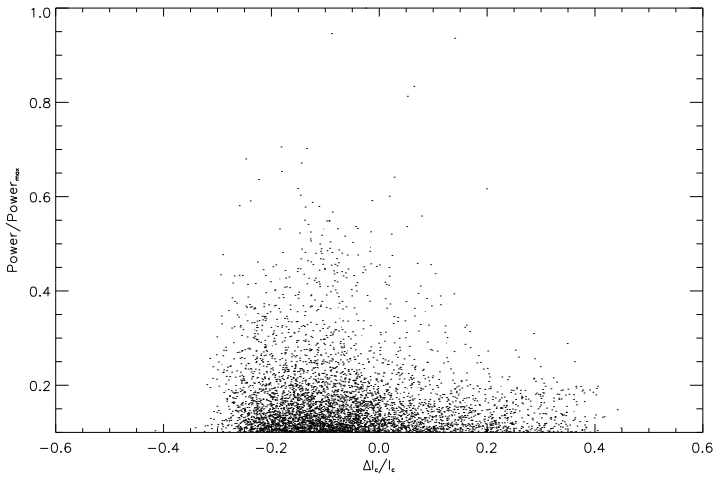

Figure 4.13: Scatter plot from the data set DS1. The short-period wave power exceeding 30% of the maximum level is presented vs. the corresponding pixel intensity in the granulation image after a time shift expected for acoustic wave propagation of 75s between the continuum level and the height of 600km.

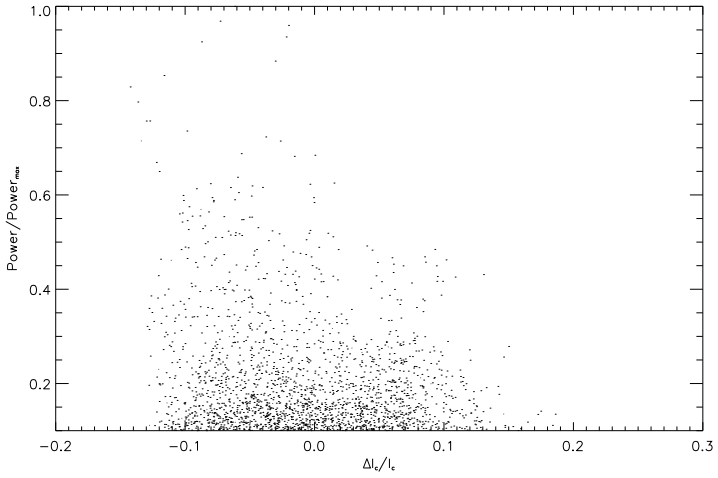

Figure 4.14: Scatter plot from the data set DS6a. The short-period waves power is presented vs. the corresponding pixel intensity in the granulation image with the time shift expected for the acoustic wave propagation of 68s between the continuum level and the height of the 600km.

The scatter plots were made for just one image from the time sequence. During the time sequence the percentage of power appearing above intergranular lanes varies, as is seen from Fig. 4.8.

The maximum of the power

Various events cause power of different amount. An overview of the events related to a maximum of power is given in Table 4.4.

Table 4.4: Granular events which cause a maximum power of short-period waves in the data set DS1.

Data set 1 - cause of the maximum of wave power		
No.	granular event	%
1	bright point-like structure	42
2	disappearance of bright structure	15
3	dark intergranular lane with traces of some structure	15
4	dark intergranular lane	14
5	dark patch in a granule	7
5	appearance of a granule	7

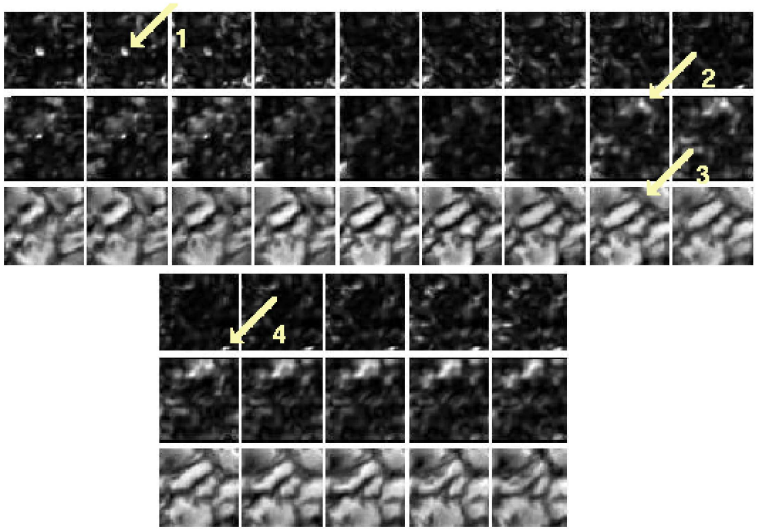

Figure 4.15: Time sequence of 350s from the data set DS1, with a repetition time of 25s. The bottom rows represent granulation changes, the middle row power of short-period waves integrated over periods 50s to 100s at the height 200km, and the top row power of short-period waves integrated over the same period range at the height 600km.

Fig. 4.15 shows several examples of the maximum power of short-period waves and their location within the quiet Sun structure. There are three clearly distinguished power features of strong intensity in this time sequence. The maximum marked with 1 which appears at both height levels in the first three images, i.e. the first 75s, is located in the centre of an intergranular lane.

The other power feature, marked with 2, which appears in the last 7 images, i.e. 175s, at the height of 200km is composed of two maxima which seem to merge into one power

feature. In the first 3 of those images, the maximum is easy to separate from the rest of the power feature since it has high intensity and appears in an intergranular lane above some small structure near the edge of a larger granule, marked with the 3. The second maximum which can be distinguished, starts gaining intensity 25s after the first one and appears also in the intergranular lane just at the bottom edge of a small structure near the border of a larger granule.

Another maximum, marked with 4, which appears in the seventh image of the sequence, i.e. after 175s, is located at the edge of the sub panels, a relation with the granular events can thus not be deduced.

The lower values of the percentage obtained with the pixel by pixel analysis for the data set DS6a, can be explained by the finding that power above bright structures is more frequent for DS6a than in the data set DS1: for DS6a 67% of the short-period wave power maxima appear above bright structures.

4.3.2 Solar area with G-band structures

In order to study possible differences between quiet and active regions, data sets which contain G-band structures have been observed. At the beginning of each observation the solar area with G-band structures was selected with the help of a G-band filter. Exact locations of the G-band structures are not registered. These sets are DS4 and DS7. The pixel by pixel comparison of the granular intensity with the location of short-period power gives 52% of the power above dark intergranular lanes for the height level of 600km, and 53% for the level of 200km. Fig. 4.16 presents the scatter plot for the data set DS7. It can be seen that the power is almost equally distributed over granules and intergranular lanes.

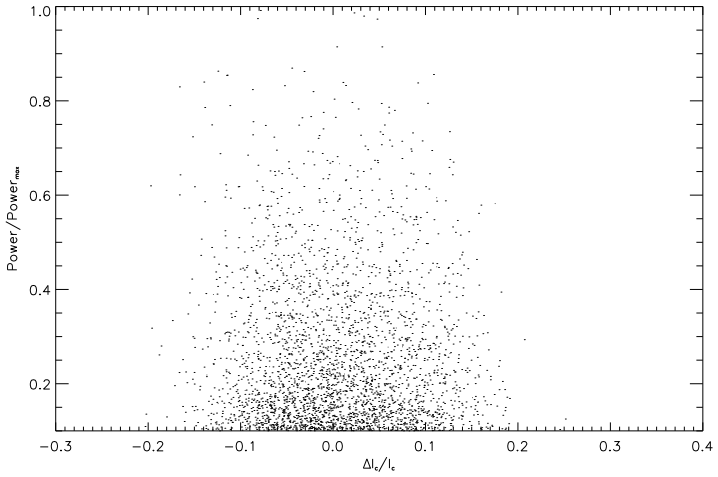

Figure 4.16: Scatter plot from the data set DS7. The short-period wave power is presented vs. the corresponding pixel intensity in the granulation image with the time shift expected for the acoustic wave propagation of 90s between the continuum level and the height of the 600km.

In the Fig. 4.17 the variation of the percentage is shown for the whole time sequence. It is noticeable that for this data set, the percentage varies much less than for the quiet

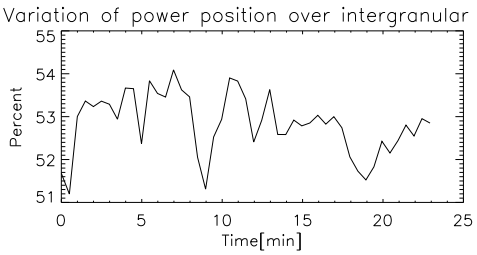

Figure 4.17: Time variation of the percentage of short-period waves power appearing above intergranular lanes for the data set DS7.

Sun, and tends to be above 50% over the whole time. This could be due to the larger occurrence of small structures in the solar regions with G-band features.

Location of power maxima

The maxima of the observed power are mostly located above bright structures, but not in an amount one would expect. In Table 4.5 an overview over the most common locations of the maxima of short-period waves is given.

Table 4.5: Events which cause the maximum power of short-period waves in data set DS7.

Data set 7 - location of the maximum of wave power		
No.	granular event	%
1	the bright point-like structure	39
2	intergranular lane	23
3	the dark intergranular lane with traces of some structure	19
4	the dark patch in the granule	19

4.3.3 Observations containing a pore

A still stronger influence of magnetic fields on short-period waves than in G-band structures can be expected in the vicinity of pores. The observations near a pore are DS5 and DS6b. The pixel by pixel analysis shows that the amount of power above the intergranular lanes is for both sets of data 49% at the height of 200km; at the upper level of 600km, it is 49% for the data set DS6b and 50% for DS5.

The scatter plot in Fig. 4.18 shows a group of points at the left side which is separated from the main group. This power is probably appearing above the pore, since they are related to very low intensities.

During the time sequence, the percentage of power above intergranular lanes does not vary strongly, except at the end; its mean value is about 49% (see Fig. 4.19).

An interesting result is the almost equal percentage of power above intergranular lanes at the two height levels for both data sets which contain magnetically active structures. A

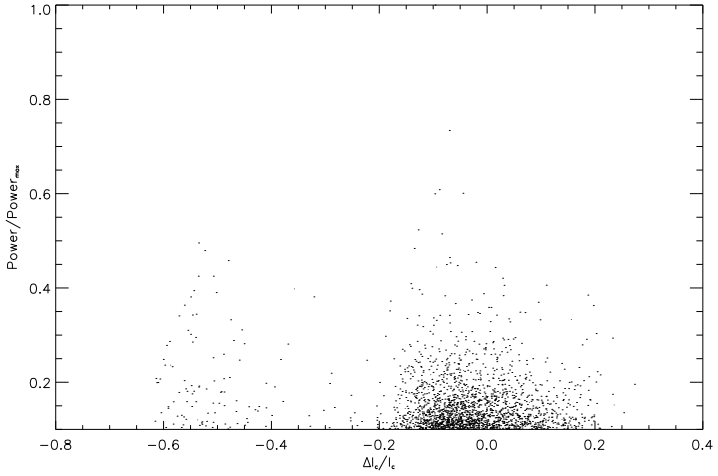

Figure 4.18: Scatter plot from the data set DS6b. The short-period waves power is presented vs. the corresponding pixel intensity in the granulation image with the time shift expected for the acoustic wave propagation of 68s between the continuum level and the height of the 600km.

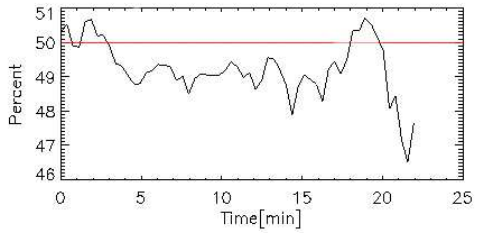

Figure 4.19: Time variation of the percentage of short-period wave power appearing above intergranular lanes for the data set DS6b.

possible explanation for this may be that power features above bright point-like structures do not differ spatially between different heights. They tend to be similar, with sometimes very slight symmetric expansion at the higher level.

Location of the power maxima

The study of short-period wave sources in these data is done from sub-images not containing the pore. The pore and its vicinity showed quite small amounts of power; therefore this analysis is done outside the pore. Since the data sets with the pore also contain G-band structures, it was enough to exclude the pore and its close neighbourhood to get a data set with G-band structures. As might be expected, the analysis of sub-images without pore showed that most of the power maxima appear above bright structures. An overview of the results for the DS5 set of data is shown in Table 4.6. Inside the pore there is no significant power of short-period waves, most power appears in the ambient area. In the

pore there is one maximum which appears to be connected in high layers with structures which are bright and located on the border of the pore, see Fig. 4.21.

Table 4.6: Events which cause a maximum power of short-period waves, for the data set DS5.

Data set 5; location of maximum of wave power		
No.	Event	%
1	bright point-like structures	52
2	intergranular lanes	36
3	dark intergranular lanes with traces of some structure	6
4	dark patch in a granule	6

4.4 Relation of short-period waves to certain structures on the Sun

The data used in this work make it possible to investigate the position of power features relative to white-light events. The relation of short-period waves and white-light structures gives valuable information about possible sources of the short-period waves.

The results in this section are obtained by comparison of the power maps with white-light images, see Sect. 4.2.1. In this analysis also the results were distinguished between quiet and active regions.

4.4.1 The quiet Sun

The most frequent origin of power in these data sets are variations in the granulation, for which the typical time scale is much longer than the period of the observed waves. 50% to 70% of the total observed power is associated with these slow changes. Examples of this can be seen in Fig. 4.10, where one notices the difference between power features at the two levels. The occurrence of power at different height levels has been shifted in time corresponding to the sound speed, so that a change in the granulation pattern occurs at the same time step as the power feature.

At 200km there are more power features visible (Fig. 4.10). The power features tend to follow intergranular lanes, while those features with stronger power tend to follow the borders of the granulation structure. At the higher level, 600km, it looks like there are less power features involved. In the first five images of the time sequence two maxima, marked in the figure with the arrows 1 and 2, appear to be followed by power features which are slight grey, indicating less amount of local power.

The maximum marked with 2, appears through the whole time sequence and seems to be related to the disappearance of a small structure in the intergranular lanes surrounded by larger granules (arrow 3). The change of the power shape which does not correspond

to a similar change of the shape of the granulation pattern might indicate that there is no clear connection between them.

The second maximum which appears only in the first five images is also related to a disappearance of a part of the granulation structure; its shape and change in shape corresponds to that of the granulation pattern. Stronger power features tend to cluster around irregular borders of the granulation structure. The power features at both levels tend to appear at similar locations. Although corresponding power features for the higher level can also be found at the lower level, they seem not to be at identical locations.

The second frequent cause of power is the variation of small granular structures, which cause 12% to 17% of the total observed power. An overview of the granular events which cause short-period waves in the data set DS1 is given in Table 4.7.

Table 4.7: Granular events which cause short-period waves, in the data set DS1, with the percentage of appearing above the 10%.

Data set 1; cause of wave power		
No.	granular event	%
1	slow granulation changes	52
2	fading of a small granule into the background	12
3	changes of abnormal granulation	12
4	bright point-like structure	12

In addition to Table 4.7, the following events also cause short-period wave power:

- fading of a small granule into the background,
- splitting of a granule into two,
- appearance of a granule,
- disappearance of part of a granule,
- merging of two granules into one larger,
- disappearance of a low intensity structure from a granule.

The percentage of the power connected with these events is 12% of the total observed power.

4.4.2 Solar area with G-band structures

Here the data sets which contain G-band structure, DS4 and DS7, will be analysed. Since those data sets with pores in the field of view also show G-band structures, the pore surroundings were also used in this analysis. The most common sources of short-period power are changes of abnormal granulation in the continuum layer. The amount of total power appearing in the small-scale structure is around 60% of the total registered power.

The power originating from these sources is spread over most of the field of view without large amplitude variation and often covers small granulation structures. An example of this source is given in Fig. 4.20. The most striking structures are the three point-like power features which appear at both height levels at the same locations. They are marked with the arrow. It is interesting to notice that at the granulation level there is no structure of similar shape. All three features follow the change of the small-scale structures near the borders of larger granulation structures. Table 4.8 gives an overview over the most common sources of short-period power for these data sets with G-band features.

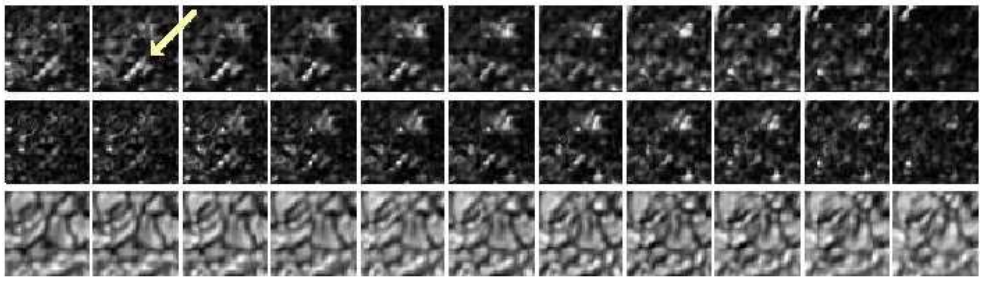

Figure 4.20: Time sequence of 283s from the data set DS5, with a repetition time of 28.3s. The bottom rows represent granulation changes, the middle row power of short-period waves integrated over periods 56s to 120s at the height 200km, and the top row power of short-period waves integrated over the same period range at the height 600km.

Table 4.8: Granular events which cause short-period waves, in the data set DS7.

Data set 7 - cause of wave power		
No.	granular event	%
1	changes in abnormal granulations	56
2	slow changes in the granulation	19
3	fading of a small granule into the background	14
4	appearance of two smaller granules from one larger	11

For the data set DS7, the appearance of granules is found as an additional source. However, the power related to this event is only 3% of the total observed power.

4.4.3 Observations containing a pore

The study of short-period wave sources in these data, DS5 and DS6b, is performed from sub-images without the pore.

Also in these data sets the most common source of short-period waves are changes of small structures. In the data set DS5 it amounts to 70% of the total registered power for this data set. Table 4.9 gives an overview of the sources.

Additional sources with amounts of power below 10% are:

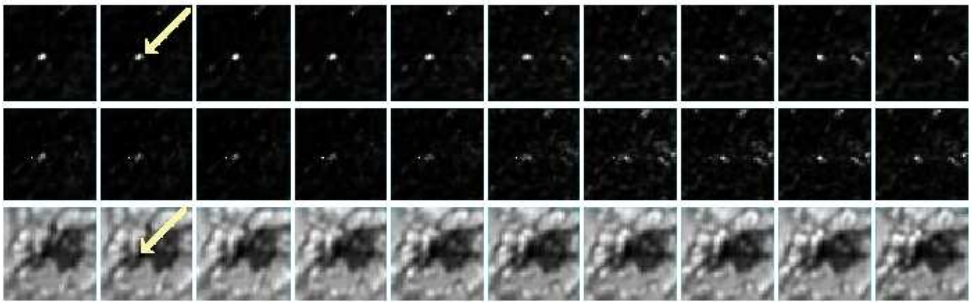

Figure 4.21: Time sequence of 283s from the data set DS5, with a repetition time of 28.3s. The bottom row represents granulation changes, the middle row power of short-period waves integrated over periods 56s to 120s at the height 200km, and the top row power of short-period waves integrated over the same period range at the height 600km.

Table 4.9: Granular events which cause short-period wave, presented for the data set DS5.

Data set 5; cause of wave power		
No.	Event	%
1	changes in abnormal granulations	70
2	slow changes in the granulation	19
3	bright-point-like structures	4
4	appearance of two smaller granules from one larger	3.5
5	appearance of a dark structure inside a granule	3.5

- disappearance of small granules,
- appearance of granules.

Above the pore the amount of power of short-period waves is extremely small. As one can see in the Fig. 4.21, the only power feature, marked with 1, seems to be caused by a bright structure at the edge of the pore, marked with 2, at the beginning of the time sequence. Later the most pronounced maximum seems to drift a bit into darker areas of the pore, without relation to a visible structure. Other faint structures seem to be caused by granular changes, which cannot be determined since the pore in the field of view causes low contrasts in the surrounding granulation.

4.5 Relation between waves of different periods

Differences between neighbouring octaves are found to be not very large since the observations shows that the power behaviour varies slowly with the period. Major changes usually appear for periods near 80s. This section discusses the dependence of waves on the period interval.

4.5.1 Variation of power location with periods

In Fig. 4.22 one can note differences between various periods. For each interval the power over a different period interval appears at different spatial locations. Usually, the most rapid changes occur in the intervals P13, P23, P33, P64 and P72, (interval definition given in Sect. 4.2.3) which often do not have much relation to other periods. In Fig. 4.22 it can be seen that the intensity of the power in the third panel is markedly weakened.

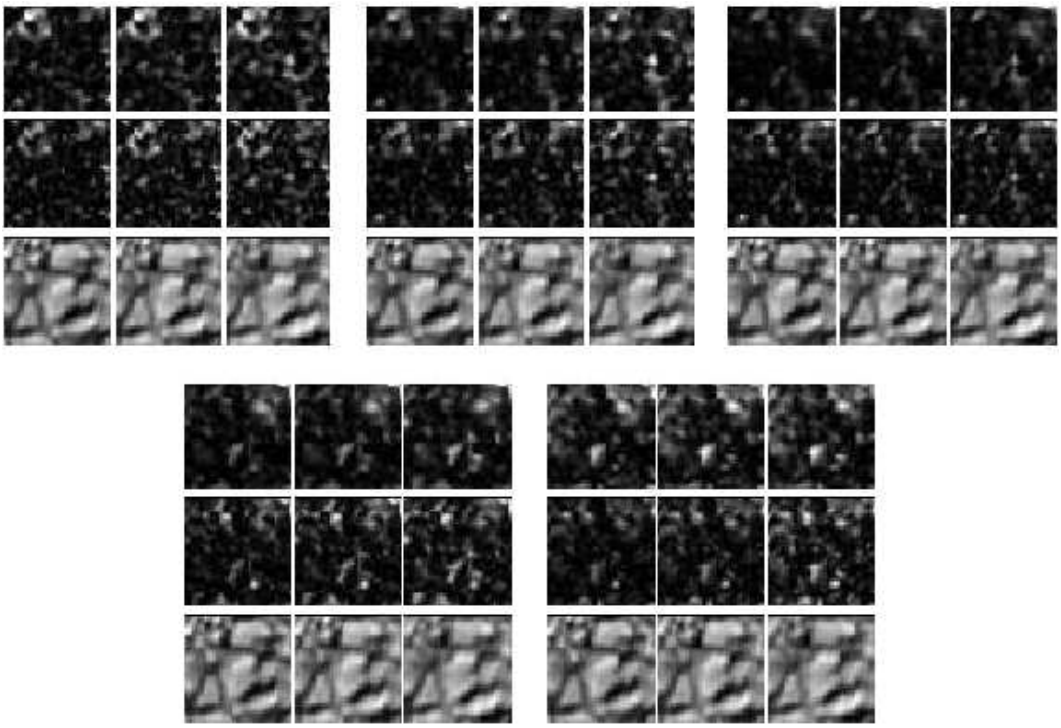

Figure 4.22: Time sequence of 90s in three time steps from the data set DS2. The five panels represent integrated power over the period ranges P21, P22, P23, P24 and P25 (P21 $= (54-65)$s, P22 $= (65-76)$s, P23 $= (76-87)$s, P24 $= (87-98)$s, P25 $= (98-109)$s), at the two different heights of 200km (middle row) and 600km (top row). The bottom rows show the corresponding granular pattern.

For comparison, Fig. 4.23 shows the same time sequence with the power integrated over all period ranges. The general power distribution is quite similar; the only difference occurs for such power features which appear in relation to bright point-like structures.

For data sets stemming from the quiet Sun, the results generally show that this change of power in the period interval around 80s is the most obvious. The Table 4.10 gives an overview of the most prominent events related to changes of short-period waves with the period interval.

The event No.1 happened together with slow granular changes, while event No.3 relates to changes of small structures. The variation of the location of maxima, event No.5, is found in relation with different granular events. In 4% of the cases where a variation over period ranges occurs, one can find that power in P11 has a different location compared with P14; P15 show power at the same locations, as in the former two period

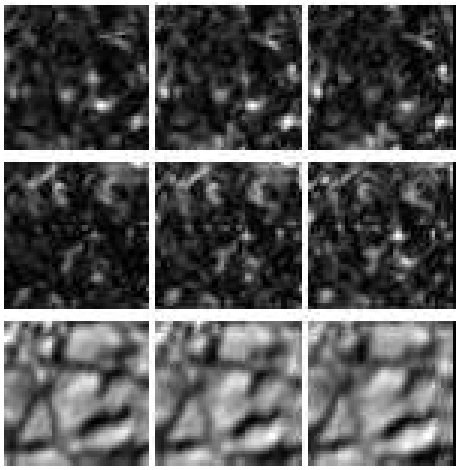

Figure 4.23: Same time sequence of 90s in three time steps from the data set DS2, but with the power integrated over the whole period range from 54s to 109s.

Table 4.10: Events related to difference in the short-period waves visible over the different period intervals. The analysis is done for all ranges given in Table 4.3.

Data set 1: changes of short-period power over the period intervals		
No.	event	%
1	diffuse power features with different shapes over all ranges	43
2	change of the location over the period range around 80s	27
3	diffuse power features with similar shapes over all ranges	13
4	no differences	7
5	maxima at different locations	4

ranges. For the quiet Sun data there is no clear correlation between granular events and the behaviour of short-period waves over the different period intervals.

For the G-band data there is some difference as compared to the quiet Sun observations. In Fig. 4.25 the behaviour above a bright point structure is presented. Fig. 4.24 shows in different sub-panels the power in the different period intervals. It can be noticed that the first two panels, which present power in the intervals P31 and P32, exhibit a similar spatial distribution. Also the last three panels, which represent power ranges P33, P34 and P35, show similar distribution. However, panels 1 and 2 differ significantly from 3, 4, and 5. In particular, the almost central maximum in P33, P34 and P35 does not occur in P31 and P32. This means that those waves cover a period range from 79s to 113s. This maximum also occurs in the integrated power.

Comparison of the integrated power (Fig. 4.25) with that in the different ranges shows that in this example some power of the short-period ranges P31 and P32 does not occur when integrated over the whole period range. This clearly indicates that in this case the power in those two intervals is much smaller than in the other three intervals.

In Table 4.11 an overview of the behaviour of power features over the different period

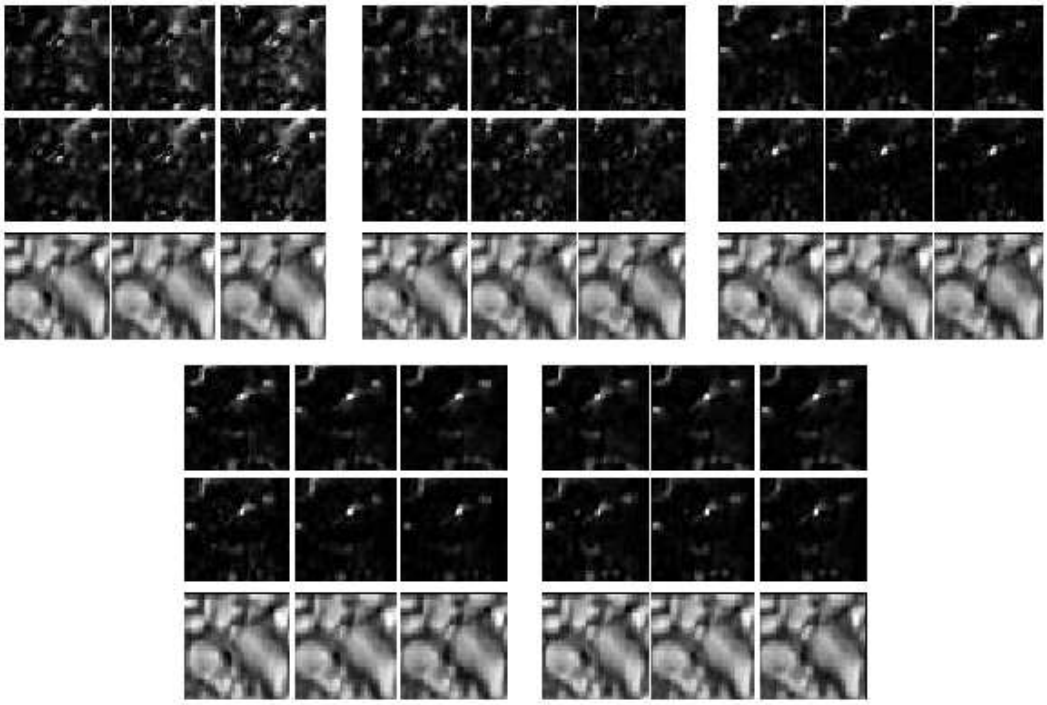

Figure 4.24: Time sequence of 90s in three time steps from the data set DS5. The five panels represent integrated power over period ranges P31, P32, P33, P34 and P35 (P31 $= (56-68)$s, P32 $= (68-79)$s, P33 $= (79-90)$s, P34 $= (90-102)$s, P35 $= (102-113)$s), at the two different heights of 200km (middle row) and 600km (top row). The lower panels show the corresponding granular pattern in the three time steps.

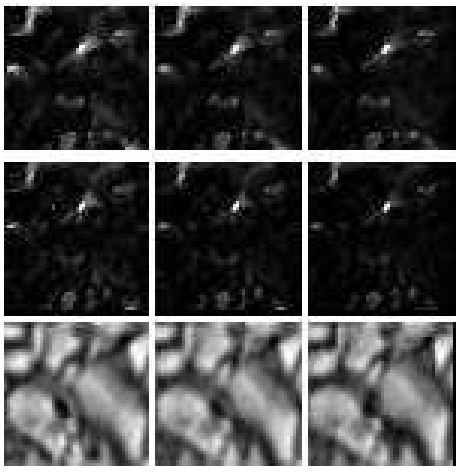

Figure 4.25: Same time sequence of 90 of the same granular change for the data set DS5, but for the integrated power over whole period range.

intervals is given. It is seen that for the data near G-band structures diffuse power features are more frequent, these are usually related to changes of small granulation structures.

In the data set, DS5, there are bright point-like structures, for which almost 90% of the power equally appears in the map with power integrated over the whole period range as in the various period ranges. In the rest of the cases a slightly larger power is observed in the different period intervals compared to the integrated power.

Table 4.11: Events related to differences in the short-period waves visible over the different period ranges.

Data set 7 - changes of short-period power over the period intervals		
No.	event	%
1	similar diffuse power features over all ranges	28
2	change in the position over the range of 70 to 80s	14
3	similar diffuse power features over all ranges	17
4	no differences	13
5	maxima at different locations	25

In the data sets containing a pore the analysis leads to similar results for those locations outside the pore as for the data sets with the G-band structures. This may be expected since the pore surroundings are known to be covered by G-band structures.

Fig. 4.26 show the spatial distribution of power in the period ranges P31, P32, P33, P34 and P35 in the pore and its immediate vicinity. It can be seen that the location of the strong maximum is the same for both heights, whereas the rest of the power is insignificant.

The power maximum is located at the lower end of a lengthy bright structure at the left side of the pore which seems to separate a small extension from the main pore region. One finds no variation of power over the period intervals; accordingly the power feature equally occurs in the map of integrated power.

4.5.2 Comparison of short-period waves with waves of the longer-period

To complete the discussion about differences in the various period intervals I here discuss a comparison between the short and the long-period waves. Such a comparison is only done for the data sets from the quiet Sun, since previous investigations (Espagnet et al. 1996) were done for the quiet Sun as well. In this section I also use conclusions from the results about longer-period waves.

The range of 50 to 200s

Fig. 4.28 presents the variation of power features in the two period intervals 50s to 100s and 50s to 200s. It is seen that features of longer-period (50s – 200s) waves tend to vary more slowly and cluster near specific locations. An interesting event is marked with 1. Power features of short-period waves seem to originate from larger numbers of smaller sources, marked with 2.

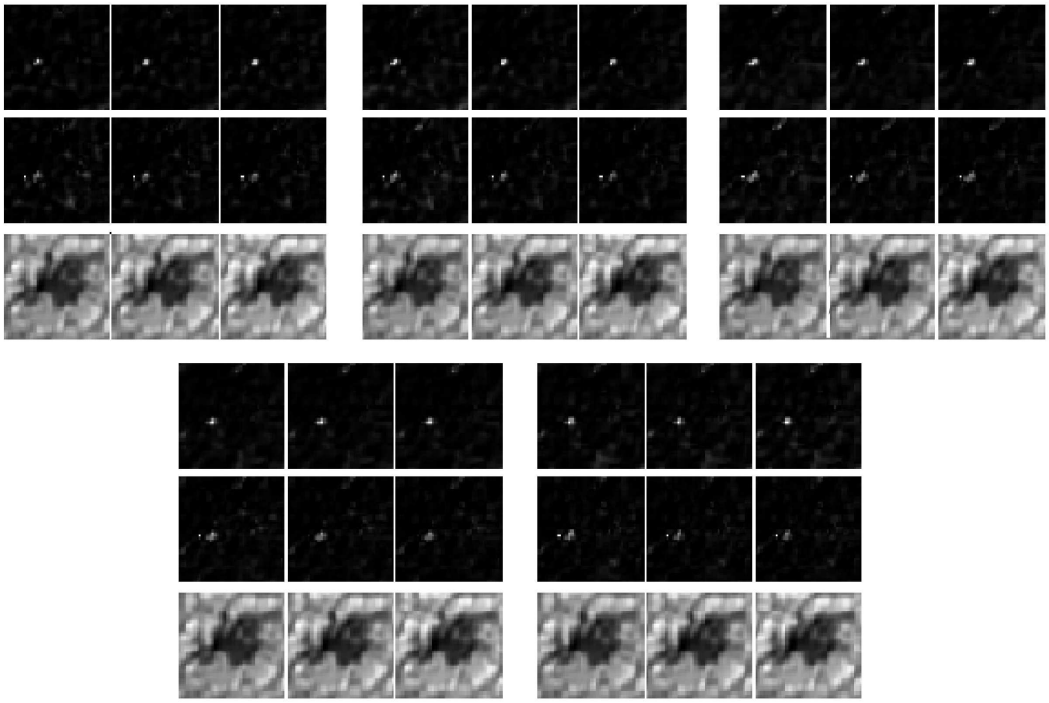

Figure 4.26: Time sequence of 90s in three time steps from the data set DS5. The five panels represent integrated power over period ranges P31, P32, P33, P34 and P35, at the two different heights of 200km (middle row) and 600km (top row). The lower panels show the corresponding continuum pattern in the three time steps.

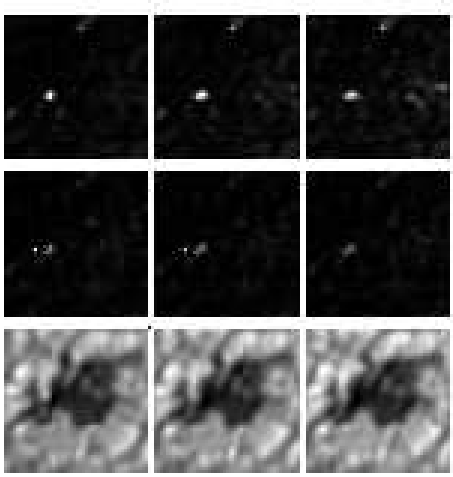

Figure 4.27: Time sequence of 90s in three time steps from the data set DS5.

In Fig. 4.29 the temporal behaviour of features with maximum power is shown. The arrows 1 and 2 mark the power maxima of longer-period waves, and arrows 3 and 4 the power maxima of short-period waves.

Careful inspection of the longer sequence Fig. 4.29 shows that the features of longer-

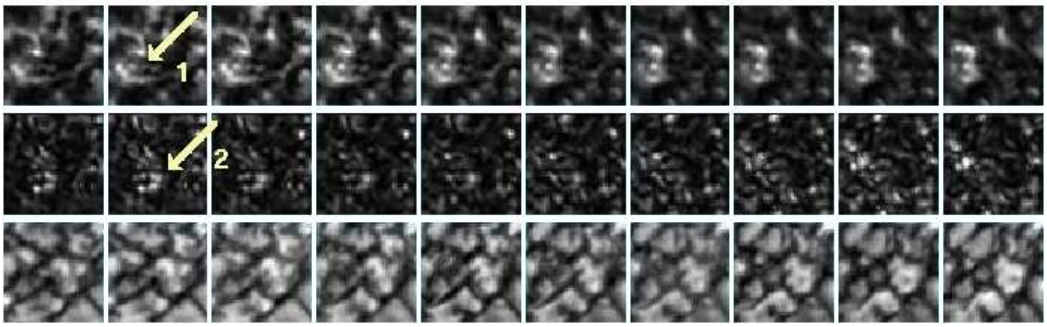

Figure 4.28: Time sequence of 250s from the data set DS1. The top row presents power integrated over the range 50s to 200s, the middle one power integrated over the range 50s to 100s, both at the height of 600km; the bottom row presents the corresponding granulation change.

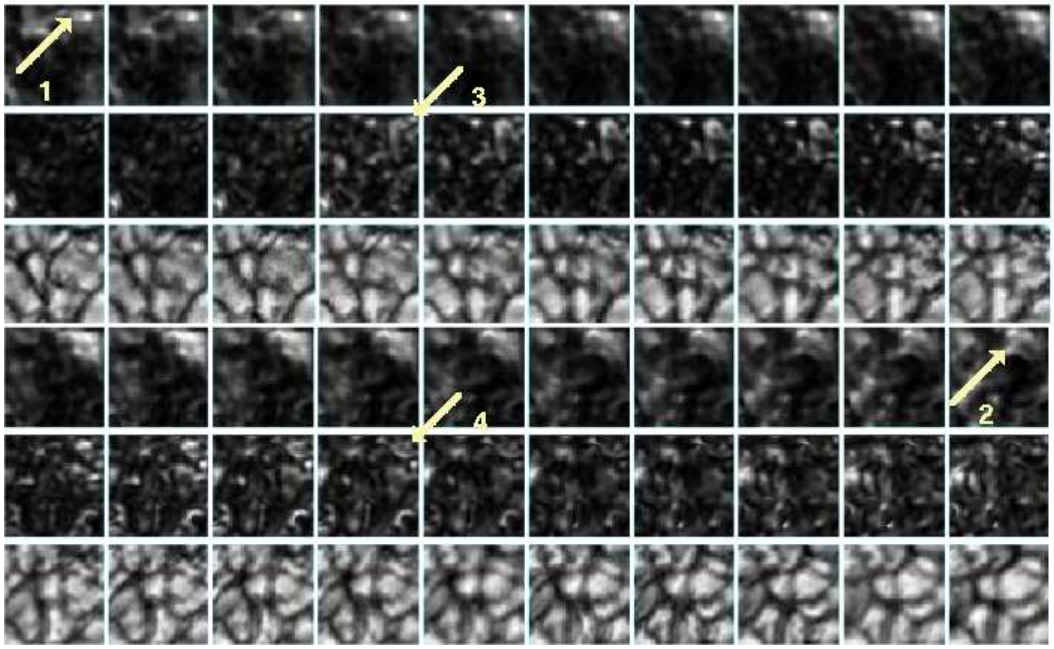

Figure 4.29: Time sequence of 500s from the data set DS1; upper, middle and lower panels like Fig. 4.28 but at a different spatial location.

period waves appear earlier in the time sequence and last longer than the corresponding feature of short-period waves at the same location. In turn, the power features of short-period waves appear later and disappear earlier.

For the same data set, DS1, the wavelet analysis was done two times, yielding maps of power integrated over the two period intervals 50s to 100s and 50s to 200s. The differences in the features occurring in both intervals are evident. They indicate more power in the range 100s to 200s than in the range 50 to 100s, since no structure from the interval 50s to 100s is visible in the power maps of the interval 50s to 200s.

The period range between 175s and 280s

Also for the data set DS6a the wavelet analysis was done two times yielding maps of power integrated over the period intervals 46s to 90s and 46s to 280s. This set of data shows dominant power patterns only in the range 46s to 90s, indicating that the short-period waves have the largest amplitudes. Therefore it was necessary to separate this range, from the one between 175s to 280s.

The power maps of this range show a behaviour of longer-period waves similar to the behaviour of the waves in the period interval 100s to 200s. The changes of their power features are slower and they do not come from the same sources as the short-period waves.

The maxima of the wave power behave similarly as in Fig. 4.29: the features of the longer-period waves last longer than the corresponding power features of the short-period waves at the same locations.

4.6 Travelling of waves through the solar atmosphere

For an effective heating of the chromosphere upwards travelling short-period waves are required. So the next step of the analysis was to determine how the short-period waves travel through the solar atmosphere. As a first step in this analysis a pixel by pixel correlation was attempted.

This method gave $\approx$ 30% correlation between the location of power integrated over the whole period range at the two heights, presuming that waves travel with the speed of sound. For the data sets which contain more small granular structures, the percentage of this correlation was larger, since the power over these structures tends to have similar shapes at both height levels.

The same procedure is done for various period ranges. It was found that the largest percentages of matching power locations occur for comparison within the same period range at both heights. A similar behaviour was observed if one period range, e.g. P11 (see. Table 4.3), was taken for the one height, and the neighbouring one, e.g. P12, for the other height level. However, comparing period intervals not neighbouring, the percentage of the correlation was 20% smaller than the percentage of correlation of neighbouring period ranges. In Table 4.12 one can see an overview of the percentage of the matching short-period power in the different period ranges, assuming that they travel with the speed of sound, $7\,\frac{km}{s}$.

Comparison of the results from the wavelet transform for each pixel showed that waves do travel through the solar atmosphere, but that their velocity is not exclusively the speed of sound. Fig. 4.30 shows the result of the wavelet analysis for one pixel. Those parts of the contour plot presenting power of short-period waves at both heights (marked with the letters A, B, and C) indicate the existence of a time shift. But the areas marked with these letters also show the complexity of the problem. Areas A and B are separate at the height of the 200km while at the height 600 they are joined into one, although the two parts seem to be still visible. The area marked with the C differs not only in time but also in intensity and period between the two heights. This picture might be more complex since the pixel by pixel analysis does not take into account variations of the spatial position of short-period waves, or variations over the period ranges.

Table 4.12: Percentages of matching locations of power features at the two different heights, assuming that the short-period waves travel with the speed of sound, for the data set DS3.

Data set 3; matching locations			
No.	range at 200km [s]	range at 600km [s]	matching [%]
1	56 - 120	56 - 120	15
2	56 - 69	56 - 69	36
3	69 - 81	69 - 81	36
4	81 - 94	81 - 94	36
5	94 - 107	94 - 107	31
6	107 - 120	107 - 120	31

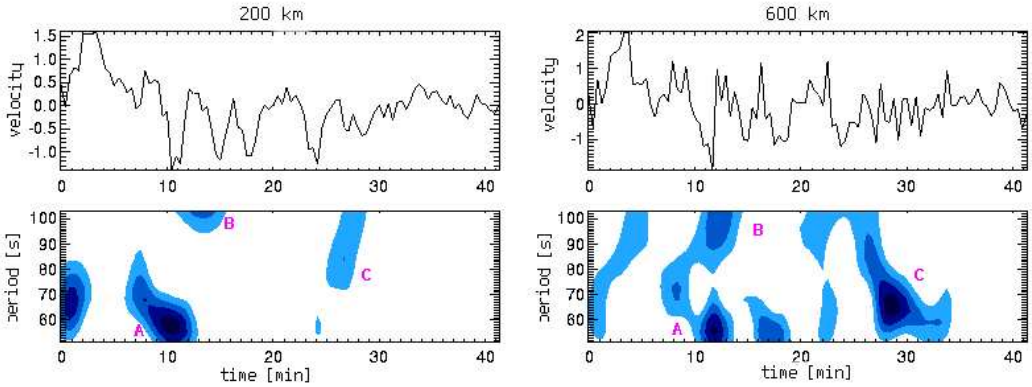

Figure 4.30: Result of the wavelet analysis for pixel (167,112) at the two heights for data set DS1.

4.6.1 Matching of similar power features

Using the pixel by pixel comparison differences between the data sets are now investigated. The results show differences between the various objects of the observations. In this section the reader must bear in mind that in total 8 different data sets are analysed and most of them have different repetition time, which automatically causes the difference in the size of the necessary time steps. Table 4.13 gives an overview of the repetition time for each data set.

The quiet Sun

In those data sets containing the quiet Sun as object of observation the most frequent time shift to match power maxima at both height levels is 71.6s. This corresponds to a velocity of $7.8 \pm 0.6 \frac{km}{s}$, being close to the sound speed. This value is obtained by averaging the measurements over the different data sets. The different cadences of the sets give different time and velocity resolutions, and therefore an averaging of the velocities was necessary.

Table 4.13: Data sets and their repetition time.

Data Sets	
Data set	repetition time (size of one time step) [s]
DS1	25
DS2	27.4
DS3	28.2
DS4	28.4
DS5	28.3
DS6a	22.7
DS6a	22.7
DS7	29.9

In Table 4.14 an overview of some time shifts for the data set DS1 is given.

Table 4.14: Time shifts deduced for the data set DS1 (quiet Sun) and their corresponding velocities and granular events.

Data set 1 - the time shift				
No.	granular event	time shift [s]	velocity $[\frac{km}{s}]$	percentage
1	slow granulation changes	75	5.3	4
2	small changes at the borders of granules	50	8	28
3	bright point-like structure	100	4	4
4	changes in abnormal granulations	100	4	6

In total, for the data set DS1 35% of the events occur with a time shift of 50s, 10% with 75s, 10% with 100s and the rest was not detectable. For the data set DS2, which shows the largest variations, 40% of the events occurred with a time shift of 56s, 40% with 82s, 10% with 109s, the rest not being measurable. For both data sets, the dominant velocity is $7.8 \pm 0.6 \frac{km}{s}$, yet only $\approx 35\%$ of all observed events have this velocity. The second frequent velocity for those data sets is $5.2 \pm 0.4 \frac{km}{s}$.

Also, these quiet Sun data give evidence for rather fast short-period waves. One of the examples is shown in Fig. 4.31. The two arrows in the left panels with velocity power (1 and 2) mark the power feature which was used to determine the time-shift. The arrow in the granulation image (No.3) marks the possible event in the granulation which corresponds to the appearance of the power feature; the total contribution of these speedy short-period waves is around 2%. The arrows 4 and 5 marks the power feature before the time-shift is applied.

The following figures present results from a quantitative comparison of powers features. Fig. 4.32 shows in the left panel the power vs. time without time shift. It can be seen that the power variations do not correspond to each other. The right panel shows the

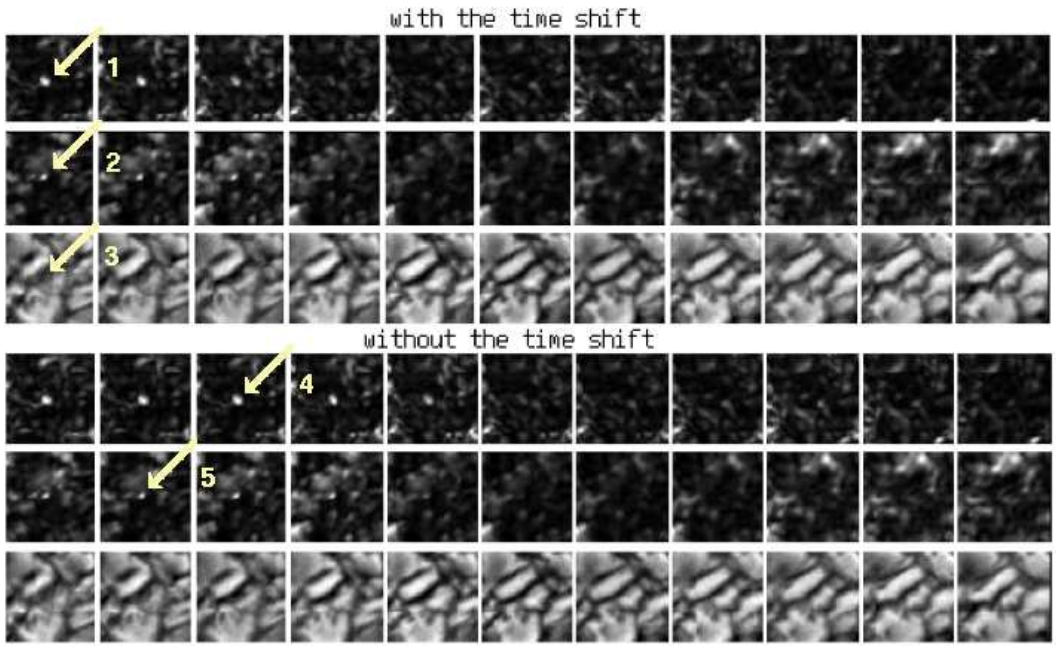

Figure 4.31: Illustration of the time shift of power features for the data set DS1. The time shift in this example is 25s, one time step, which corresponds to a velocity of $16\frac{km}{s}$.

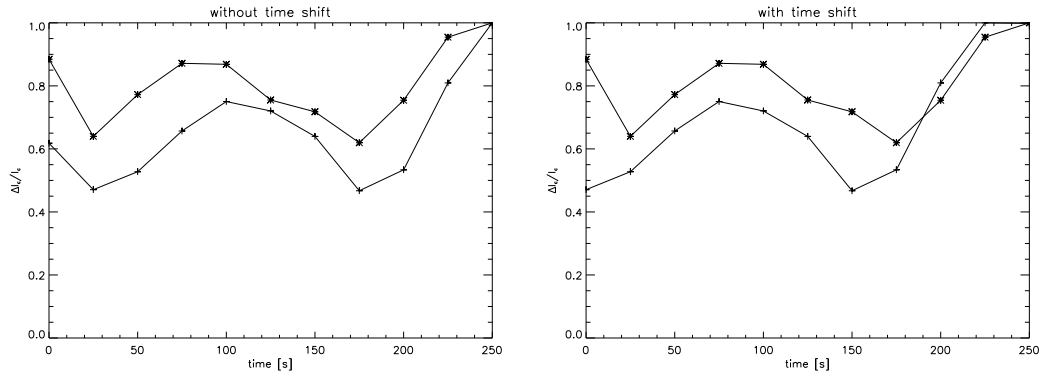

Figure 4.32: Temporal variation of the power spatially integrated over one power feature in the data set DS1. The line with the crosses presents the feature at 600km, the line with stars the feature at 200km height. The diagram gives an example from the data set DS1. A time shift is not applied in the left panel, in the right panel a time shift of one step 25s, is applied fitting optimally the curves, yielding 16km/s.

situation after applying a time shift of 25s. This means that the optimal time shift corresponds to a velocity of $16\frac{km}{s}$, being about twice the sound speed. Also it is visible in this diagram that the power increase at the end does not correspond to the above assumed velocity. That is because this part may belong to another power structure within the spatial region integrated.

The data set DS1 has also examples of features which indicate a time shift corresponding to the speed of sound. Fig. 4.12 shows the behaviour of such a power versus time.

The time shift optimally fitting the two curves is 50s which well corresponds to the speed of the sound.

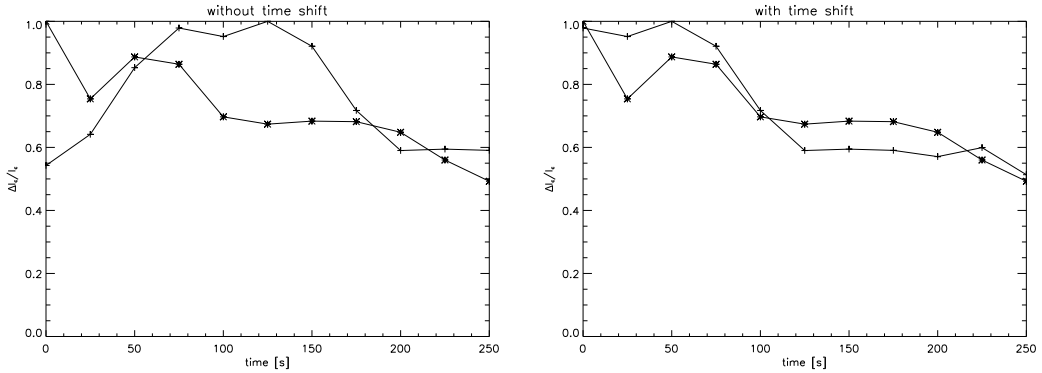

Figure 4.33: Temporal variation of the power spatially integrated over one power feature in the data set DS1. The line with the crosses presents the feature at 600km, the line with stars the feature at 200km height. The time shift is not applied in the left panel. In the right panel a time shift of three steps is applied, corresponding to 75s, yealding the velocity of 5.3km/s.

The data set DS1 has also examples of features which indicate a time shift corresponding to velocities which are slower than the speed of sound. Fig. 4.33 shows a time evolution which requires a time shift of 75s. This example of an evolution is, however, not representative, but it is evident that the time shift produces an exact matching of power changes at two heights only for a small part of the time interval. In particular the very beginning of the series shows a rather different behaviour in both heights, which might need another time shifts.

The G-band structures and pores

It is reasonable to put the results from the data with G-band structures (data sets DS4, DS7) and with pores (data sets DS5 and DS6b) together, since in the latter, regions surrounding the pore show the same behaviour as those with the G-band structures.

All these data sets have the most frequent time shift of three time steps which corresponds to a velocity (averaged over all data sets) of $3.7 \pm 0.4 \frac{km}{s}$. In Table 4.15 an overview of the time shifts and the corresponding granular events is given for the data set DS6b. This data set is a typical representative of the behaviour short-period waves in regions with G-band structures. In this case the dominant time shift is 90s which corresponds to a velocity of $4.4 \frac{km}{s}$, since the repetition time in this data set is 23s. An example for such slowly travelling short-period waves is shown in Fig. 4.34. The two arrows in the bottom panels (1 and 2) mark the power feature which was used to determine the time-shift, before applying the time-shift itself, and arrows 3 and 4 the power feature after the time shift.

The second frequent velocity is $7.4 \pm 0.7 \frac{km}{s}$, being close to the sound speed, and in some data sets it appears with the same percentage as the dominant velocity of the data set DS6b.

Table 4.15: Time shifts for the data set DS6b and their corresponding velocities and granular events.

Data set 1: the time shift				
No.	granular event	time shift [s]	velocity $[\frac{km}{s}]$	percentage
1	slow granulation changes	45	8.9	18
2	small changes at the borders of granules	67	5.9	17
3	bright point-like structures	90	4.45	2
4	changes in abnormal granulation	90	4.45	36

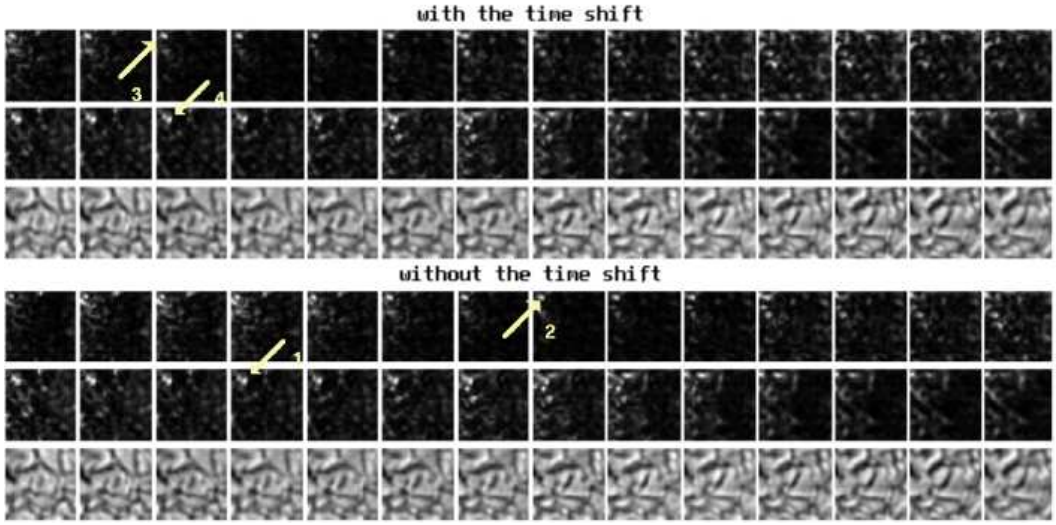

Figure 4.34: Illustration of the time shift of some power features in the data set DS6b. The time shift between 200km (middle) and 600km (upper panel) is 68s which corresponds to a velocity of $5.8\frac{km}{h}$. The power feature used to determine the time shift is marked with arrows on both levels.

Also, for the data set DS5, the velocity $7.4 \pm 0.7\frac{km}{s}$ is the dominant one. However, faster short-period waves also appear. Some of them are so fast that the actual velocity can not be determined due to the finite time resolution; one time step corresponding to 28.3s.

Fig. 4.35 shows examples of two power features (arrow 1) which indicate a time difference smaller than the time resolution of the data set. In Fig. 4.35 the source of the power feature is a small granulation structure with high intensity (arrow 2). In the example Fig. 4.35 one can notice that the intensity of the power structure raises at almost the same time at both height levels; it also decreases apparently at the same time. There are two power features in this example which show this kind of behaviour. This behaviour of power features often occurs in the data sets which include some magnetic structures. Also, the power features which appear around the pore tend to behave in a similar way.

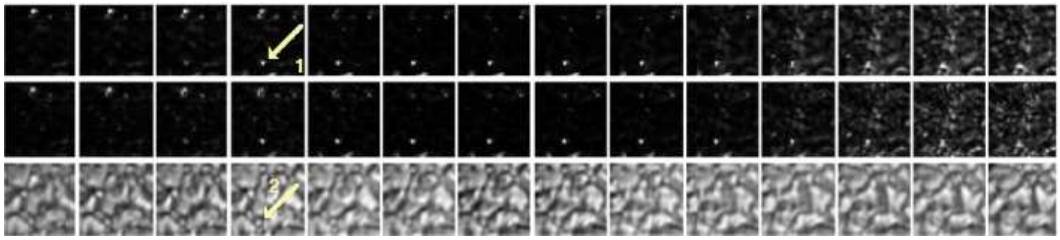

Figure 4.35: Illustration of the time shift of two power features in the data set DS5. The time shift in this example is undetectable, since it is smaller than one time step of these series of 28.3s.

The actual velocity of those waves can only approximately be determined. Since the data set DS6 has a quite fast repetition rate, 22.7s, these waves have to be faster than $17.6\frac{km}{s}$.

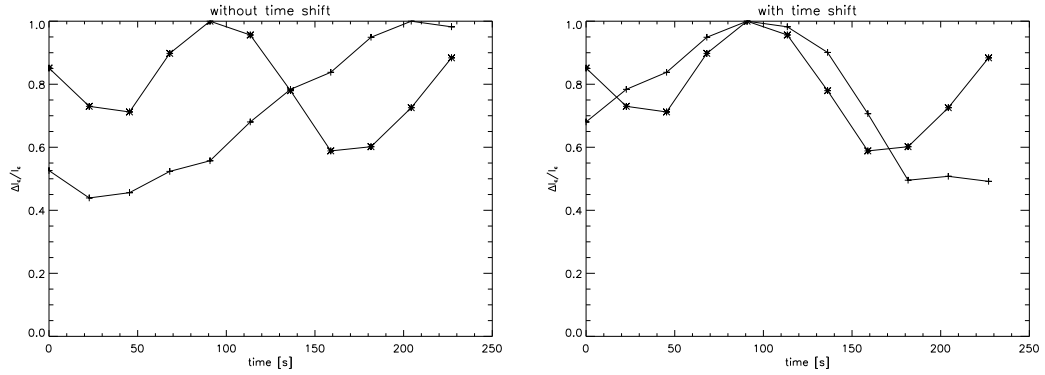

Figure 4.36: Temporal variation of the power spatially integrated over one power feature in the data set DS6b. The line with the crosses presents the feature at 600km, the line with stars the feature at 200km height. In the left panel a time shift is not applied, and in the right panel a time shift of 113s is applied fitting optimally the curves and corresponding to 3.5km/s.

The power variations with time confirm the previous finding. Fig. 4.36 shows one of the slow velocity examples with a velocity of $3.4\frac{km}{s}$.

The example given in Fig. 4.37 shows even slower travelling waves, having velocities of only $3.4\frac{km}{s}$. Yet this behaviour can be due to different time resolutions of both data sets. In that data set where the repetition time is 22.7, shown in Fig. 4.36, the time shift was deduced from five time steps, while in the data set DS7 the time shift was only taken from four time steps. In this example of data set DS7 the evolution of two features is indicated. The second feature has larger power at the 200km level than at 600km; this may be explained by a dissipation of waves.

An example from data set DS6b is shown in Fig. 4.38. The time shift was deduced from three time steps and yields a velocity of $5.9\frac{km}{s}$. Some events in the data sets DS6b and DS5 show waves which are faster than the speed of sound. The example in Fig. 4.39 shows waves which travel with a velocity of $14.3\frac{km}{s}$, being roughly twice the sound velocity. The applied time shift corresponds to one time step, and presents only the end of the evolution of one power feature.

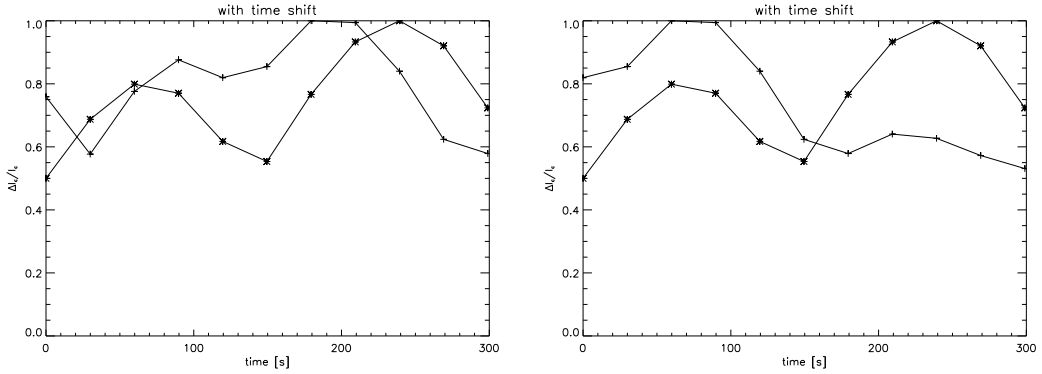

Figure 4.37: Temporal variation of the power spatially integrated over one power feature in the data set DS7. The line with the crosses presents the feature at 600km, the line with stars the feature at 200km height. In the left panel a time shift is not applied, and in the right panel a time shift of 119s is applied fitting optimally the curves and corresponding to 3.4km/s.

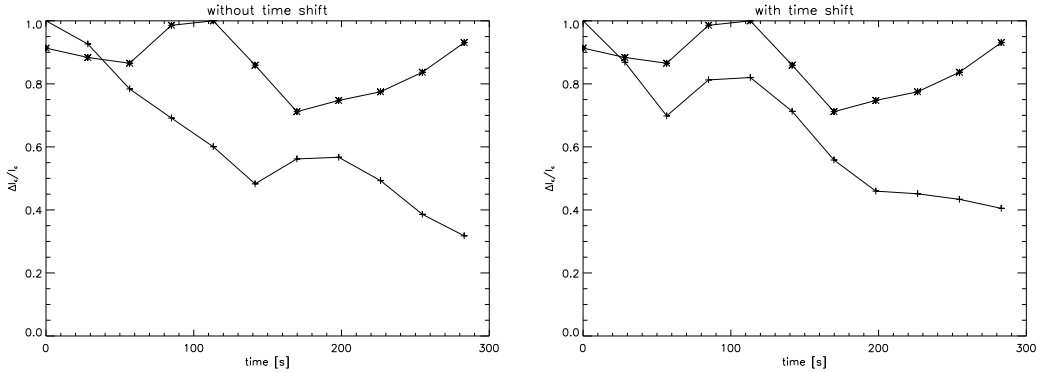

Figure 4.38: Temporal variation of the power spatially integrated over one power feature in the data set DS6b. The line with the crosses presents the feature at 600km, the line with stars the feature at 200km height. In the left panel a time shift is not applied, and in the right panel a time shift of 68s is applied fitting optimally the curves and corresponding to 5.9km/s.

Fig. 4.40 gives the most frequent situation for the data set DS5. The integration area evidently covers two features matching almost perfectly without time shift. In the first 250s of the diagram, one can see that the curve from the lower height level seems to consist of two features superposed on each other. The first, weaker one peaks after 80s and does not appear at the higher level; the second maximum at 180s well matches with the higher level.

The time resolution of this data set with a repetition of 28s, is to low to determine with which velocity the waves travel. The only possible conclusion is that they are faster than $14\frac{km}{s}$.

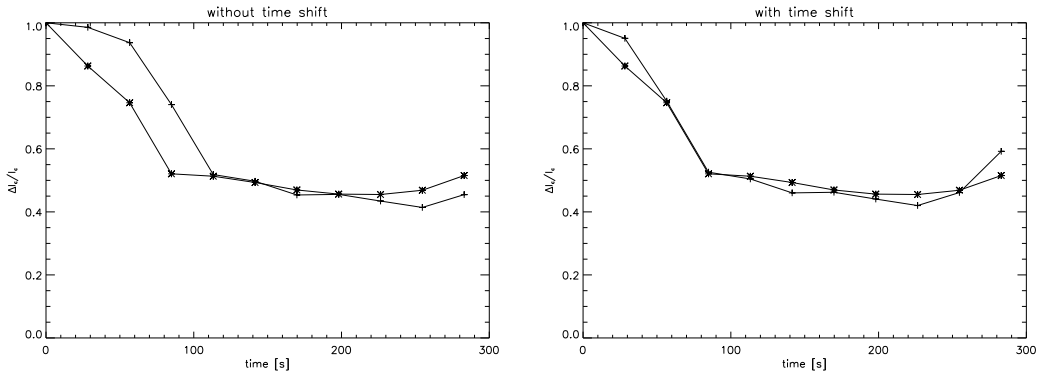

Figure 4.39: Temporal variation of the power spatially integrated over one power feature in the data set DS5. The line with the crosses presents the feature at 600km, the line with stars the feature at 200km height. In the left panel a time shift is not applied, and in the right panel a time shift of 28s is applied fitting optimally the curves and corresponding to 14.3km/s.

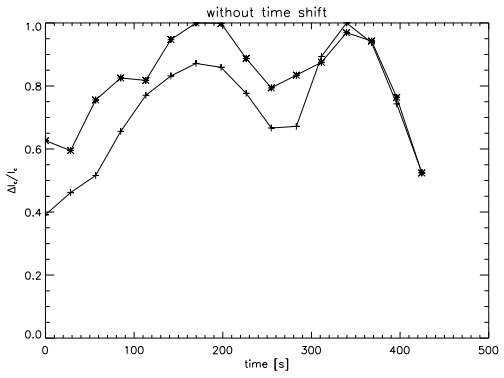

Figure 4.40: Temporal variation of the power spatially integrated over one power feature in the data set DS5. The line with the crosses presents the feature at 600km, the line with stars the feature at 200km height. The diagram is done for the example from the data set DS5. A time shift had not to be applied since both curves match almost perfectly.

4.7 Energy transport and the dissipation of energy

In order to heat the chromosphere by short-period waves, it is necessary that they carry a certain amount of energy and that they dissipate that energy. To determine how much energy is carried by acoustic waves the LTE model (Holweger & Müller 1974) was used to determine the density and the corresponding speed of sound. The energy flux is calculated with the expression:

$$F_h = \rho_h < v^2 > c_h, \tag{4.1}$$

where, ρ_h is the density at the height h, and c_h the corresponding speed of sound. For the two heights used in this work the respective values are presented in Table 4.16

In Fig. 4.7 one can see the signal which is used in this analysis. The filtering removed

Table 4.16: Values of the sound speed and the density used for calculations of the energy flux.

Sound speed and density		
height [km]	speed of sound $[\frac{m}{s}]$	density $[\frac{kg}{m^3}]$
600	6700	$2.74 \cdot 10^{-6}$
200	7300	$7.99 \cdot 10^{-5}$

all waves whose period was above 120s in Fourier domain, in order to suppress the 5min oscillations. It is interesting to notice that in certain parts of right side panels, where non-filtered signals are presented, one can not see short-period oscillations. Just after filtering the short-period waves and their amplitude can be seen (left panels of Fig 4.7), - evidently since they are no more superposed by 5min oscillations.

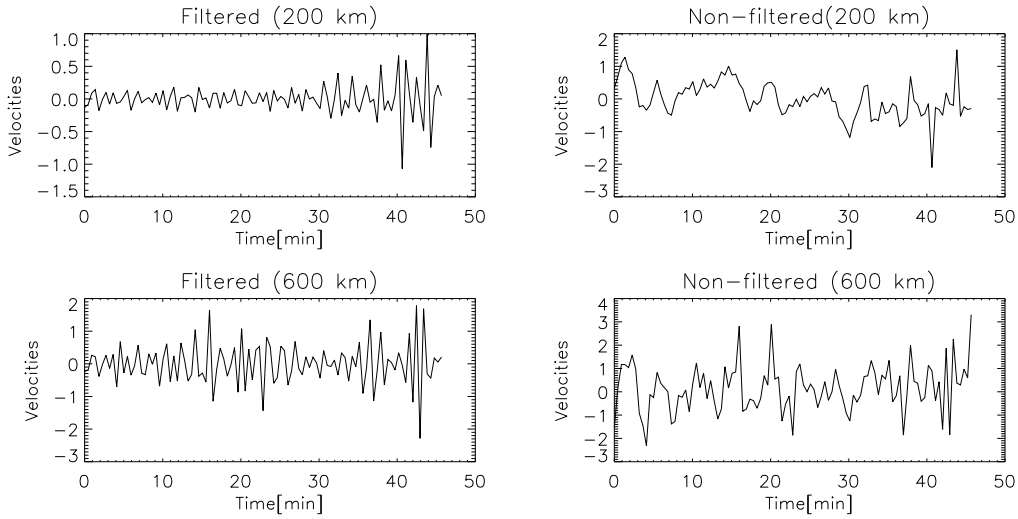

Figure 4.41: Examples of the analysed signals before filtering (right panels) and after filtering for the period range 50s to 120s (left panels).

The average velocity $< v^2 >$ in Eq. 4.1 was determined from the velocity maps at the appropriate height. The averaging was done for each pixel of each velocity map in the time sequence. For this calculation only the data sets DS1, DS2 and DS7 were used. In Table 4.17 the flux values are presented. The error is calculated using the statistical distribution for the low number events, since the number of measurements is quite small, the values are obtained from only three data sets.

The energy flux at the height of 200km is:

$$F_{200} = 6.5 \pm 0.6 \, \frac{kW}{m^2}. \tag{4.2}$$

The energy flux at the height of 600km is:

Table 4.17: The energy flux for the data sets DS1,DS2 and DS7.

The energy flux				
data set	cadence	$F_{600}[\frac{kW}{m^2}]$	$F_{200}[\frac{kW}{m^2}]$	$F_{200} - F_{600}[\frac{kW}{m^2}]$
DS1	25	0.899	6.954	6.054
DS2	27.4	1.583	7.059	5.477
DS7	29.9	0.794	5.375	4.581

$$F_{600} = 1.1 \pm 0.3 \, \frac{kW}{m^2}. \tag{4.3}$$

And the difference between those two energy fluxes is:

$$|F_{600} - F_{200}| = 5.4 \pm 0.5 \, \frac{kW}{m^2}. \tag{4.4}$$

This difference represents the loss of energy flux during the travel of the short-period waves.

Table 4.18: The energy flux for the data sets DS6a and DS6b.

The energy flux				
data set	cadence	$F_{600}[\frac{kW}{m^2}]$	$F_{200}[\frac{kW}{m^2}]$	$F_{200} - F_{600}[\frac{kW}{m^2}]$
DS6a	22.7	2.486	19.732	17.246
DS6b	22.7	8.613	17.936	9.323

The data sets DS6a and DS6b have a cadence of 22.7s, and according to the theory there should be more energy flux detected; the smaller repetition rate allows to measure higher energy flux. Table 4.18 shows the results for these data sets. It can be seen that for the data set DS6a, which has the quiet Sun as object of observation, the dissipated energy flux is $\approx 2 \cdot 10^4 \, \frac{W}{m^2}$, while the energy flux for the data set DS6b is smaller. This result may be explained by the fact that data set DS6b contains a pore above which short-period waves appear quite seldom and averaging over the whole field of view, can thus not yield an amount of energy flux similar to that in the data set DS6a.

To analyse the energy flux above the different granulation structures, the field of view from the data set was cut such that it presents only the respective structure with its close surroundings. From these sub-images the time sequence which contains only the evolution of that structure is taken and then analysed. Table 4.19 shows an overview of the different features and their energy fluxes.

It can be seen that various granulation events produce different amounts of energy flux carried by short-period waves; also the amount of dissipated flux varies. Most energetic are changes at the borders of granules. The slow variations of granulation emit smaller amounts of energy. Events related to a possible magnetic influence (as bright point-like

Table 4.19: The difference of the energy flux for the various granular events.

The energy flux differences			
structure	$F_{600}[\frac{kW}{m^2}]$	$F_{200}[\frac{kW}{m^2}]$	$F_{200} - F_{600}[\frac{kW}{m^2}]$
changes at the borders of granules	0.843	6.848	6.005
small granules	0.796	6.236	5.440
bright point-like structures	0.675	5.929	5.255
changes of abnormal granulations	1.122	6.148	5.026
dark structure in the middle of a granule	1.241	6.066	4.826
slow changes of the granulation	1.027	5.784	4.757

structures and abnormal granulation) do emit a significant amount of energy, while events without possible magnetic influences seem to emit less energy.

5 Summary and conclusions

This work analyses short-period waves in the range from of 46s to 120s. They are determined from two height levels in the solar atmosphere at 200km and 600km above the continuum forming atmospheric layer. Information from these two heights were either deduced from core and wing of the strong Fe 543.45nm line or from the core of Fe 543.29nm (200km) and Fe 543.45nm (600km).

The two-dimensional images from different wavelengths were corrected for disturbing influences from the Earth's atmosphere by restoration techniques. The finally obtained time series of two-dimensional Doppler maps at two height levels were used to determine the spatial and temporal behaviour of short-period waves, i.e. their location within the solar white-light structure, their vertical velocity, their dependence on the period range, and their energy content.

The results showed that short-period waves do exist at different heights. Their power is more pronounced at 600km than at 200km height. They show a large variety of power amplitudes and frequencies. Their spatial distribution indicates morphological differences of the power at the two height levels: the power features occupy smaller areas at 200km than at 600km height. This can be explained by a spatial enlargement of the short-period waves when travelling upwards (Sect. 4.1). Comparison with the solar white-light structure indicates that power features which are related to different sources can merge into one bigger feature; a fact which is characteristical for acoustic waves (Lighthill 1951).

5.1 Location of power

The data used for this work were observed in (a) quiet solar regions, (b) active regions with G-band structures, and (c) active regions containing a pore. It is found that these different object of observation show substantial influences on the results (see Sect. 4.3).

In the data sets from the *quiet Sun*, the most frequent locations of short-period power are dark intergranular areas; this concerns 70% of the total power. The power features usually follow the intergranular lanes, but they partly cover also granules. The maxima located in intergranular lanes often appear just before some granular change starts. The time difference to such granular event can not exactly be determined since it is very close to the time resolution of the data. The remaining percentage of power is mostly located 'above' small structures which resemble G-band bright points.

Concerning the temporal evolution, slow changes of the granulation pattern are most frequently followed by the appearance of short-period wave power; such changes are the most common behaviour in the present data sets. The second frequent location of power are dark areas in abnormal granulation (see Sect. 4.2.4).

The data sets with *G-band structures* also show a clear tendency for short-period waves to appear 'above' intergranular areas. However, in contrast to the quiet Sun, these cases concern only $\approx 50\%$ of total power. Maxima related to bright point-like structures occur for 40% of the all power features. The temporal evolution shows that the most frequent 'causes' of short period waves near G-band structures are changes of small white-light structures (similar as for the quiet Sun). More than 60% of the total observed power is related to this kind of structure evolution. In cases of an isolated white-light structure, the corresponding power feature tends to 'surround' the intensity structure. The temporal appearance of short-period power features also indicates that they are most probably related to turbulence eddies which are spatially smaller.

The data sets with a *pore* show similar results as those with G-band structures when considering only the pore surroundings. Inside the pore there are almost no power structures; the few ones which appear tend to be related to small bright features at the boundary and inside the pore. A pixel by pixel comparisons of the amount of powers with the corresponding continuum intensity shows an interesting clustering of power in low intensity regions. This indicated power which appears above the pore itself.

Fig. 4.21 shows an untypical but interesting behaviour where a power feature drifts away from a white structure at the edge of the power to an area inside the power where apparently no additional white-light structure exists. This may indicate that either the true origin of that power feature is not resolved at the spatial resolution achieved, or that waves have a horizontal component which cannot be measured.

In all three regions (quiet Sun, G-band regions, pore surrounding) the power is mostly related to down flow regions. The percentage of power 'above' dark areas is reduced near magnetic fields as can be seen from the different results for the quiet Sun and for regions with G-band structures (incl. pore surroundings). The latter are known to closely relate to the existence of small flux concentrations in intergranular lanes. Probably, these are responsible for the reduced occurrence of short period wave power 'above' dark areas from 70% to 50%.

5.2 Periods

Some power features of short-period waves tend to vary with the period interval. Power features in different period ranges do not show preferred relation to particular white-light structures. However, similar granular events tend to cause differently distributed power in the various period ranges, see Sect. 4.5.

Comparison with waves of much longer period shows their different behaviour as that of short-period waves. Previous work, (Espagnet et al. 1996), finds that the longer-period waves are located in the intergranular lanes and that their source is deeply rooted in the granulation layer. The present results for the long-period waves establishes that finding: the appearance of power in intergranular lanes with slow temporal evolution, and a tendency that the power maximum appears after the maximum of the temporal variation of the white-light structure.

The short-period waves are mostly related to intergranular lanes, however, with a different temporal evolution: the maximum of the power feature tends to follow more closely

the temporal change of the white-light structure than the long-period wave power. This indicates that the short-period waves are formed closer to the solar surface, and that different periods are associated with different spatial scales.

5.3 Travelling

The short-period waves travel through the chromosphere. This travelling seems to be highly complicated and affected by different white-light structures and their evolution (see Sect. 4.6).

A large percentage of the short-period waves observed in the *quiet Sun* travels with the dominant velocity (averaged over the data sets) of $7.8 \pm 0.6 \frac{km}{s}$, being close to the sound speed. Also very slow waves appear in these data sets with the second most frequent velocity of $5.2 \pm 0.4 \frac{km}{s}$.

The fastest waves in these data sets travel with a velocity of approximately twice the speed of sound, but in total they cover less than 5% of the observed velocities.

In the data sets with the *G-band structures and pores* the waves tend to be slower. The most common velocity is smaller than the speed of sound. The dominant velocity averaged over the data sets in active regions is $3.7 \pm 0.4 \frac{km}{s}$, and the second frequent velocity is $7.4 \pm 0.7 \frac{km}{s}$.

The fastest waves appear above white-light structures which look like the G-band bright points. Their velocity cannot be measured, since the changes in the power features seem to happen simultaneously at both heights, at the time resolution achieved in this work. The power features which appear near the boundary of the pore and in the pore belong to this group of very fast waves.

The analysis of all data sets shows that short-period waves travel with different velocities. The interval of observed velocities starts with $3.7 \pm 0.4 \frac{km}{s}$ but the upper limit can not be determined at the temporal resolution achieved in this work.

The data sets with the different objects of observations indicate that the magnetic field has an influence on the short-period waves. The presence of magnetic field may then partly inhibit acoustic waves. Possibly, waves at such locations are markedly affected by the magnetic field, e.g. occurring as magnetic or magneto-acoustic waves.

The results of the work by (Domìnguez 2004) may explain the complex situation in the quiet Sun, since the percentage of varying velocities in this study agrees with those findings for magnetic field in the quiet Sun which say that magnetic fields in the quiet Sun are more complex than previously thought, and high values of the field strenght, up to 10^{-1}T, may well appear.

5.4 Energy

The short-period waves carry substantial energy. Since the data sets have different temporal resolution, the lower limits of the short periods range form 50s to 60s. The energy flux, for waves in the period range of 50s to 120s at a height of 200km is:

$$F_{200} = 6.5 \pm 0.6 \, \frac{kW}{m^2}. \tag{5.1}$$

The energy flux at a height of 600km is:

$$F_{600} = 1.1 \pm 0.3 \, \frac{kW}{m^2}. \tag{5.2}$$

And the difference between those two energy fluxes is:

$$F_{200} - F_{600} = 5.4 \pm 0.5 \, \frac{kW}{m^2}. \tag{5.3}$$

This energy flux is affected by smearing with the Airy function of the telescope, meaning that the actual energy flux can be higher.

The data set with period ranges of 45s to 96s clearly shows that they carry a larger amount of the energy, see Sect. 4.7. This is in agreement with theory which predicts that the maximum of transported power will occur for waves of the periods around 40s.

Therefore, one can conclude that the short-period waves carry enough energy to support the heating of the solar chromosphere.

6 Suggestions for future investigations

The present work can not yield a 'final' picture of the wave packets travelling into the chromosphere. Clearly, additional research is necessary. Some suggestions may be drawn from the present work:

6.1 Instrumental

For the FPIs, the optimally scan direction is toward the blue; hence the fainter line from lower layers should be located at longer wavelengths than the stronger line from higher layers. Keeping for the latter Fe 543.45nm as most suitable, the lower layers near 200km should be investigated from the redwards located Ni 543.56nm. Besides, that Ni line is less Zeeman sensitive ($g = 0.5$) as compared Fe 543.29nm ($g = 0.667$). Unfortunately, the Ni line was not used because the FPI should not be changed for other FPI observations which did not investigate travel times.

As a consequence, upwards travelling waves can only be studied by comparison of Fe 543.29nm from the first scan with Fe 543.45nm from the second scan. The first Fe 543.29nm is measured 13s earlier than the deeper line where the waves are expected to start. I thus had to adjust the time shift accordingly for all data sets which were taken in two lines.

6.2 Information from the granular pattern

A more quantitative comparison of the continuum intensity pattern with the related power maxima could be done by time series of the respective intensity feature at the same location as the power maximum. In case of a clear relation of power to isolated, small features their continuum intensity could be integrated over a reasonable area and then plotted versus time as was done for the power features in Sect. 4.6. This procedure would also allow to determine a possible time shift between the development of the intensity feature at continuum level with the power features at 200 and at 600km height.

6.3 Information from the line profiles

An interesting question related to short-period power is the location within magnetic structures. A simultaneous measurement of the Zeeman effect meets difficulties with the repetition rate (cadence time) due to long integrations required (Domìnguez 2004). Images in the G-band would yield such information at a quick repetition rate; however,

the 430nm wavelength is too far from the 543 nm line pair required for the wave analysis: Speckle information for the latter could hardly be extracted from the first.

One of the future research could address the study of line profiles and their behaviour in areas where the short-period power was observed. One of the most puzzling things is the cause of the various velocities of wave packet propagation.

A promising possibility to get information about magnetic structures is the 'residual intensity effect', which indicated magnetic fields as reduced line depth (Chapman & Sheeley 1977). This effect occurs for all lines but it would be superposed by a magnetic splitting; this is not the case for the low Zeeman sensitive lines used for this analysis.

Since the line gap effect or line weakening increases with line strength (Stellmacher & Wiehr 1979), Fe 543.45nm will be more sensitive to magnetic fields than the fainter lines (either Fe 543.29nm or Ni 543.56nm). The continuum intensity is required to normalize the line profile for a determination of the 'line gap' effect.

$$I_\lambda^{rel} = \frac{I_\lambda}{I_{cont}}. \tag{6.1}$$

Yet even the line 543.29nm shows 'line gaps'.

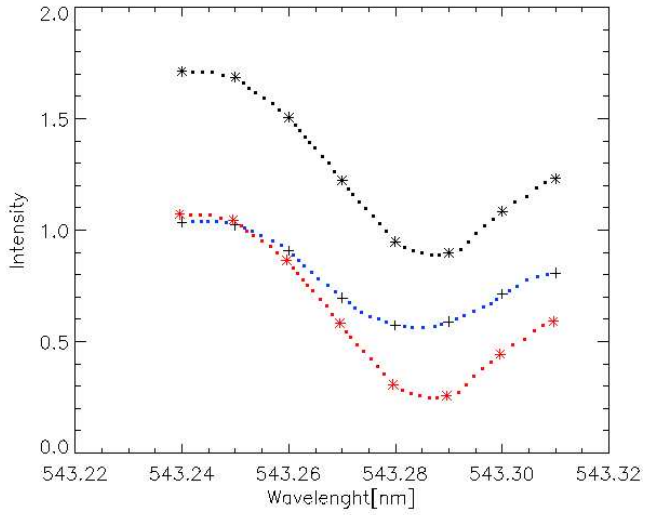

Figure 6.1: The averaged profiles of the spectral line Fe I 543.29nm from data set DS4 for the areas where short-period wave power travels approximately with the speed of sound. Black dotted line with stars represents profiles averaged over regions where short-period waves cover only 4% of the total area. Blue dotted line with crosses represents mean profiles from region with short-period waves covering 70% of the total area, and the red dotted line with stars represents the average profile from larger area downscaled to the intensity level of the averaged line of the smaller area.

Figures 6.1, 6.2, 6.3 give few examples of residual intensity effects related to short-period waves of different velocity. Ones sees reduced intensity in regions where short-period wave power is meassured. This is due the fact that power maximum from short-period waves preferably occur in intergranular lanes. When normalizing the line profiles

to their corresponding continuum, this effect is eliminated, and variations of the relative profiles can be studied.

The few examples show that it is generally possible to determine the residual intensity effect for power locations and to thus extract a possible relation to the wave velocity.

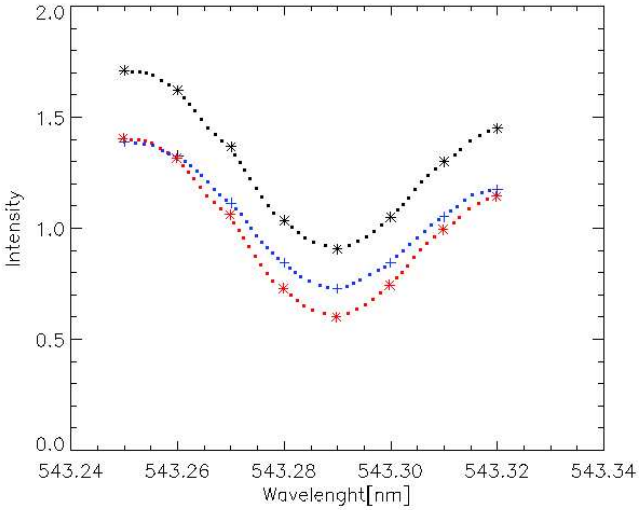

Figure 6.2: Same as Fig. 6.1, but for locations with waves faster than sound speed.

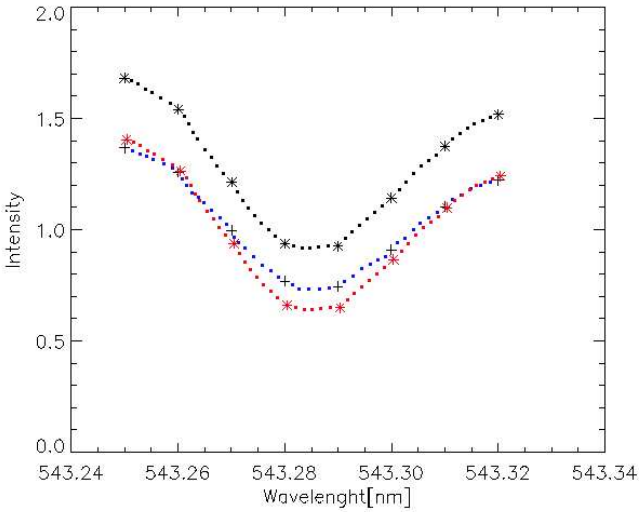

Figure 6.3: Same as Fig. 6.1, but for locations with waves slower than sound speed.

Some of the profiles analysed did not show any line weakening. Hence, a more extended statistics of the relation between wave speed and line gap regions is required to obtain reliable information about the influence of magnetic fields on the short-period waves.

A Appendix 1

A.1 Fabry- Perot interferometer

Fabry-Perot interferometers are capable to assure extremely high spectral resolution, are quite efficient, and spectrally tunable. They are constructed with two partially transmitting mirrors of reflectance R that are parallel to each other. Those mirrors form a FP cavity.

An incident beam is multiply reflected between these parallel surfaces, at each reflection a fraction T of the intensity is transmitted and these fractions interfere in the outgoing beam. If the angle of incidence is Θ, the path difference between two successive beam fractions is $\Delta = 2ndcos\Theta$, and the phase difference is:

$$\delta = \frac{2\pi\Delta}{\lambda} = \frac{4\pi ndcos\Theta}{\lambda}. \tag{A.1}$$

For an incoming wave of form $e^{i\omega t}$ the absolute transmitted and reflected wave amplitudes are $T^{1/2}$ and $R^{1/2}$, respectively. Considering all the reflections and the concomitant phase differences, the outgoing wave represents a geometric series:

$$Ae^{i\omega t} = Te^{i\omega t} + TRe^{i(\omega t+\delta)} + TR^2e^{i(\omega t+2\delta)} + ... \tag{A.2}$$

or shortly written as:

$$A = T(1 + Re^{i\delta} + R^2e^{i2\delta} + ...) = T/(1 - Re^{i\delta}) \tag{A.3}$$

Therefore we can get the intensity of the outgoing beam as:

$$I = AA^* = \frac{T^2}{1 - 2Rcos\delta + R^2} \tag{A.4}$$

or

$$I = I_{max}(\frac{1}{1 + \frac{4R}{(1-R)^2}sin^2\frac{\delta}{2}}), \tag{A.5}$$

where

$$I_{max} = \frac{T^2}{(1 - R)^2}. \tag{A.6}$$

It is obvious that the transmission is periodic, and the m-th maximum is at $\delta = 2\pi m$ or at wavelength:

$$\lambda = \frac{2nd}{m} cos\Theta. \tag{A.7}$$

This is the condition for constructive interference of a transmitted wave front. The expression for the free spectral range or distance between two successive maxima is:

$$FSR = \frac{\lambda}{m} = \frac{\lambda^2}{2\,n\,d\,cos\Theta}. \tag{A.8}$$

The transmission peaks become narrower as R approaches 1. If the width is small in comparison to the free spectral range, it is possible to expand the $sin(\delta/2)$ in:

$$I = I_{max}(\frac{1}{1 + \frac{4R}{R^2} sin^2 \frac{\delta}{2}}), \tag{A.9}$$

and obtain for the full width $\Delta\lambda$ at the half maximum transmission:

$$\Delta\lambda = \frac{FRS}{\mathcal{F}}, \tag{A.10}$$

where

$$\mathcal{F} = \pi \sqrt{\frac{R}{1-R}} \tag{A.11}$$

is the finesse of the interferometer. The finesse is the ratio of the free spectral range and the spectral resolution.

The free spectral range of a FPI is rather small, for $\lambda = 500$nm and $d = 1$mm we have $FSR \approx 0.13$nm. Therefore further filters are required to select a particular transmission maximum. For an optimally high maximum transmission a combination of two etalons is used to select the appropriate range. The transmission maximum and free spectral ranges of the etalons are essentially determined by the plate separations d. Therefore the ratio of these separations must be chosen such that the unwanted transmission windows are closed. Pre-filters, in our case interference filters, must still be applied in order to select a certain spectral band. Their pass bands can be broad thus assuring a satisfying transmission.

The wavelength scanning trough a spectral line is done by computer controlled variation of the spacing of the etalons by means of Piezo elements.

B Appendix 2

- Object of observations: granulation, quiet Sun, disc centre
- Lines: Fe I $543.45nm$ and Fe I 543.29nm,
- Plate distances: $d = 1.5mm$(FPI1), $d = 0.125mm$(FPI2)
- Temperature in OL2: 18^oC

B.1 2003

- Date of observation: 8.10.2003
- Position of Coelostat: (30^o)
- $P_o = -5.8^o$, $B_o = 2^o$, $R_{Sun} = 962$"
- Duration of one scan inclusive data storage: $t = (28.2 \pm 0.5)s$
- 108 images per scan, 18 positions in both line, 6 images per wavelength position, exposure time: $30ms$
- Start of scanning (sj1): 7:30 UT, end of scanning: 8:27 UT

B.2 2004

B.2.1 22.6.2004

- Date of observations: 22.6.2004
- Position of Coelostat: 0^o
- $P_o = -5.8^o$, $B_o = 2^o$, $R_{Sun} = 944.5$"
- Duration of one scan inclusive data storage: $t = (28.2 \pm 0.5)s$
- 108 images per scan, 18 positions, 6 images per position, exposure time: $30ms$
- Start of scanning (sj1): 7:30 UT, end of scanning: 8:27 UT

B.2.2 26.6.2004

- Date of observations: 26.6.2004
- Position of Coelostat: 0^o
- $P_o = -4^o$,$B_o = 2.5^o$, $R_{Sun} = 944.3$”
- Duration of one scan inclusive data storage: $t = (22.7 \pm 0.3)s$
- 91 images per scan, 13 positions, 7 images per position, exposure time: 20ms
- Start of scanning: 9:25 UT, end of scanning: 10:40 UT

Bibliography

[Bendlin et al. 1992] Bendlin, C., Volkmer, R., Kneer, F., 1992, A new instrument for high resolution, two-dimensional solar spectroscopy, A& A 257, 817

[Berkefeld & Soltau 2001] Berkefeld, Th., Soltau, D., MCAO at the German solar Vacuum Telescope, 2001, Venice 2001, Beyond Conventional Adaptive Optic

[de Boer 1996] de Boer, C.R., 1996, Noise filtering in solar speckle masking reconstructions, A&A Suppl. Ser. 120, 195-199

[de Boer & Kneer 1994] de Boer, C.R., Kneer, F., 1994, Speckle observations of solar granulation, IAUS, 158, 398D

[de Boer et al. 1992] de Boer, C.R., Kneer, F., Nesis, A., 1992, Speckle observations of solar granulation, A&A, 257, L4-L6

[Bothmer 2004] Bothmer, V., 2004, Sonnenkorona, course at Universitaet Goettingen

[Carlsson & Stein 1995] Carlsson, M., Stein, R.F., 1995, Does a nonmagnetic solar Chromosphere exist?, ApJ 440, L29

[Chapman & Sheeley 1977] Chapman, G.A., Sheeley JR., N.R., 1977, An improved measurement of a spectrogram of a 'gap', SoPh, 51,61C

[Deubner & Laufer 1983] Deubner, F.L., Laufer, J., Short-period oscillations, 1983, SoPh 82, 151D

[Domìnguez 2004] Domìnguez, I.F., 2004, Quiet Sun Magnetic Fields, PhD Thesis, Goettingen University

[Eibe et al. 2001] Eibe, M.T., Mein, P., Roudier, Th., Faurobert, M., 2001, Investigation of temperature and velocity fluctuations through the solar photosphere with the Na I D lines, A&A 371, 1128-1136

[Espagnet et al. 1996] Espagnet, O., et al., 1996, Spatial relation between the 5-minute oscillations and granulation pattern, A& A 313, 297-305

[Fleck & Deubner 1989] Fleck, B., Deubner, F.-L., 1989, Dynamic of the solar atmosphere II. Standing waves in the solar chromosphere, A&A 224, 245-252

[Graps 1995] Graps, A., 1995, An introduction to wavelets, 1995, IEEE Computational Science and Engineering, vol.2, num.2

[Hansteen et al. 2000] Hansteen, V.H., Betta, R., Carlsson, M., 2000, Rapid intensity and velocity variations in solar transition region lines, A&A 360, 742 -760

[Hoekzema et al. 2002] Hoekzema, N.M., Rimmele, T.R., Rutten, R.J., 2002, Small scale topology of solar atmospheric dynamic, V. Acoustic events and internetwork grains, A&A 390, 681-690

[Holweger & Müller 1974] Holweger, H., Müller, E.A., 1974, The photospheric barium spectrum: solar abundance and collision broadening of BaII lines by hydrogen, SoPh 39, 19

[Howell 2000] Howell, S.B.,2000, Handbook of ccd Astronomy, Cambridge University press

[Janssen 2003] Janssen, K., 2003, Struktur und Dynamik kleinskaliger Magnetfelder der Sonnenatmosphaere, Ph.D. Thesis, Goettingen University

[Kalkofen 1990] Kalkofen, W., 1990, The heating of the quiet solar chromosphere, IAUS, 142, 197K

[Kalkofen 2001] Kalkofen, W.,2001, The case against cold dark chromospheres, AJ, 557:376-383

[Keller & von der Lühe 1992] Keller, C.U., von der Lühe, O.,1992, solar speckle polarimetry, A&A 261, 321-328

[Kneer & Uexküll 1999] Kneer, F., von Uexküll, 1999, Diagnostic and dynamic of the solar chromosphere, A. Hanslmeier and M. Messerotti(eds.), Motions in the solar atmosphere, Kluwer Academic Publishers, Netherlands, 99-118

[Kneer 2002] Kneer, F., 2001, solar photosphere and chromosphere, lectures from IMPRS.

[Knox & Thompson 1974] Knox, K.T., Thompson, B.J., 1974, recovery of images from atmospherically degraded short exposure photographs, AJ, 193:L45-L48

[Korff 1973] Korff, D.,1973, Analysis of a method for obtaining near diffrection limited information in the presence of astmospheric turbulence, OSAJ, 63,971

[Koschinsky et al. 2001] Koschinsky, M., Kneer, F., Hirzberger, J., 2001, Speckle spectra - polarimetry of solar magnetic structures, A&A 365,588-597

[Kostyk & Schukina 1999] Kostyk, R.I., Shchukina, N.G., 1999, Local 5-min oscillation above solar granules and Intergranular Space, Astronomy letters, 25, No.10

[Krieg et al. 1998] Krieg, J., Kneer, F., Koschinsky, M., Ritter, C., Starck, J.L., 1998, Ground-based observation with high spatial and spectral resolution, cesh.conf, 317K

[Labeyrie 1970] Labeyrie, A., 1970, Attainment of diffraction limited resolution in large telescopes by Fourier analysing speckle patterns in star images, A&A 6, 85-87

[Lighthill 1951] Lighthill, M.J., 1951, On sound generated aerodiynamically I. General theory, Proceedings of the Royal Society, A, 211, P. 564

[von der Lühe 1994] von der Lühe, O., 1994, Speckle imaging of solar small scale structure, A&A, 281, 889-910

[von der Lühe 1993] von der Lühe, O., 1993, Speckle imaging of solar small scale structure, A&A, 268, 374-390

[von der Lühe 1984] von der Lühe, O., 1984, Estimating Fried's parameter from a time series of an arbitrary resolved object imaged thought atmospheric turbulence, J.Opt.Soc.Am. A1,510

[Mein 1971] Mein, P., 1971, Inhomogenieties in the solar atmosphere from the CaII infra-red lines, SoPh 20,3

[Moretti et al. 2001] Moretti, P.F., et. al., 2001, The source of the solar oscillations: Convective or magnetic?, A& A 372, 1038-1047

[Neckel 1999] Neckel, H.,1999,Announcement SPECTRAL ATLAS OF SOLAR ABSOLUTE DISK-AVERAGED AND DISK-CENTER INTENSITY FROM 3290 TO 12510 (Brault and Neckel, 1987) NOW AVAILABLE FROM HAMBURG OBSERVATORY ANONYMOUS FTP SITE, SoPh 184,421

[November 1986] November, L.J., 1986, Measurement of geometric distortion in a turbulent atmosphere, Applied Optic 25, 3, 392

[Pérez Rodrìguez & Kneer 2002] Perez Rodrigues, E., Kneer, F., 2002, Formation of granular intensity fluctuation on the Sun, A&A 395, 279

[Proudman 1952] Proudman, I., 1952, The generation of noise by isotropic turbulence, Proceedings of the Royal Society of London, A 214, 119

[Soltau et al. 2002] Soltau, D., Berkefeld, Th.,von der Luehe, O., Woeger, F., Schelenz, Th.,2002, Adaptive optic and muti conjugate adaptive optic with the VTT, AN 323,3 /4, 236-240

[Starck et al. 1997] Starck, J.L., Siebenmorgen, R., Gredel, R., 1997, Spectral analysis using the wavelet transform, AJ 482, 1011-1020

[Stein 1967] Stein, R.F., 1967, Generation of acoustic and gravity waves by turbulence in an isothermal stratified atmosphere, SoPh 2, 385S

[Stein & Leibacher 1974] Stein, R.F., Leibacher, J.,1974, Waves in the solar atmosphere, A&A, 12, 407

[Stellmacher & Wiehr 1979] Stellmacher, G., Wiehr, E., 1979, A common model for solar filigree and faculae, A& A, 75, 263-267

[Stix 2002] Stix, M.,2002, The Sun an introduction, Springer -Verlag Berlin Heidelberg

[Torrence & Compo 1998] Torrence, C., Compo, G.P., 1998, A practical guide to wavelet analysis, Bull. Amer. Meteor. Soc., 79, 61

[von Uexküll et al. 1985] von Uexküll, M., Kneer, F., Mattig, W., Nesis, A., Schmidt, W., 1985, Oscillations of the Suns chromosphere III. Simultaneous $H\alpha$ observations from two sites, A& A, 146, 192-194

[Ulmschneider 2003] Ulmschneider, P., 2003, Review: the physics of chromospheres and coronae. In: Lectures in solar Physic, H.M. Antia, Springer & Verlag

[Ulmschneider & Kalkofen 2003] Ulmshneider, P., Kalkofen W., 2002, Heating of the solar chromosphere. in: Dynamic Sun, B.N. Dwivedi, Ed., Cambridge University Press, 2003

[Ulmschneider 1971b] Ulmschneider, P., 1971, On the propagation of a spectrum of acoustic waves in the solar atmosphere, A& A,14, 275-282

[Ulmschneider 1971a] Ulmschneider, P., 1971, On the computation of shock heated models for the solar chromosphere and corona, A& A,12, 297-309

[Vigouroux & Delache 1993] Vigouroux, A., Delache, Ph., Fourier versus wavelet analysis of solar diameter variability, A&A 278, 607-616

[Vujićić & Djurović 1995] Vujićić, B., Djurović, S., 1995, Astrofizika sa Astronomijom, Univerzitet u Novom Sadu Prirodno-matematicki fakultet, Novi Sad

[Wang et al. 1995] Wang, Z., Urlich, R.K., Coroniti, F.V., 1995, Acoustic wave propagation in the solar atmosphere, I. rediscussion of the linearized theory including nonstationary solutions, Astrophysical journal, 444:879-915,

[Weigelt 1977] Weigelt, G.P.,1977, Modified astronomical speckle interferometry, speckle masking, Opt. Comm., 21,55

[Weigelt & Wirnitzer 1983] Weigelt, G.P., Wirnitzer, B., 1983, Image reconstruction by the speckle-masking method, Opt. Lett.,8,389

[Wunnenberg 2003] Wunnenberg,M.,2003, Untersuchung kuryperiodischer akustischer Wellen in der Sonenatmosphaere mit Hilfe der Wavelet- Transformation, Ph.D. Thesis, Göttingen University

[Wunnenberg et al. 2003] Wunnenberg, M., Kneer, F., Hirzberger, J., 2003, Evidence for short-period acoustic waves in the solar atmosphere, A& A 271

[Wunnenberg et al. 2002] Wunnenberg, M., Andjic, A., Kneer, F., 2003, Short-period waves in the solar atmosphere, Astronomishe Nachrichten, 324, 4, 356

[Yi & Molowny Horas 1992] Yi, Z., Molowny Horas, R.L., 1992, in: Proc.from LEST Mini-workshop, Software for solar image processing, eds. Z. Yi, T. Daravann, R. Molowny Horas, Oslo ITA, 69

[USW web page] `www.uni-sw.gwdg.de/research/exp_solar/etelescope.html`

Acknowledgements

First, I wish to thank prof. F. Kneer and the Max Planck Institut fuer Sonnensystemforschung for making possibility for me to complete this work.

During the work itself I had lots of stimulating discussions which brought me new knowledge and ideas for data processing. For those discussions and support I wish to thank the solar physics group at the MPS and the Göttingen University. Especially I wish to thank R. Cameron, A. Vögler, E. Wier, and M. Sailer for all comments and suggestions.

For the help with the observations I wish to thank J.K. Hirzberger, S. Stangl and whole USW solar physics group. Especially to J.K. Hirzberger and M. Wunnenberg who had enough patience to teach me how to operate post-focus instrumentation and the telescope itself.

The scientific writing in English was the last and the biggest obstacle in my work. So my gratitude goes to R. Cameron and E. Wier which helped me to master the style of scientific writing and to A. Vögler for corrective reading.

My greatest gratitude goes to my friends and family for all patience and support they provided me during this work.

Curriculum Vitae

die Personalangaben	
Name	Aleksandra Anđić
Geburtstag	04.09.1971
Geburtsort	Banja Luka, Bosnia and Herzegovina
Staatsangehörigkeit	Bosnien
die Ausbildung	
1978-1986	Grundschule, Georgi Stojkov Rakovski, Banja Luka
1986-1990	Oberschule, Nikola Tesla, Banja Luka
1996-2001	Physik studium, PMF, University Banja Luka, Banja Luka, Bosnien
2002-2005	Ph.D. - Astrophysik, Göttingen Universiät,Deutschland
Forschungs Erfahrung	
Sonnenphysik	Kurzperiodische Wellen (Boden- und Satelliten-Beobachtungen)
Experimentalphysik	Alterungstest für PMT im AMANDA-Experiment
	Herstellung eines Demonstrations-Gerät für Thompson-Experiment
	Verbesserung eines Gerätes für Hoffman-Experiment
Physik der Polymere	Reduzierung thermischer Material-Koeffizienten, theoret. Arbeit
Optische Kommunikationen	Modellieren optischer Kommunikation in Gegenwart von Phononen
Zugewinn an Erfahrung	
2001-2002	teilzeitbeschftigte Hilfskraft für Physik-Lehre, Univerzität Banja Luka
1999-2002	Web designer
1998-2001	Studentische Hilfskraft für Physik, Univerzität Banja Luka
1997-1998	Studentische Hilfskraft für Anglistik, Univerzität Banja Luka
1996-1998	Journalistin, Banja Luka, Bosnien und Herzegovina
1996-1997	Dolmetscherin für Englisch, OSCE, Bosnen und Herzegovina